

PHOTOELASTIC AND ANALYTICAL INVESTIGATION OF STRESSES  
IN DEEP BEAMS WITH OPENINGS

---

A Thesis  
Presented to  
The Faculty of Graduate Studies and Research  
THE UNIVERSITY OF MANITOBA

---

In Partial Fulfillment  
of the Requirements for the Degree  
MASTER OF SCIENCE IN CIVIL ENGINEERING

---

by  
Benedict Hon Yiu Fan

August, 1968<sup>v</sup>



## SYNOPSIS

Simply supported deep beams with circular openings were investigated, both analytically and photoelastically.

The six beams studied were divided into two series. Series A consisted of three beams, loaded in pure bending, each with depth/span ratio of  $2/3$ , and containing a circular hole with diameter/depth ratio of  $1/3$ . However, the holes were located along the central vertical axis at different depths.

The three beams of series B also had depth/span ratios of  $2/3$  but were loaded in bending and shear with a point load at mid-span. Each beam had a pair of circular holes, diameter/depth ratio  $1/3$ , centred on the vertical axes at quarter-span from either support, and along the same horizontal line. The varying parameter in this case was the distance of the line of centres of holes from the top edge.

All six beams were experimentally studied, using two-dimensional photoelasticity. The method used for separating principal stresses was the direct numerical solution of the Laplace equation for the sum of principal stresses. For an analytical solution, an original numerical method, philosophically similar to the compatibility method of structural analysis, but using finite element techniques, was developed. A relatively coarse discretization was then applied to one beam of the B series and stresses obtained, which were then compared to the experimental results. They were seen to compare favorably.

#### ACKNOWLEDGEMENT

The author wishes to express his appreciation to Dr. B. N. Thadani for his suggestion of and keen interest in the development of the Flexibility Coefficient Method in Plane Stress Analysis presented in Chapter 3, and for his invaluable help in the understanding of technical literature published in German and Russian.

## TABLE OF CONTENTS

CHAPTER	PAGE
1. INTRODUCTION . . . . .	1
2. REVIEW OF LITERATURE . . . . .	5
3. A FLEXIBILITY COEFFICIENT METHOD IN PLANE STRESS	
ANALYSIS . . . . .	8
Introduction . . . . .	8
The Primary Structure and the Calculation	
of Flexibility Coefficients . . . . .	9
Numerical Procedure . . . . .	18
4. ANALYTICAL SOLUTION TO PROBLEMS OF DEEP BEAMS	
WITH OPENINGS . . . . .	26
Discretization . . . . .	26
Selection of Redundants . . . . .	28
Computations . . . . .	28
5. THE PHOTOELASTIC EXPERIMENT . . . . .	35
Fundamental Principles . . . . .	35
Materials for Photoelastic Models . . . . .	36
Experimental Procedures . . . . .	38
Interpretation of Photoelastic Data . . . . .	52
Separation of Principal Stresses . . . . .	52
6. DISCUSSIONS . . . . .	93
Observations on Experimental and	
Analytical Results . . . . .	93

CHAPTER	PAGE
Application of Experimental Results	
to Prototypes . . . . .	94
Conclusions . . . . .	95
BIBLIOGRAPHY . . . . .	97
APPENDIX A EVALUATION OF MOHR'S INTEGRALS . . . . .	99
Rectangular Elements -- Direct Stress Terms	99
Rectangular Elements -- Crossed	
Stress Terms . . . . .	101
Elements at Curvilinear Boundaries . . . . .	103
APPENDIX B ADAPTATION OF THE FLEXIBILITY COEFFICIENT METHOD	
TO COMPUTERS . . . . .	106
APPENDIX C CASTING OF ARALDITE SHEETS FOR TWO-DIMENSIONAL	
PHOTOELASTICITY . . . . .	113

LIST OF TABLES

TABLE		PAGE
3.1	Stresses at Interfaces of the Beam in Example Problem . . . . .	23
4.1	Redundant Stress Resultants in Beam B-2 . . . . .	31
4.2	Stresses in Beam B-2 . . . . .	32
5.1	Photographic Data . . . . .	51
5.2	Solution 1 for $(\sigma_1 + \sigma_2)$ of Beam A-1 . . . . .	57
5.3	Solution 1 for $(\sigma_1 + \sigma_2)$ of Beam A-2 . . . . .	58
5.4	Solution 1 for $(\sigma_1 + \sigma_2)$ of Beam A-3 . . . . .	59
5.5	Solution 1 for $(\sigma_1 + \sigma_2)$ of Beam B-1 . . . . .	60
5.6	Solution 1 for $(\sigma_1 + \sigma_2)$ of Beam B-2 . . . . .	61
5.7	Solution 1 for $(\sigma_1 + \sigma_2)$ of Beam B-3 . . . . .	62
5.8	Solution 2 for $(\sigma_1 + \sigma_2)$ of Beam A-1 . . . . .	63
5.9	Solution 2 for $(\sigma_1 + \sigma_2)$ of Beam A-2 . . . . .	64
5.10	Solution 2 for $(\sigma_1 + \sigma_2)$ of Beam A-3 . . . . .	65
5.11	Solution 2 for $(\sigma_1 + \sigma_2)$ of Beam B-1 . . . . .	66
5.12	Solution 2 for $(\sigma_1 + \sigma_2)$ of Beam B-2 . . . . .	67
5.13	Solution 2 for $(\sigma_1 + \sigma_2)$ of Beam B-3 . . . . .	68

LIST OF FIGURES

FIGURE		PAGE
3.1	Discretized Structure as Assemblage of Finite Elements Connected with Fictitious Hinges at Centres of Interfaces . . . . .	10
3.2	Discretized Doubly-Connected Continuum . . . . .	10
3.3a	Stresses on Typical Rectangular Element . . . . .	11
3.3b	Typical Stress Variations . . . . .	11
3.4a	$\sigma^0$ and $\tau^0$ on Primary Structure . . . . .	13
3.4b	$\sigma^i$ and $\tau^i$ for $b\tau_{m+1}^i = 1$ . . . . .	13
3.5	Stress Variations for Element 1 . . . . .	16
3.6	$\sigma^k$ and $\tau^k$ for $a\tau_n^k = 1$ . . . . .	16
3.7	Wall Beam with U.D.L. at Upper Edge. . . . .	19
3.8a	Applied Loads on Primary Structure . . . . .	22
3.8b	Self-Equilibrating System for $S_3 = 1$ . . . . .	22
3.9	$\sigma_x$ at Centre-Line of Wall Beam . . . . .	25
4.1	Discretization of Beam B-2 . . . . .	27
4.2	Self-Equilibrating System for $S_{32} = 1$ . . . . .	29
5.1	Loading Diagrams . . . . .	39
5.2a	Isochromatics in Circular Disk Under Diametral Compression . . . . .	40
5.2b	Variation of Fringe Order Along x-Axis of Circular Disk . . . . .	40
5.3	Isochromatics in Beam A-1 with $P = 400$ lb . . . . .	44

FIGURE		PAGE
5.4	Isochromatics in Beam A-2 with P = 480 lb . . . . .	45
5.5	Isochromatics in Beam A-3 with P = 480 lb . . . . .	46
5.6	Isochromatics in Beam B-1 with P = 216 lb . . . . .	47
5.7	Isochromatics in Beam B-2 with P = 240 lb . . . . .	48
5.8	Isochromatics in Beam B-3 with P = 240 lb . . . . .	49
5.9	Isoclinics in Beam B-2 . . . . .	50
5.10	Variation of $\sigma_{\theta}/\sigma_m$ Around Hole of Beam A-1 . . . . .	53
5.11	Variation of $\sigma_{\theta}/\sigma_m$ Around Hole of Beam A-2 . . . . .	53
5.12	Variation of $\sigma_{\theta}/\sigma_m$ Around Hole of Beam A-3 . . . . .	54
5.13	Variation of $\sigma_{\theta}/\sigma_m$ Around Left Hole of Beam B-1 . . . . .	54
5.14	Variation of $\sigma_{\theta}/\sigma_m$ Around Left Hole of Beam B-2 . . . . .	55
5.15	Variation of $\sigma_{\theta}/\sigma_m$ Around Left Hole of Beam B-3 . . . . .	55
5.16	Principal Stresses in Beam A-1 . . . . .	71
5.17	Principal Stresses in Beam A-2 . . . . .	72
5.18	Principal Stresses in Beam A-3 . . . . .	73
5.19	Principal Stresses in Beam B-1 . . . . .	74
5.20	Principal Stresses in Beam B-2 . . . . .	75
5.21	Principal Stresses in Beam B-3 . . . . .	76
5.22	Beam A-1, $\frac{\partial \sigma_s}{\partial x}$ and $\frac{\partial \sigma_s}{\partial y}$ . . . . .	77
5.23	Beam A-2, $\frac{\partial \sigma_s}{\partial x}$ and $\frac{\partial \sigma_s}{\partial y}$ . . . . .	78
5.24	Beam A-3, $\frac{\partial \sigma_s}{\partial x}$ and $\frac{\partial \sigma_s}{\partial y}$ . . . . .	79
5.25	Beam B-1, $\frac{\partial \sigma_s}{\partial x}$ and $\frac{\partial \sigma_s}{\partial y}$ . . . . .	80
5.26	Beam B-2, $\frac{\partial \sigma_s}{\partial x}$ and $\frac{\partial \sigma_s}{\partial y}$ . . . . .	81
5.27	Beam B-3, $\frac{\partial \sigma_s}{\partial x}$ and $\frac{\partial \sigma_s}{\partial y}$ . . . . .	82

FIGURE		PAGE
A.1a	Stress Variation for $\sigma_x^i$ . . . . .	100
A.1b	Stress Variation for $\sigma_x^k$ . . . . .	100
A.2a	Stress Variation for $\sigma_x^i$ . . . . .	102
A.2b	Stress Variation for $\sigma_y^k$ . . . . .	102
A.3	Stress Variations on a Truncated-Rectangular Element . . . . .	104
B.1	Notation of Stresses in the Program . . . . .	108
B.2	Flow Chart for Flexibility Coefficients Program . . . . .	109
B.3	Program for Flexibility Coefficients & Stress Resultants . . . . .	110

LIST OF PLATES

PLATE		PAGE
1	Matching Dark-Light Field Isochromatics in Circular Disk . . . . .	83
2	Dark and Light Field Isochromatics in Beam A-1 . .	84
3	Dark and Light Field Isochromatics in Beam A-2 . .	85
4	Dark and Light Field Isochromatics in Beam A-3 . .	86
5	Model in Dark and Light Fields before Load Application . . . . .	87
6	Dark and Light Field Isochromatics in Beam B-1 . .	88
7	Dark and Light Field Isochromatics in Beam B-2 . .	89
8	Dark and Light Field Isochromatics in Beam B-3 . .	90
9	Isoclinics in Beam B-2 . . . . .	91
10	Isoclinics in Beam B-2 (Continued) . . . . .	92

## LIST OF SYMBOLS

- $a$  = length of rectangular element  
 $b$  = width of rectangular element  
 $L$  = span of beam  
 $H$  = depth of beam  
 $d$  = flexibility coefficient  
 $D$  = displacement  
 $m, n$  = interface numbers  
 $N$  = normal stress resultant  
 $S$  = shearing stress resultant  
 $q$  = intensity of distributed load  
 $X$  = redundant  
 $\sigma$  = normal stress  
 $\tau$  = shearing stress  
 $\epsilon$  = linear strain  
 $\gamma$  = shearing strain  
 $\sigma_1$  = major principal stress  
 $\sigma_2$  = minor principal stress  
 $f_\sigma$  = material fringe value  
 $f'_\sigma$  = Model fringe value  
 $\sigma_s$  = extreme fibre stress as calculated with  
simple beam theory  
 $E$  = modulus of elasticity  
 $G$  = shear modulus

## 1. INTRODUCTION

A deep beam may be defined as one whose depth is comparable to its span. Beams of this type, both in steel and in reinforced concrete, often arise in the construction of bins, hoppers or similar structures, as well as in more ordinary construction of foundation walls or in cases in which walls are supported on individual columns or footings. The vertical or horizontal diaphragms used to transmit wind forces in tall buildings (walls or floors) are frequently of such dimensions as to be classified as deep beams.

The problem of holes in beams, especially beams with large depth/span ratios, is not uncommon. In almost all buildings and related structures, openings of some sort are required either for access or for passing piping, ventilation or electrical systems to different compartments. Such material discontinuities cause stress concentrations in structural members and, if neglected, may endanger the otherwise well designed structure. It is, therefore, the duty of the structural engineer to carefully evaluate these stress concentrations and properly allow for them in the overall design.

As is well known, the ordinary theory of bending, the Bernoulli-Euler theory, cannot be applied to a beam whose depth is greater than about half its span. The stress distribution in deep beams has received the attention of mathematicians and research workers since the turn of the century. One common approach is by solving the bi-harmonic equation for the Airy stress function, and then obtaining the normal and shear stresses as second partial derivatives of the stress function. Unfortunately, in the case of the deep beam, there are six boundary conditions to be satisfied in the general loading case and only four constants in the bi-harmonic

(15)

so that no general solution is possible. Approximate solutions, however, have been obtained for certain simple loading cases by choosing a particular solution for the bi-harmonic and then finding a polynomial which, when super-imposed on the particular solution, will satisfy boundary conditions.

Neglecting body forces, and assuming all boundary forces to be given, the stress distribution in two-dimensional problems involving simply-connected bodies is independent of the material. However, the presence of openings greatly complicates the mathematical solution, since in multiply-connected bodies, the possibility exists that strains may be multi-valued even when the stresses are single-valued <sup>(10)</sup>. In such problems, not only must the mathematical solution satisfy the conditions at the boundaries, but in addition the expressions for displacement must be examined to see that they are single-valued. The mathematical solution of deep beams with openings thus becomes a very tedious and involved, and very often impossible, task.

Classical mathematics, despite its ever-increasing sophistication, is basically capable of solving only highly idealized situations while demanding at the same time a great deal of skilled time, which could otherwise be more usefully employed in the process of design. Fortunately, with the advent of digital computers which perform arithmetical operations at an amazing speed, methods of numerical analysis have been developed which are easily adaptable to electronic computations. The finite difference and the up-coming finite element methods are fine examples of such techniques. Unlike solutions employing classical mathematics, numerical solutions encounter no difficulty in satisfying boundary conditions. Numerical methods give approximate solutions, but so do

mathematical analyses which make use of series convergence. In the latter case, only a series summed to infinite number of terms will yield an exact solution. In the finite difference method, the approximation lies in the solution of the bi-harmonic, whereas in the finite element method, the approximation is in the assumption of behaviour of individual elements.

Before numerical solutions of real problems dealing with complex continua can be performed, it is necessary to limit the number of unknowns involved --- a process known as discretization. Naturally, the finer the discretization, the closer will be the solution obtained to its exact value. The digital computer, with its tremendous capacity and speed, is ideally suited to solve the large number of linear algebraic equations resulting from the numerical analysis.

Alternatively, the complicated problems of stress distribution in multiply-connected continua may be solved experimentally with the relatively simple and yet very powerful photoelastic methods. Photoelastic methods excel in yielding a whole-field representation of stress distribution and concentration.

The science of photoelasticity first appeared in the engineering world at the turn of the century, and has since become a powerful tool for stress analysts. It is applicable to any state of stress, but it can be most conveniently applied in studies of two-dimensional state of stress. The present problem may be studied as a plane-stress case if it is assumed that either the thickness of the beam is small compared with its other dimensions, or the load is applied uniformly throughout its thickness. Thus only two-dimensional photoelastic equipment and technique are required.

Photoelastic data include principal stress directions and differences in principal stresses. Any standard method of separation of principal stresses --- be it the interferometer, the lateral extensometer, the oblique incidence or the shear difference method, or the semi-analytical method of numerical solution of the Laplace equation for sums of principal stresses --- completes the analysis for stresses in a given continuum.

## 2. REVIEW OF LITERATURE

The departure of stresses in deep beams from straight-line distribution is well known. In 1932 Dischinger<sup>(6)</sup> used trigonometric series to determine the stresses in continuous deep beams. The Portland Cement Association prepared an expanded version of Dischinger's paper and added solution for simply supported spans. Conway, Chow and Morgan<sup>(3)</sup>, in 1951, proposed a method of solving problems of simply supported deep beams by satisfying lateral boundary conditions by super-imposing on the primary Airy stress function, a second stress function obtained with a strain energy method. Later in 1952, Chow, Conway and Winter<sup>(1)</sup> used finite difference equations to deal with the same problems. Many cases of loading and depth/span ratios were studied for the simply supported deep beam, but, unfortunately, it was later brought out in a discussion of the paper that a considerable amount of error existed because of the coarseness of the net and inherent rounding-off of peak values.

An exhaustive compilation of solution to problems of plates, with or without openings, loaded transversely or in their planes, with various support conditions, was prepared by Weinberg<sup>(22)</sup>. Timoshenko<sup>(20)</sup> also gave solutions to beams with circular openings, but only limited to openings that are small compared with dimensions of the beam, and a further simplification of uniform stress field was made. Muskhelishvili<sup>(13)</sup>, in his book on problems in elasticity, indicated the use of conformal mapping in solving problems dealing with multiply-connected bodies. Boundary conditions, however, were again idealized. Timoshenko<sup>(20)</sup> demonstrated the application of finite difference techniques to problems of multiply-connected bodies, with special considerations to how conditions at secondary boundaries could be satisfied. The work of Savin on stress

concentration around holes has been translated into English and published  
(17)  
in the form of a monograph . It is an extensive theoretical investi-  
gation of the influence of various holes in the state of stress in a  
non-uniform stress field in a plane, based on one important assumption ---  
that this influence is localized.

The difficulty of satisfying boundary conditions no longer exists  
with the recent development of finite element techniques, which consider  
the discretized continuum as an assemblage of elements whose behaviour is  
studied with the basic methods of structural analysis, namely the force  
and displacement methods. The large number of resulting linear algebraic  
equations are expediently solved with high speed electronic computers.  
(24) and(25)  
Clough and Zienkiewicz (11) have made important contributions to  
this field, while Gaonkar (11) explores the feasibility of various numerical  
methods in solving problems of inclusions.

Literature on photoelastic analysis of deep beams or beams with open-  
(14)  
ings are relatively scarce. Saad and Hendry (14) investigated simply  
supported deep beams, depth/span ratios of 2/3, 1 and 1.59, each carrying  
a central concentrated load. The conclusion was that the simple beam  
theory was adequate in the case of beams whose spans exceeded 1.5 times  
(12)  
their depths. Gibson and Jenkins (12) photoelastically analysed a simply  
supported shallow beam with a circular opening at the centre of the beam  
and carrying a concentrated load at mid-span. Holes of different sizes  
were studied and it was found that the pattern of local stress concentration  
around the holes could not be predicted by mathematical theory.

No literature on deep beams with openings have been located, even  
with the help of the exhaustive Geodex Structural Information Index.

It is therefore hoped that this contribution to the study of the problem will provide useful information to designers and serve to encourage further investigation of the problem.

### 3. A FLEXIBILITY COEFFICIENT METHOD IN PLANE STRESS ANALYSIS

#### 3.1 Introduction

Any method of analysis of indeterminate structures must satisfy the following conditions:

- (1) Equilibrium of the structure is maintained.
- (2) Stress-strain relationship of the elastic material is obeyed.
- (3) Compatibility exists between different parts of the structure before fracture.

Consequently, all methods are basically similar except for the order in which the above conditions are satisfied. In particular, the flexibility coefficient method, also known as the force or compatibility method, initially assumes equilibrium of the structure. Further equations are then obtained by stipulating compatibility requirement between parts of the structure. The stress-strain relationship is implicitly obeyed in the process of determining flexibility coefficients.

The same concepts may be used in problems of stress analysis, and most conveniently in plane stress problems. When the body is discretized into a finite number of elements, it can be considered as an ordinary indeterminate structure. In this particular method, the unknowns are the normal and shear stress resultants, which are assumed to be acting at the centres of the interfaces between elements. Thus the discretized structure is statically equivalent to an assemblage of elements connected by fictitious hinges at the centres of interfaces (Fig. 3.1).

Basically, the relation between the method presented here and the usual finite element method can be compared to the relation between the force and displacement methods used in analysis of indeterminate structures.

As will be seen later, the procedure used in solution of any plane stress problem by flexibility coefficients closely parallels the steps used in setting up and solving the elastic equations of the force method.

As compared to the usual finite element technique, the flexibility coefficient method offers several advantages. Geometrical and stress conditions at the boundaries are automatically satisfied, and in most cases the number of unknowns is substantially less than in the finite element approach. One of the outstanding features of the method is its remarkable simplicity and the ease with which it can be adapted for the computer by making use of a few simple standard sub-routines.

### 3.2 The Primary Structure and the Calculation of Flexibility Coefficients

In the flexibility coefficient approach, any elastic body in a state of plane stress can be considered as an assemblage of mostly rectangular elements with trapezoidal or truncated-rectangular elements at curvilinear boundaries (Fig. 3.2). In the subsequent development, it is simpler to concentrate one's attention on a typical rectangular element as is shown in Fig. 3.3a.

Assuming the body to be of unit thickness, the well-known equilibrium equations for such an element can be written in a finite difference form (21) and (7) as

$$(\sigma_{x,m+1} - \sigma_{x,m})b + (\tau_{yx,n+1} - \tau_{yx,n})a + abX = 0 \quad (3.1)$$

$$(\sigma_{y,n+1} - \sigma_{y,n})a + (\tau_{xy,m+1} - \tau_{xy,m})b + abY = 0 \quad (3.2)$$

where X and Y are body stresses. As can be seen from Fig. 3.3b, these equations assume that the variations of the stresses  $\sigma_x$ ,  $\tau_{xy}$ ,  $\sigma_y$ ,  $\tau_{yx}$  across the lengths of the element are linear. And by considering the

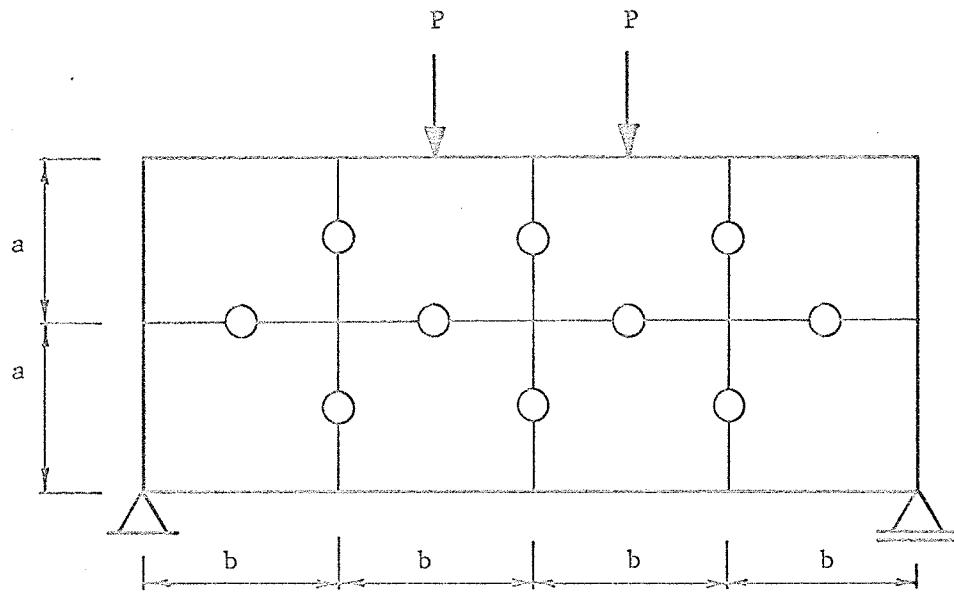


Fig. 3.1 - Discretized Structure as Assemblage of Finite Elements Connected with Fictitious Hinges at Centres of Interfaces

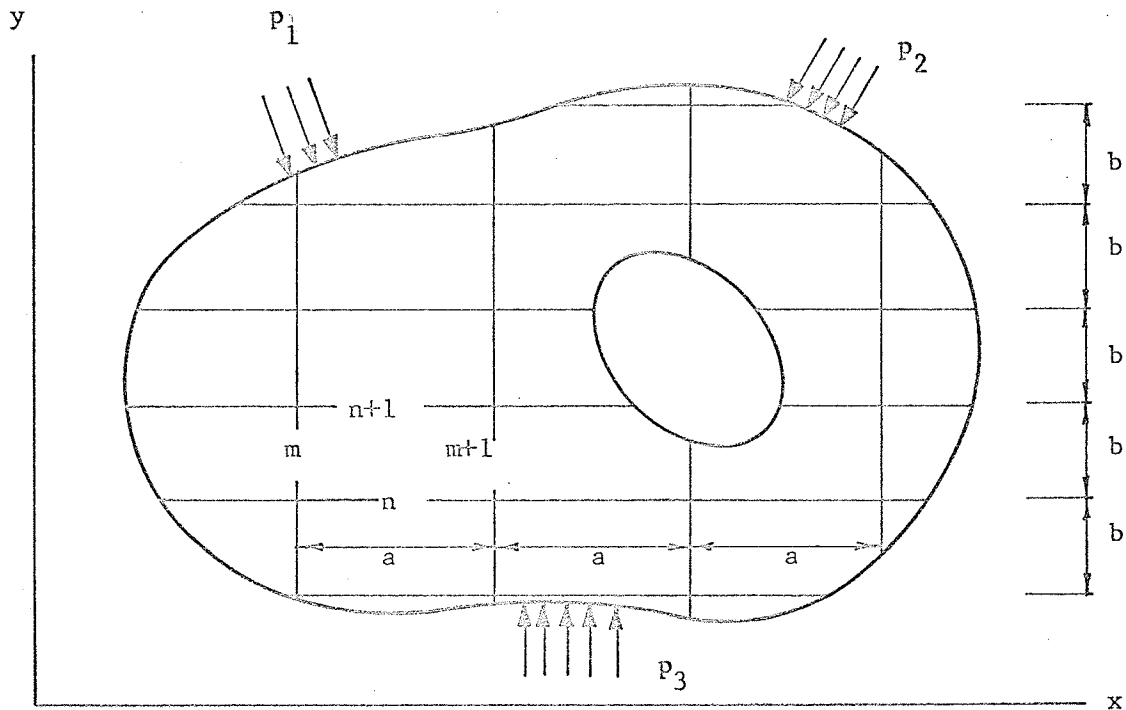


Fig. 3.2 - Discretized Doubly-Connected Continuum

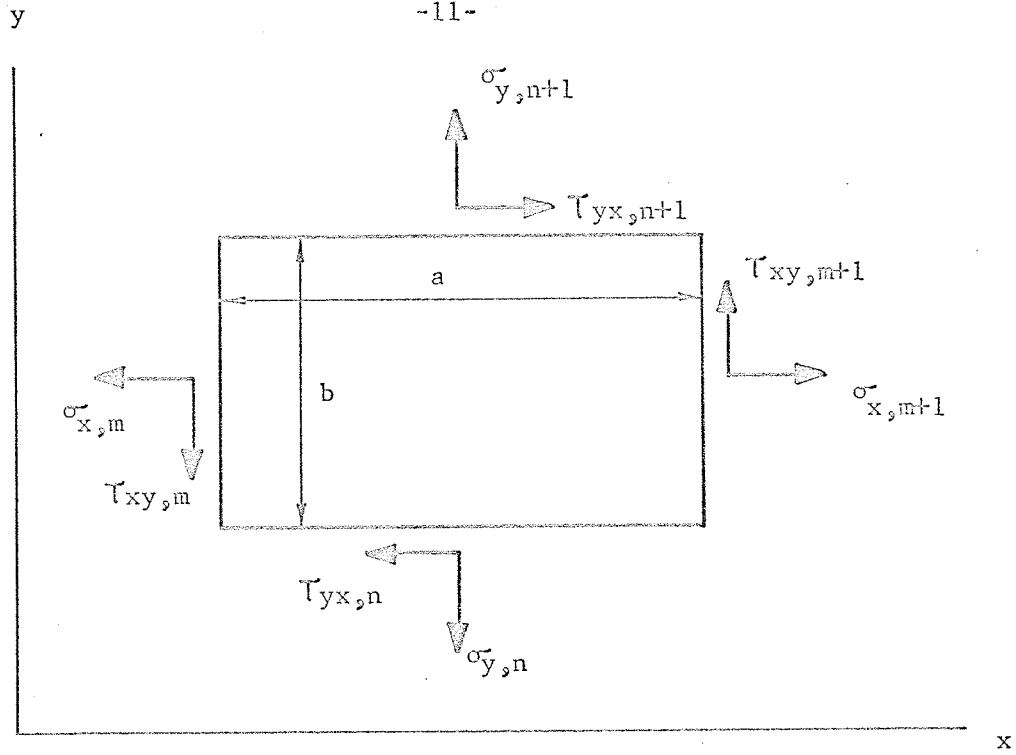


Fig. 3.3a - Stresses on Typical Rectangular Element

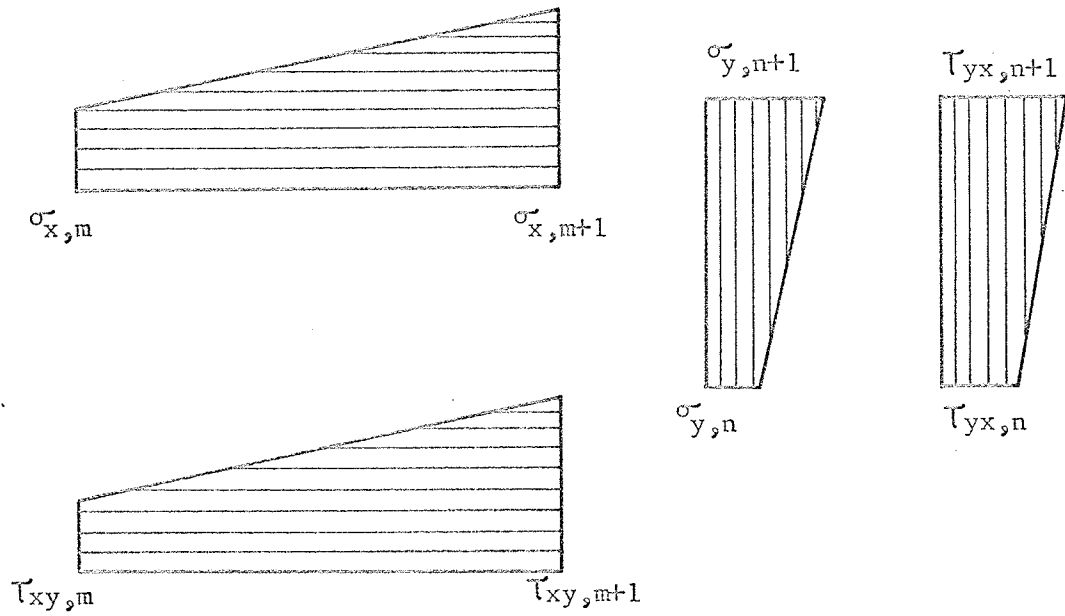


Fig. 3.3b - Typical Stress Variations

stress resultants to act at the centres of interfaces, one has inherently assumed uniform stress distribution over the interfaces between the finite elements. Further, it may be noted that since elements of finite lengths are being considered,  $\tau_{xy} \neq \tau_{yx}$ , since equality applies only to infinitesimally small elements.

Two such equilibrium equations can be written out for each element, so that if the body of Fig. 3.2 were divided into E elements, a total of 2E equilibrium equations would be available. At each interface such as m in Fig. 3.2, normal and shearing stresses  $\sigma$  and  $\tau$  are acting. If F is the number of interfaces, then the number of stresses to be determined is 2F. The assemblage of E elements constituting the body is therefore indeterminate I times where

$$I = 2(F - E) \quad (3.3)$$

Of the 2F stresses to be found, I stresses can be treated as redundants and on setting these as zero, a primary structure will be obtained which should be determinate and geometrically stable. Bearing this in mind, it is not difficult to decide on which of the 2F stresses can be treated as redundants.

Consider now the primary structure. Under the action of the applied loads, primary stresses which can be denoted by  $\sigma^0$ ,  $\tau^0$  are produced at the interfaces as shown in Fig. 3.4a. These can be evaluated by writing out equation (3.1) and (3.2) for each element and by considering the equilibrium of groups of such elements taken as rigid bodies.

Due to the deformations of the individual elements, discontinuities will be produced in the direction of the redundants at the interfaces. These deformations which can be denoted in general by  $D^0$ , are evaluated by

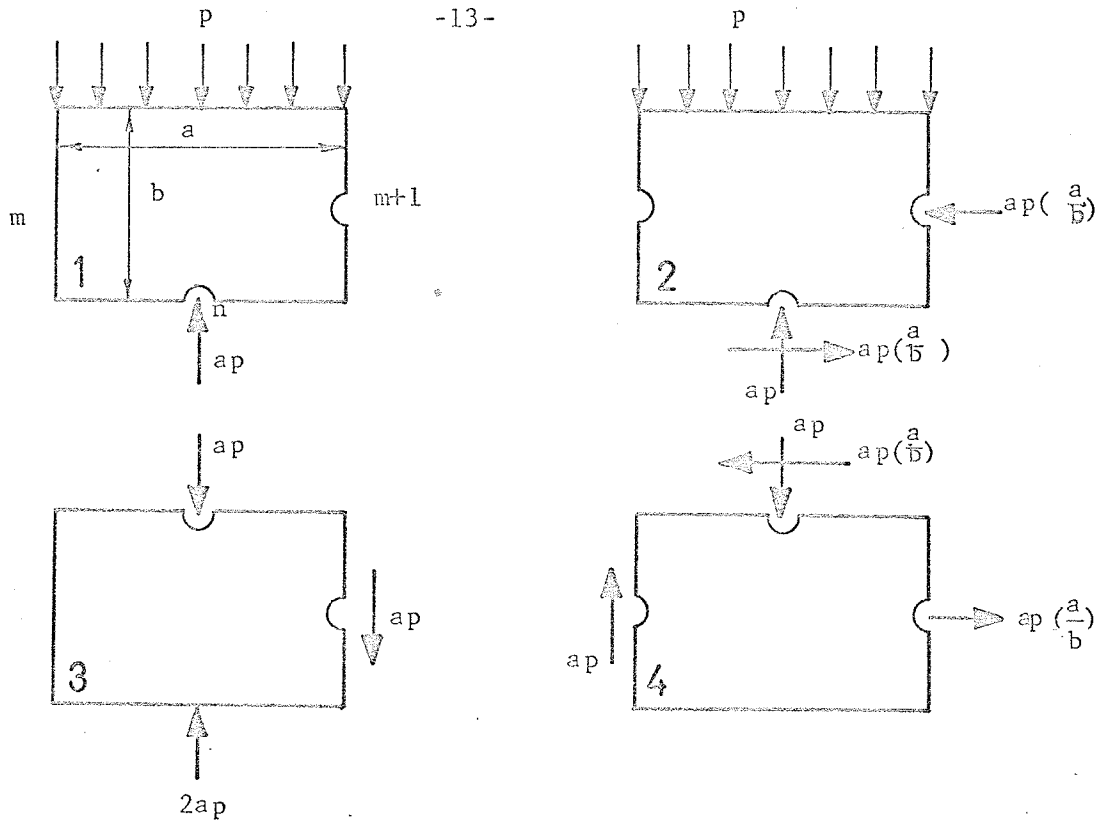


Fig. 3.4a -  $\sigma^0$  and  $\tau^0$  on Primary Structure

Fictitious Hinge shown thus  $\text{-----} \bigcirc$

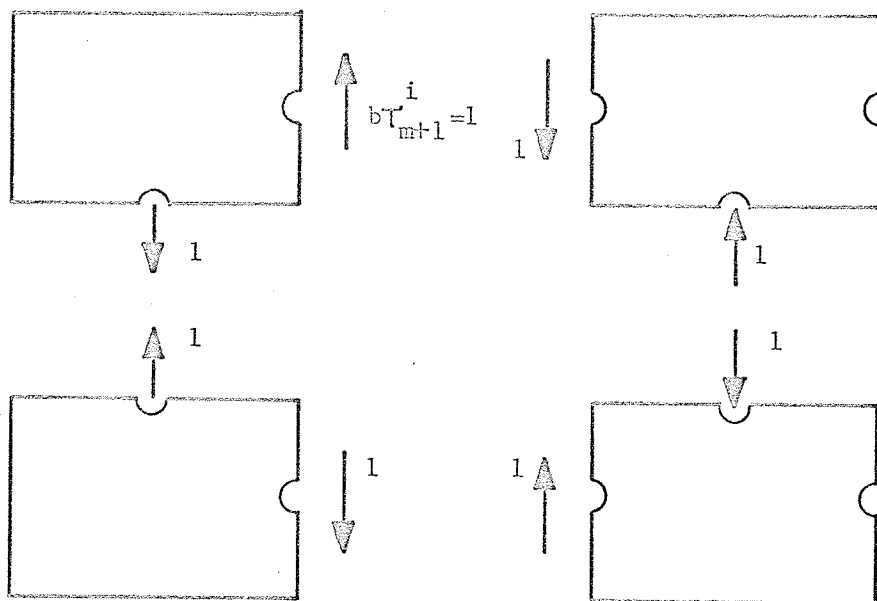


Fig. 3.4b -  $\sigma^i$  and  $\tau^i$  for  $b\tau_{m+1}^i = 1$

applying suitable fictitious loads to the primary system.

Fig. 3.4b shows the effect of a unit fictitious load  $b\bar{T}^i=1$  applied at the interface of the elements marked 1, 3, where  $\bar{T}^i$  is a fictitious stress acting in the direction of the redundant  $X^i$ . The effect of this fictitious stress will generally be localized over a limited number of elements, since the stresses are self-equilibrating. The stress distribution throughout these elements will also be mostly rectangular or triangular, a fact which further simplifies calculations.

The discontinuity  $D_i^0$  in the primary structure along the direction of  $\bar{T}^i$  is found by applying Mohr's equation of virtual work to the two loading cases shown in Fig. 3.4a and 3.4b. The result is

$$(b\bar{T}^i)D_i^0 = \int \sigma_x^i \epsilon_x^0 dV + \int \bar{T}^i \gamma^0 dV + \int \sigma_y^i \epsilon_y^0 dV \quad (3.4)$$

where  $\epsilon_x^0, \gamma^0$  are the strains in the primary structure. Considering only the case of plane stress and putting

$$\begin{aligned} \epsilon_x^0 &= \frac{1}{E} (\sigma_x^0 - \mu\sigma_y^0); & \epsilon_y^0 &= \frac{1}{E} (\sigma_y^0 - \mu\sigma_x^0); \\ \gamma^0 &= \frac{1}{G} (\tau^0) = \frac{2}{E} (1+\mu)\tau^0 = \frac{1}{E} (1+\mu) (\tau_{xy}^0 + \tau_{yx}^0) \end{aligned} \quad (3.5)$$

gives the equation

$$\begin{aligned} D_i^0 &= \frac{1}{E} \iint (\sigma_x^i \sigma_x^0 + \sigma_y^i \sigma_y^0) dx dy - \frac{\mu}{E} \iint (\sigma_x^i \sigma_y^0 + \sigma_y^i \sigma_x^0) dx dy \\ &+ \frac{1}{E} (1+\mu) \iint \tau_{xy}^i \tau_{xy}^0 dx dy + \frac{1}{E} (1+\mu) \iint \tau_{yx}^i \tau_{yx}^0 dx dy \end{aligned} \quad (3.6)$$

Since the principle of complementary shearing stresses does not apply, it is necessary to consider the virtual work done by the shearing stresses  $\tau_{xy}$  and  $\tau_{yx}$  separately in equation (3.6). The integrations in this equation have to be performed over the entire region of the body. Since the variation of stresses over each element is linear, the integrals can be readily evaluated by using the standard tables for Mohr's (18) integrals. For instance, referring to Fig. 3.5 and considering the element marked 1,

$$\iint \sigma_x^i \sigma_x^o \, dx \, dy = \frac{ab}{6} \left[ \sigma_{x,m}^i (2\sigma_{x,m}^o + \sigma_{x,m+1}^o) + \sigma_{x,m+1}^i (2\sigma_{x,m+1}^o + \sigma_{x,m}^o) \right] \quad (3.7)$$

Equation (3.6) can now be written in a form suitable for computation by replacing the integrals by sums of the type indicated in equation (3.7) and extending the summation over the entire assemblage of elements. Derivations of equation (3.7) and similar expressions for other integrals indicated in equation (3.6) are given in Appendix A, while Appendix B discusses the computerization of these operations.

The flexibility coefficients are defined as the displacements produced in the primary structure under no loads, when one of the redundant forces is set equal to unity while the other redundants are assumed zero. Fig. 3.6 shows the redundant force  $a\tau_{xy}^k=1$  acting at the interface of elements 2, 4. Applying Mohr's equation to the two loading cases of Figs. 3.4b and 3.6 gives

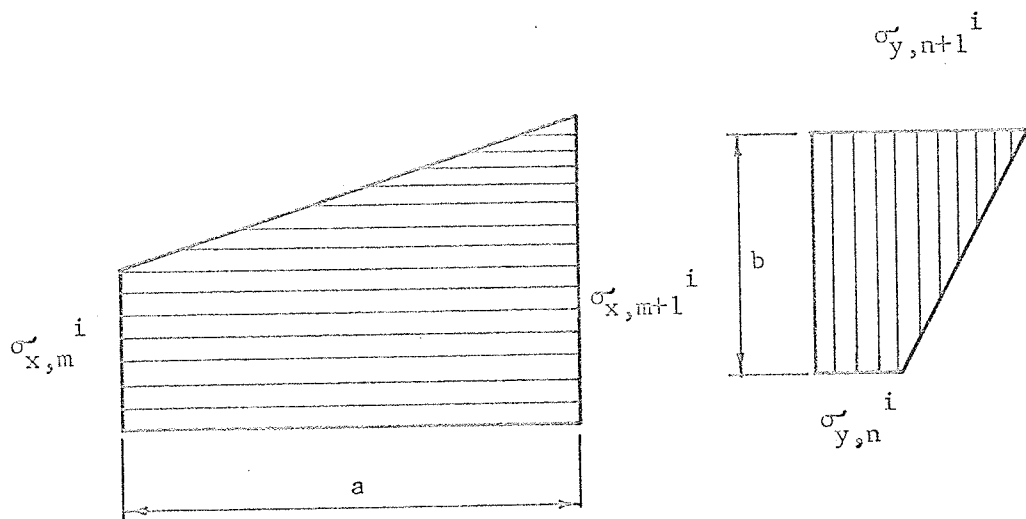


Fig. 3.5 - Stress Variations for Element 1

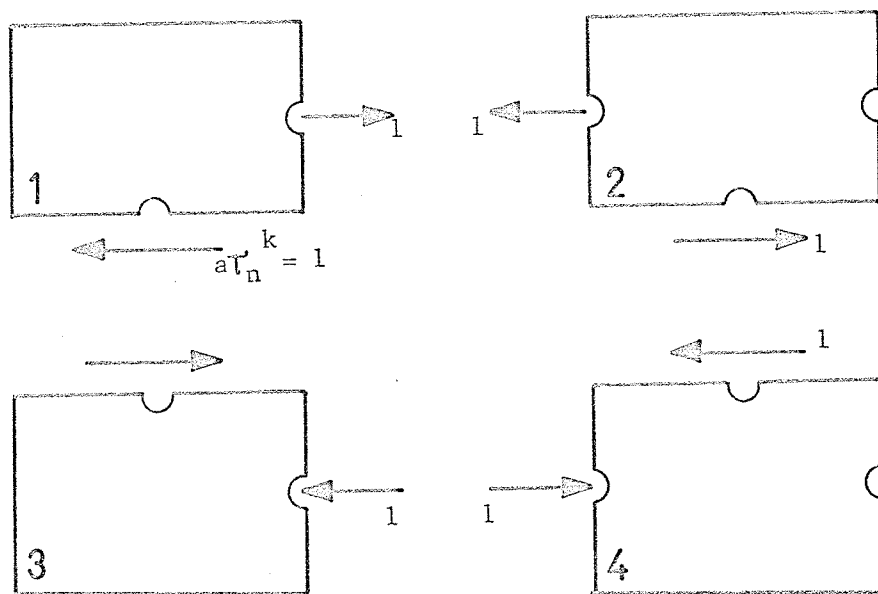


Fig. 3.6 -  $\sigma^k$  and  $\tau^k$  for  $a\tau_n^k = 1$

$$d_{ik} = \frac{1}{E} \iint (\sigma_x^i \sigma_x^k + \sigma_y^i \sigma_y^k) dx dy - \frac{\mu}{E} \iint (\sigma_x^i \sigma_y^k + \sigma_y^i \sigma_x^k) dx dy$$

$$+ \frac{1}{E(1+\mu)} \iint \tau_{xy}^i \tau_{xy}^k dx dy + \frac{1}{E(1+\mu)} \iint \tau_{yx}^i \tau_{yx}^k dx dy \quad (3.8)$$

The integrals are again evaluated for each element and summed up to give the value of the integral taken over the entire region.

For compatibility of the displacements of the various elements to occur, no discontinuities should exist in the displacements of points situated on interfaces of two adjacent elements. This leads to the usual compatibility equations

$$\begin{bmatrix} d_{11} & d_{12} & \dots & d_{1n} \\ d_{21} & d_{22} & \dots & d_{2n} \\ \dots & \dots & \dots & \dots \\ d_{n1} & d_{n2} & \dots & d_{nn} \end{bmatrix} \begin{bmatrix} X_1 \\ X_2 \\ \dots \\ X_n \end{bmatrix} + \begin{bmatrix} D_1^0 \\ D_2^0 \\ \dots \\ D_n^0 \end{bmatrix} = [0] \quad (3.9)$$

where any redundant such as  $X^i$  is the product of a stress and the length of the element, that is

$$X^i = a \sigma^i \quad \text{or} \quad X^i = a \sigma^j$$

In matrix notation, the above compatibility equations can be written in the usual form as

$$[d] [X] + [D^0] = [0] \quad (3.9a)$$

Solution of these equations gives the values of the redundants, which are then used to evaluate the remaining unknown stress resultants by using the equilibrium equations (3.1) and (3.2) and the principle of super-position.

In dealing with curvilinear boundaries, the elements at such boundaries are likely to be non-rectangular, although they are still bounded by straight lines. The basic equilibrium equations would hold good even for such elements. However, the integrals involved in the virtual work equations (3.6) and (3.8) would have to be modified from their normal numerical form as in equation (3.7). These necessary modifications are discussed in Appendix A. It may be mentioned that the number of non-rectangular elements is generally small compared to the large number of rectangular elements that are present. Any approximation inherent in the evaluation of the virtual work integrals over such elements is therefore not likely to materially affect the final solution.

### 3.3 Numerical Procedure

The numerical procedure involved in this method is best illustrated by considering the analysis of the wall-beam of Fig. 3.7 subjected to distributed loads applied to the upper edge. Tabulated values of the stress distribution in a similar problem are available <sup>(3)</sup> so that the solution can be fruitfully compared to accepted values.

Since the beam is symmetrically loaded, only half of it need be considered in its analysis, shearing stresses along the centre-line being zero. In order not to obscure the essence of the method with an unduly large amount of computations, a very coarse discretization is here used. The elements and interfaces are numbered as shown in Fig. 3.7.

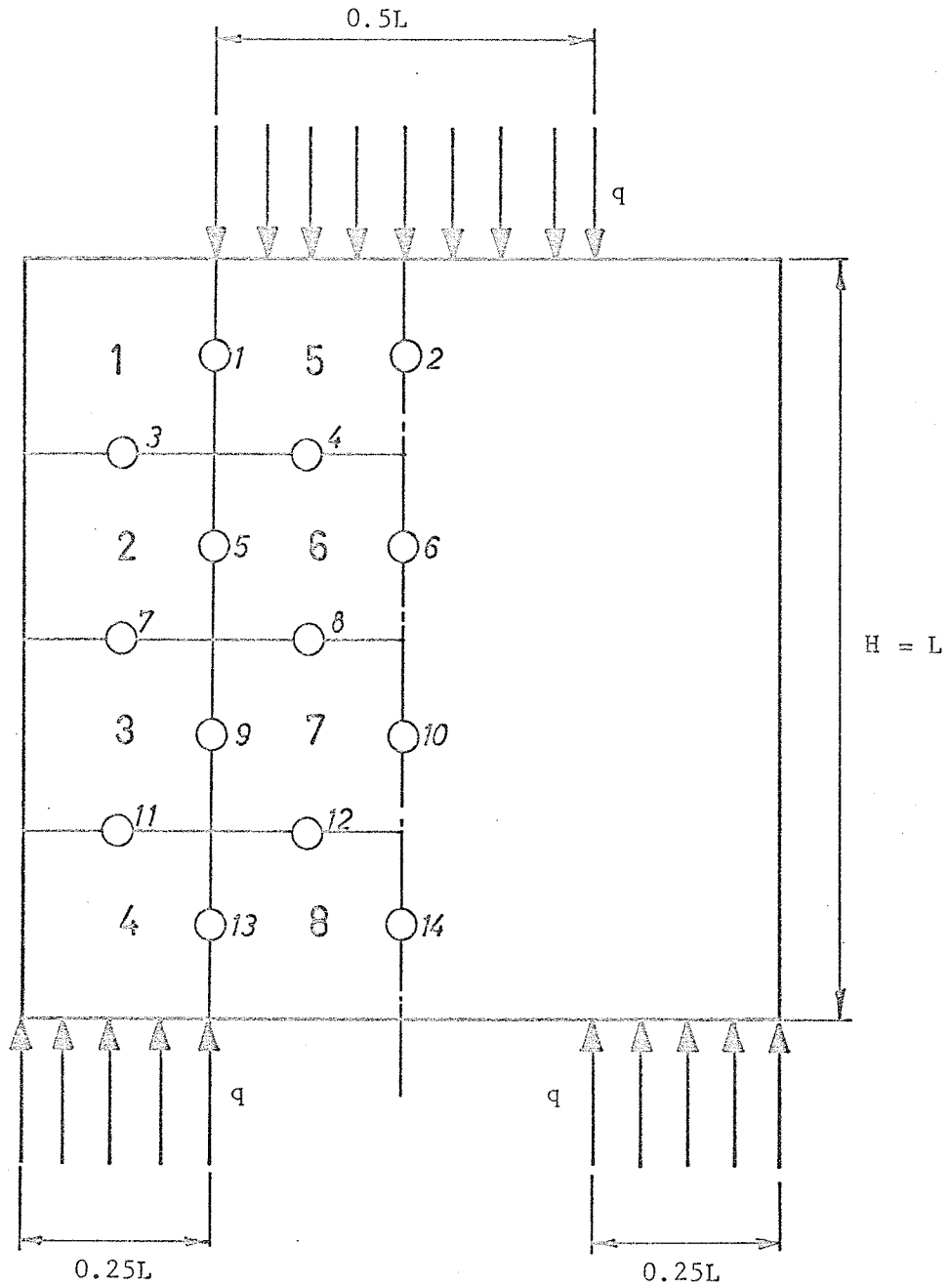


Fig. 3.7 - Wall Beam with U.D.L. at Upper Edge

Since the redundants are the stress resultants,  $N_i$  and  $S_i$  will be used to denote the normal and shearing stress resultants, respectively, where  $i$  represents the number of the interface on which the resultant acts.

There are 14 interfaces and, therefore, 28 unknowns of which, however,  $\tau_2, \tau_6, \tau_{10}$  and  $\tau_{14}$  are zero. Eight elements give a total of 16 equilibrium equations of the types occurring in equation (3.1) and (3.2). Hence eight unknowns have to be removed as redundants before the structure becomes statically determinate. The most convenient way of selecting a good set of redundants is to consider how prospective redundants would react to applied loads. This can be summarized in the following observations.

- (1) It is found that less confusion results if only shearing stress resultants are made redundants whenever possible.
- (2) For rather obvious reasons, no element should be completely severed from the structure as a result of removing redundants. Adequate connections must be maintained in the primary structure to effectively transmit external loads to the supports.
- (3) Stability of the primary structure prevents certain combinations of redundants. For instance, in Fig. 3.7, if all four forces of  $N_2, N_6, N_{10}$  and  $N_{14}$  were removed, the beam would not be geometrically stable.
- (4) Static determinacy of the primary structure as a rigid body sometimes requires certain stresses to be removed as redundants. The left half of the wall-beam in Fig. 3.7, for example, is equivalent to a beam resting on four rollers located at the centres of interfaces 2, 6, 10 and 14, respectively. Any two

of these must be removed in order that the primary structure may be analysed using the equations of equilibrium alone.

- (5) When the correct number of redundants are chosen, each self-equilibrating system, such as indicated in Fig. 3.8b, is unique.

As a result of these considerations,  $S_1, S_3, S_5, S_7, S_9, S_{11}, N_6$  and  $N_{10}$  are chosen as redundants. Figs. 3.8a and 3.8b show the effects on the primary structure of applied loads and of  $S_3 = 1$ , respectively. It should be noted that the sketching of self-equilibrating systems like these is equivalent to solving the set of equilibrium equations by setting, in turn, all redundants but one equal to zero. The  $N_i$  and  $S_i$  thus generated are then divided by the appropriate lengths to give the stresses which, together with the area of each element, are then fed into the computer to obtain the flexibility coefficients  $[d]$  and the load terms  $[D^0]$ . Results from the computer give, assuming Poisson's ratio  $\mu = 0.167$ ,

$$[d] = \begin{bmatrix} 6.889 & 4.445 & 2.445 & 0.0 & 0.0 & 0.0 & 0.042 & 0.042 \\ 4.445 & 4.889 & 2.445 & 0.0 & 0.0 & 0.0 & 0.028 & 0.056 \\ 2.445 & 2.445 & 2.889 & 0.0 & 0.0 & 0.0 & -0.014 & 0.014 \\ 0.0 & 0.0 & 0.0 & 2.889 & -0.278 & 0.0 & 0.176 & 0.268 \\ 0.0 & 0.0 & 0.0 & -0.278 & 2.889 & -0.278 & -0.027 & 0.027 \\ 0.0 & 0.0 & 0.0 & 0.0 & -0.278 & 2.889 & -0.268 & -0.176 \\ 0.042 & 0.028 & -0.014 & 0.176 & -0.027 & -0.268 & 0.994 & 0.451 \\ 0.042 & 0.056 & 0.014 & 0.268 & 0.027 & -0.176 & 0.451 & 0.994 \end{bmatrix}$$

which is, of course, a symmetric matrix.

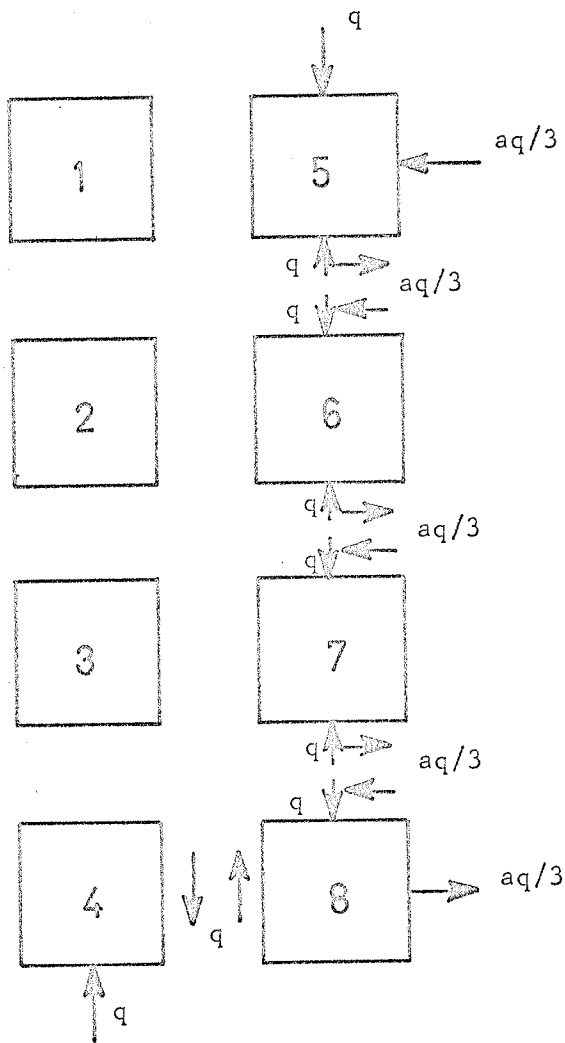


Fig. 3.8a - Applied Loads on Primary Structure

Square elements with  $b = a$

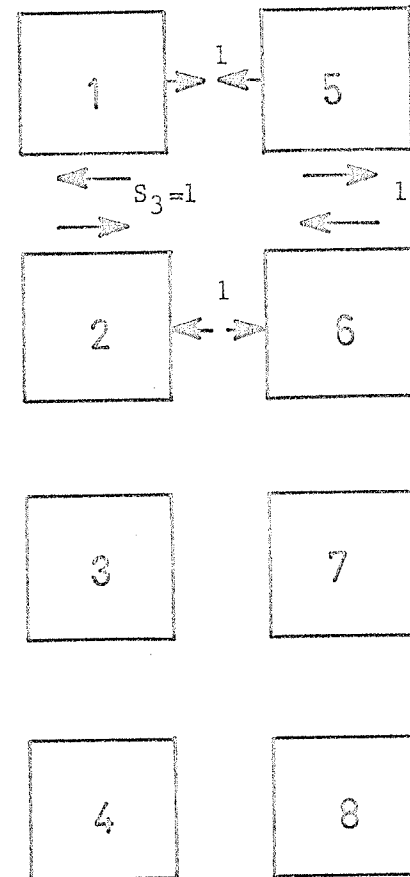


Fig. 3.8b - Self-Equilibrating System for  $S_3 = 1$

Also obtained is

$$[D^0] = [3.611 \quad 2.625 \quad 1.625 \quad 0.268 \quad 0.389 \quad 0.310 \quad 0.030 \quad 0.012]$$

Therefore, referring to equation (3.9a) and putting

$$[X] = [S_1 \quad S_3 \quad S_5 \quad S_7 \quad S_9 \quad S_{11} \quad N_6 \quad N_{10}]$$

and solving, one gets

$$[S_1 \quad S_3 \quad S_5 \quad S_7 \quad S_9 \quad S_{11} \quad N_6 \quad N_{10}] = [-0.419 \quad -0.109 \quad -0.900 \quad -0.158 \quad -0.132 \quad -0.124 \quad -0.052 \quad 0.048]$$

These values are then directly substituted into the equilibrium equations to obtain the rest of the unknowns. The stresses, obtained by dividing the stress resultants by the appropriate lengths, are listed in Table 3.1 below.

TABLE 3.1 - Stresses at Interfaces

Interface No.	1	2	3	4	5	6	7
$\sigma/q$	-0.109	-0.316	-0.419	-0.581	-0.049	-0.052	-0.509
$\tau/q$	-0.419	0.0	-0.109	-0.207	-0.090	0.0	-0.158
Interface No.	8	9	10	11	12	13	14
$\sigma/q$	-0.491	+0.034	+0.048	-0.640	-0.359	+0.124	+0.318
$\tau/q$	-0.210	-0.132	0.0	-0.124	-0.196	-0.359	0.0

Values of  $\sigma_x$  along centre-line of the wall-beam are plotted in Fig. 3.9. The curve compares very favorably with results for a similar problem obtained by Conway et al <sup>(3)</sup>, considering the coarseness of the discretization used.

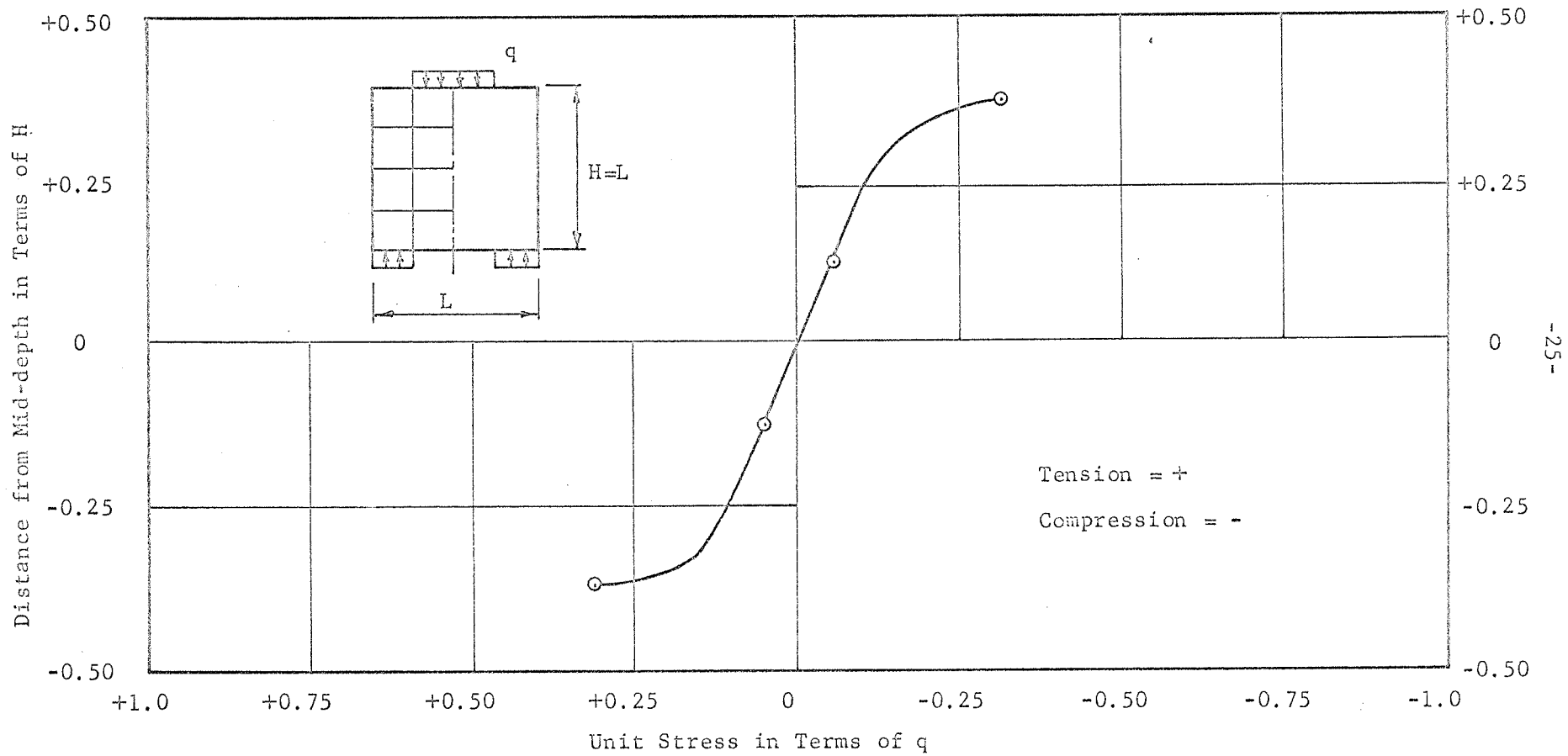


Fig. 3.9 -  $\sigma_x$  at Centre-Line of Wall-Beam

#### 4. ANALYTICAL SOLUTION TO PROBLEMS OF DEEP BEAMS WITH OPENINGS

Of the six beams photoelastically investigated, Fig. 5.1, only B-2 was analytically studied. It was felt that reasonable agreement between the experimental and theoretical solutions would serve to confirm the correctness of both techniques.

##### 4.1 Discretization

There is symmetry in loading and in the geometry of beam B-2, so only half of it need be considered (Fig.4.1). The curvilinear boundary of the circular opening is approximated by straight lines, thus making the elements bordering the opening trapezoidal. Rectangular elements are used elsewhere. Finer strips of elements at the concentrated load and at the support are justified, because this particular method assumes point loads to be distributed over the faces of the elements they act on. A finer element, therefore, would reduce the magnitude of errors introduced by this assumption.

Stress concentration around the opening is most expediently studied photoelastically, hence no unduly fine discretization is used in this region. It should be pointed out that the amount of numerical computations is proportional to the square of the number of interfaces. Thus, refinements of discretization which do not result in appreciable improvement in accuracy are not justified.

Fig. 4.1 shows the left half of the beam divided into 36 elements with 64 interfaces. Applying equation (3.3), it is seen that there are  $2(64 - 36)$  or 56 redundants, of which  $S_6, S_{18}, S_{29}, S_{40}, S_{52}$  and  $S_{64}$  are zero due to symmetry. Thus the resulting structural system is

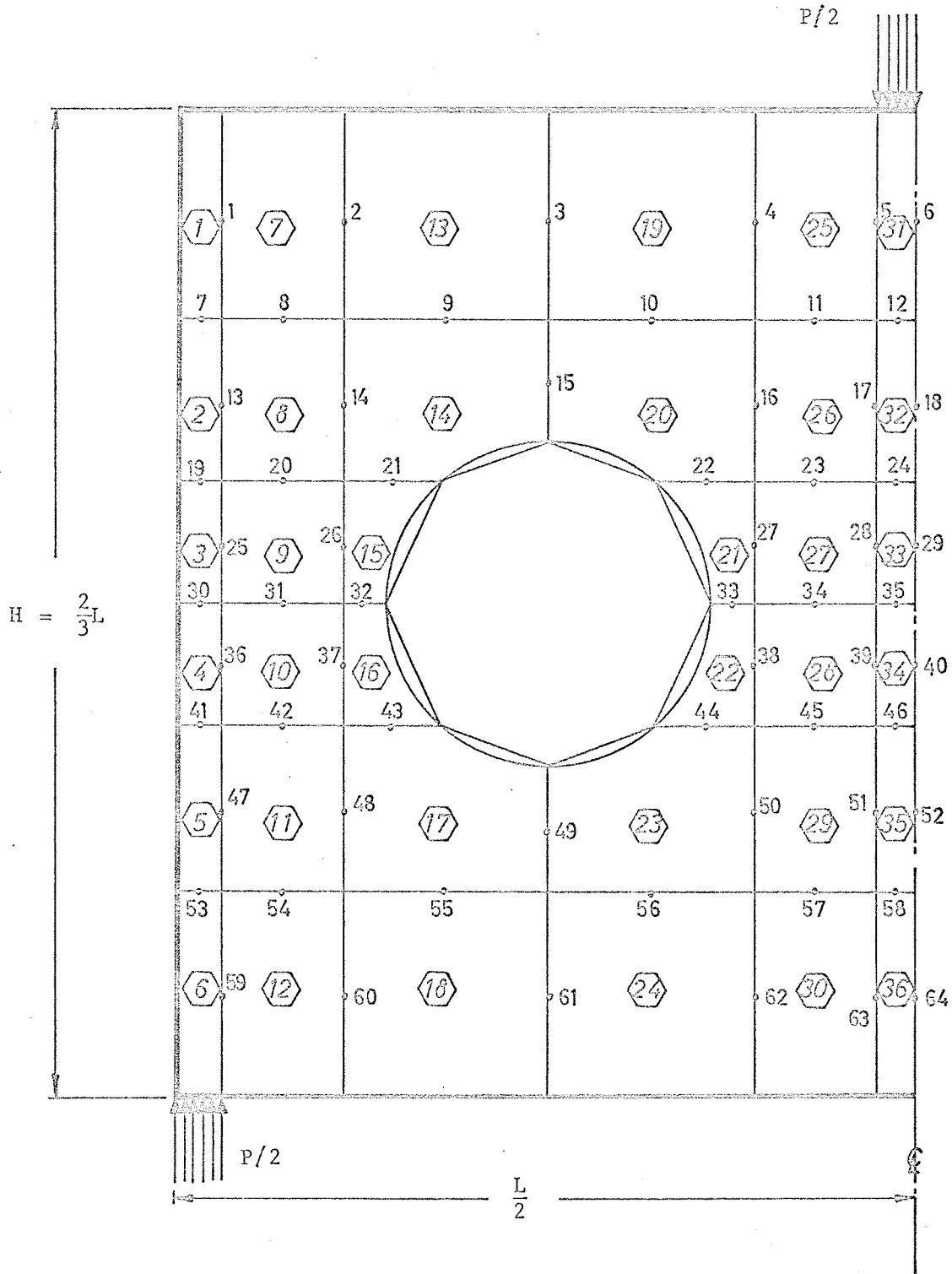


Fig. 4.1 - Discretization of Beam B-2

indeterminate 50 times.

#### 4.2 Selection of Redundants

To begin with,  $N_{18}$ ,  $N_{29}$ ,  $N_{40}$  and  $N_{52}$  are considered redundant to ensure static determinacy of the primary structure.  $S_{59}$ ,  $S_{60}$ ,  $S_{61}$ ,  $S_{62}$  and  $S_{63}$  are retained in the primary structure for transmission of forces from one strip of elements to another in the vertical direction, and  $S_{12}$ ,  $S_{24}$ ,  $S_{35}$ ,  $S_{46}$  and  $S_{58}$  are retained for the similar reason, but in the horizontal direction.

When dealing with multiply-connected bodies, special care should be taken not to remove shear resistance on too many interfaces, or a portion of the body may be completely severed. For example, it is obvious that any two of  $S_{21}$ ,  $S_{32}$  and  $S_{43}$  must be retained, otherwise either the strip of elements 3-9-15 or 4-10-16 will be completely separated from the main body when the other shears are set to zero during the process of evaluating flexibility coefficients. Consequently,  $S_{21}$  and  $S_{43}$  are not considered as redundants. All shearing forces, apart from the ones mentioned above, are removed from the system to form the statically determinate primary structure. The self-equilibrating system corresponding to  $S_{32} = 1$  is illustrated in Fig. 4.2 as an example of 51 such systems, one for each of the 50 redundants set equal to unity and one for the load terms.

#### 4.3 Computations

The program specially written for calculation of flexibility

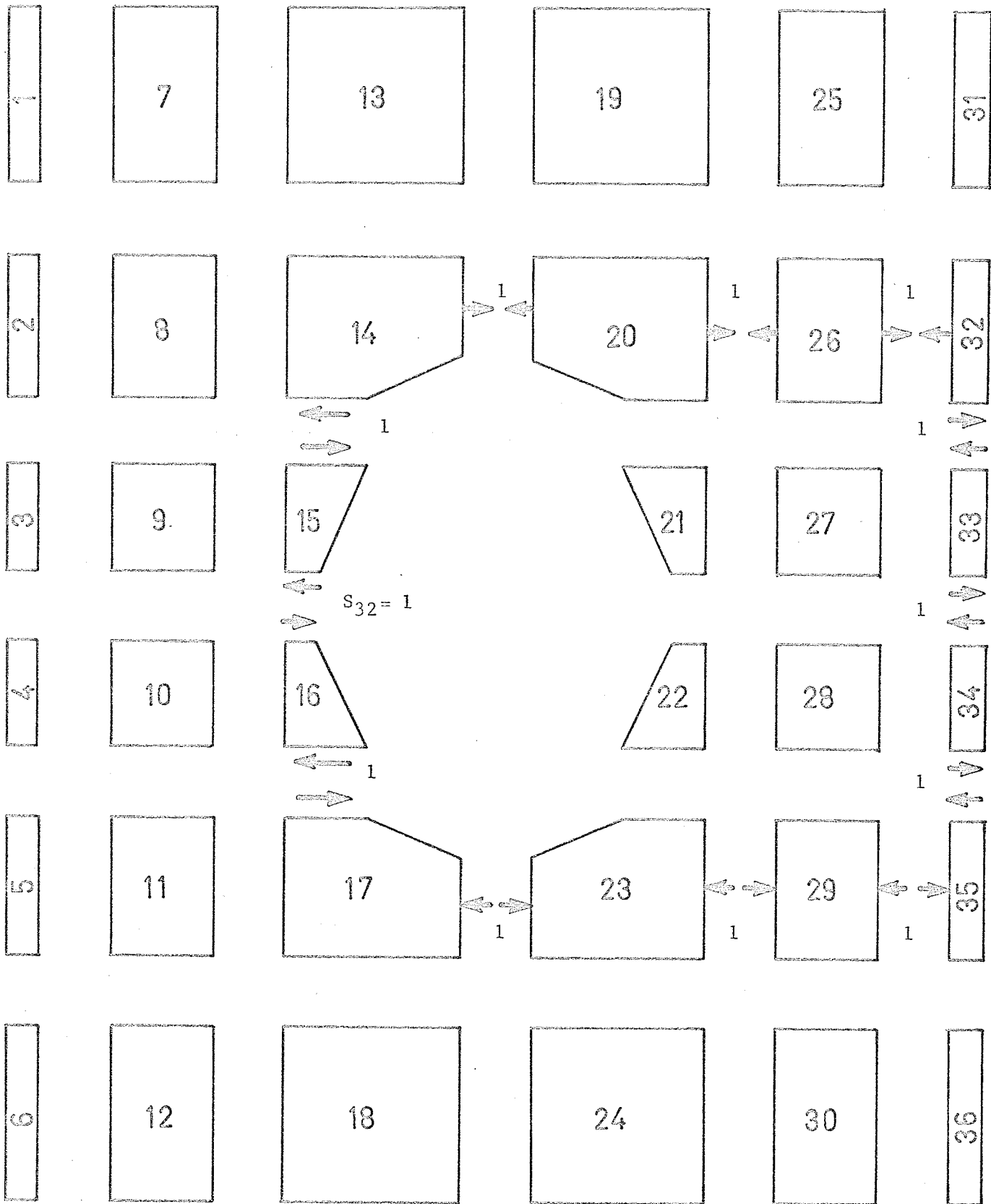


Fig. 4.2 - Self-Equilibrating System for  $S_{32} = 1$

coefficients matrix is linked up with a "simultaneous equations" sub-routine (Fig. B.3, Appendix B) so that the output directly gives the values of the 50 redundant stress resultants (Table 4.1). These are substituted into the equilibrium equations of the type indicated by equations (3.1) and (3.2) to obtain the rest of the stress resultants, which, when divided by appropriate lengths, give the stresses sought (Table 4.2).

Table 4.2 gives stresses in terms of  $(P/Lt)$ . If  $\sigma_s$  is the extreme fibre stress in the beam as predicted by the simple beam theory, then,

$$\begin{aligned}\sigma_s &= \frac{M}{Z} = \frac{(PL/4)}{\frac{1}{6} t(H)^2} \quad \text{for the loading of beam B-2,} \\ &= \frac{PL/4}{\frac{1}{6} t(\frac{2L}{3})^2} = 3.38 \left(\frac{P}{Lt}\right)\end{aligned}$$

Therefore, by dividing each stress by a factor of 3.38, dimensionless ratios are obtained which are plotted and compared to experimental results in Fig. 5.26.

1	-0.9158377E-020	2	-0.2454188E-010	3	-0.1542190E-000	4	-0.2370448E-00
5	-0.4322955E-000	6	-0.1229035E-010	7	-0.3805833E-010	8	-0.7953900E-01
9	-0.1242188E-000	10	-0.1624119E-000	11	-0.1998607E-010	12	-0.1072205E-00
13	-0.9254529E-010	14	-0.6641632E-010	15	0.4352276E-010	16	-0.2253853E-01
17	-0.9940010E-010	18	-0.9521145E-010	19	-0.1458416E-000	20	-0.1407753E-01
21	-0.7251710E-010	22	0.1409882E-010	23	-0.1481089E-010	24	-0.3706156E-01
25	-0.1367319E-000	26	-0.3092605E-010	27	-0.4738479E-010	28	-0.2125802E-00
29	-0.1859222E-010	30	0.4096083E-020	31	-0.6239852E-010	32	-0.9196892E-02
33	-0.3332542E-010	34	-0.9996675E-010	35	-0.6974081E-010	36	-0.1876130E-00
37	0.4350337E-010	38	-0.6102039E-010	39	-0.9535164E-010	40	-0.8005997E-01
41	-0.2209181E-010	42	-0.1361005E-010	43	-0.5936190E-010	44	-0.1143084E-00
45	-0.2234146E-010	46	-0.1704224E-000	47	-0.3773182E-020	48	-0.2757382E-01
49	0.1878133E-010	50	0.5517538E-010				

-31-

TABLE 4.1 - Redundant Stress Resultants  
in Beam B-2

TABLE 4.2 - Stresses in Beam B-2

Interface, i	Length, L/36	$N_i, P$	$\sigma'_i, P/Lt$	$S_i, P$	$\tau_i, P/Lt$
1	5.0	-0.012	-0.086	-0.009	-0.065
2	5.0	-0.050	-0.360	-0.025	-0.180
3	5.0	-0.130	-0.935	-0.154	-1.110
4	5.0	-0.254	-1.830	-0.237	-1.710
5	5.0	-0.416	-3.0	-0.483	-3.470
6	5.0	-0.450	-3.240	0.0	0.0
7	1.0	-0.009	-0.324	-0.012	-0.423
8	3.0	-0.016	-0.192	-0.038	-0.455
9	5.0	-0.129	-0.930	-0.080	-0.575
10	5.0	-0.083	-0.598	-0.124	-0.891
11	3.0	-0.246	-2.950	-0.162	-1.940
12	1.0	-0.017	-0.611	-0.034	-1.220
13	4.0	-0.017	-0.152	-0.020	-0.180
14	4.0	-0.082	-0.738	-0.107	-0.963
15	2.875	-0.079	-0.990	-0.093	-1.160
16	4.0	-0.054	-0.486	-0.066	-0.594
17	4.0	-0.038	-0.342	+0.044	+0.406
18	4.0	-0.004	-0.036	0.0	0.0
19	1.0	-0.029	-1.040	-0.029	-1.040
20	3.0	-0.103	-1.240	-0.099	-1.185
21	2.375	-0.115	-1.740	-0.077	-1.160
22	2.375	-0.056	-0.850	-0.095	-1.440

TABLE 4.2 - Continued

Interface, $i$	Length, $L/36$	$N_i, P$	$\sigma_i, P/Lt$	$S_i, P$	$\tau_i, P/Lt$
23	3.0	-0.136	-1.630	-0.146	-1.730
24	1.0	-0.061	-2.190	0.0	0.0
25	3.0	-0.008	-0.096	-0.014	-0.168
26	3.0	-0.046	-0.551	-0.073	-0.875
27	3.0	+0.048	+0.575	+0.014	+0.168
28	3.0	-0.019	-0.228	-0.015	-0.180
29	3.0	-0.028	-0.335	0.0	0.0
30	1.0	-0.043	-1.550	-0.037	-1.330
31	3.0	-0.162	-1.930	-0.137	-1.630
32	1.0	-0.042	-1.510	-0.031	-1.120
33	1.0	-0.042	-1.510	-0.047	-1.690
34	3.0	-0.165	-1.980	-0.213	-2.560
35	1.0	-0.046	-1.660	-0.009	-0.324
36	3.0	+0.004	+0.048	-0.019	-0.228
37	3.0	+0.041	+0.491	+0.004	+0.048
38	3.0	-0.014	-0.168	-0.063	-0.755
39	3.0	+0.011	+0.132	-0.009	-0.109
40	3.0	+0.019	+0.228	0.0	0.0
41	1.0	-0.062	-2.230	-0.033	-1.190
42	3.0	-0.139	-1.670	-0.100	-1.200
43	2.375	-0.046	-0.698	-0.074	-1.120
44	2.375	-0.105	-1.590	-0.061	-0.915

TABLE 4.2 - Continued

Interface, i	Length, L/36	$N_i$ , P	$\sigma_i$ , P/Lt	$S_i$ , P	$\tau_i$ , P/Lt
45	3.0	-0.111	-1.220	-0.188	-2.060
46	1.0	-0.037	-1.330	-0.001	-0.036
47	4.0	+0.019	+0.171	+0.044	+0.396
48	4.0	+0.060	+0.540	-0.062	-0.558
49	4.0	+0.020	+0.180	-0.095	-0.855
50	4.0	+0.058	+0.522	-0.080	-0.720
51	4.0	+0.076	+0.684	-0.022	-0.198
52	4.0	+0.055	+0.495	0.0	0.0
53	1.0	-0.018	-0.648	-0.014	-0.503
54	3.0	-0.245	-2.940	-0.059	-0.710
55	5.0	-0.079	-0.570	-0.114	-0.820
56	5.0	-0.090	-0.649	-0.023	-0.156
57	3.0	-0.053	-0.635	-0.170	-2.040
58	1.0	-0.015	-0.540	-0.020	-0.720
59	5.0	+0.014	+0.101	-0.482	-3.470
60	5.0	+0.073	+0.525	-0.237	-1.710
61	5.0	+0.187	+1.850	-0.158	-1.140
62	5.0	+0.210	+1.550	-0.068	-0.490
63	5.0	+0.380	+2.740	-0.015	-0.108
64	5.0	+0.408	+2.940	0.0	0.0

## 5. THE PHOTOELASTIC EXPERIMENT

### 5.1 Fundamental Principles

The basic property required in photoelasticity is that of temporary birefringence, or double refraction, which certain transparent materials exhibit when subjected to stress and strain. When the study is conducted, the loads are applied to the model, and the resulting optical effects in the model are viewed in a field of circularly polarized\* light. With a white light source, the optical effects are manifested in the form of coloured bands covering the range of the spectrum. With monochromatic light source, the optical effects are seen as alternate dark and light bands, referred to as isochromatic fringes. These fringes are ordered according to the darkness brightness cycles that take place at a point in the model as the load is increased from zero to its final value. The fringe orders are commonly related to the stress-optic law which states that, in the case of two-dimensional stress fields, the isochromatic fringes are the loci of points of constant maximum shear stress in the plane of the applied loads.

By the simple process of counting fringes and multiplying their orders by the proper calibration constant, the maximum shear stress

---

\* Photoelastic terms are freely used here without explanations.

Definitions of such terms, together with more detailed mathematical theory behind photoelasticity, are available in any book on fundamental theories, for example, references (4) and (8).

distribution throughout the model can be obtained. Since  $\tau_{\max} = \frac{1}{2} (\sigma_1 - \sigma_2)$ , the difference between the two principal stresses at any point can also be determined. In its mathematical form, the stress-optic law thus becomes

$$\sigma_1 - \sigma_2 = \frac{Nf_{\sigma}}{t}$$

where  $f_{\sigma}$  = material fringe value obtained from calibration,

$N$  = fringe order at point of interest,

and  $t$  = thickness of model.

When viewed in a field of plane polarized white light, another fringe pattern consisting of dark bands is seen to be super-imposed on the coloured isochromatics. These are the isoclinics, loci of points with one of the principal stress directions parallel to the axis of the polarizer.

The isochromatic and isoclinic fringes are the basic raw data obtainable from the photoelastic experiment and may be permanently recorded by photography.

## 5.2 Materials for Photoelastic Models

Apart from basic requirements of transparency and birefringence, a good photoelastic material should exhibit low optical and mechanical creep, high elastic limit, good machinability, low time-edge effect and, above all, low material fringe value and high Young's modulus. The measure for the last two properties is expressed as the ratio  $E/f_{\sigma}$ , known as the figure of merit of the material. In other words, a high figure of merit is desirable.

Araldite belongs to the family of epoxies which are the most recent addition to the list of materials used for the manufacture of photoelastic models. It is mostly used in three-dimensional investigations, but its high sensitivity, low creep and time-edge effects are also ideally suited for two-dimensional studies. It is available in sheets and also in the form of pure resin (liquid or granular) which has to be mixed with a hardener to be polymerized. Casting with liquid araldite was attempted and sheets were obtained which were practically bubble-free and had glossy-smooth surfaces. Residual thermal stresses, however, were considerable and, unfortunately, a proper photoelastic oven, which should give a close control over the cooling rate during the annealing process, was not available in the laboratory where these experiments were conducted. Hence sheet araldite was resorted to. PSM-5, supplied by Photolastic Incorporation of U.S.A., was used in making models for determining isochromatic fringes. Nevertheless, a report on the procedures followed in successfully obtaining satisfactory castings is included in Appendix C, which summarizes the experience gained by the author during the experiment.

To isolate the isoclinics from a mixed pattern of isochromatic and isoclinic fringes, one method used is to continuously vary the loads when the pictures of isoclinics are taken, to blur the images of the isochromatics. On the other hand, if a very insensitive material is used, only the isoclinic pattern will show up clearly in a field of plane polarized white light, perhaps with a few coloured isochromatic fringes around points of load application or stress concentration which can be readily distinguished. Perspex, of material fringe value approximately 700 psi/fr/in, was used in making models for isoclinic determinations.

### 5.3 Experimental Procedures

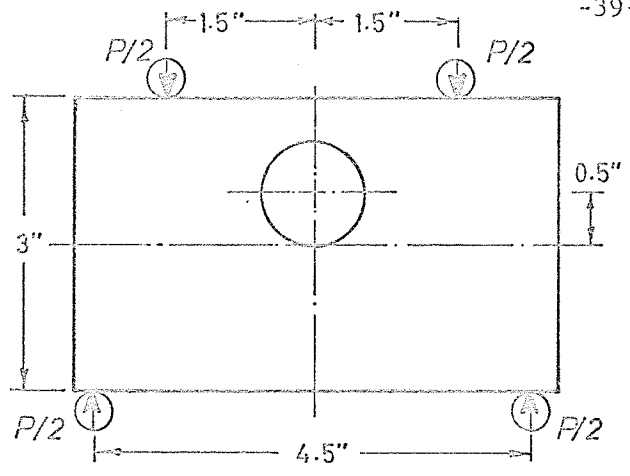
Two series of beams were investigated, each consisting of three beams. Fig. 5.1 illustrates pertinent dimensions and also loading patterns of these beams. All six beams had depth/span ratios of 2/3. Beams of series A were subjected to pure bending by two point loads located at equal distances from either support. Beams of series B were loaded in bending and shear by a concentrated load at mid-span.

Two sets of models were made, each model being inscribed with a 3/8" square grid. The set made of PSM-5 was used for investigating isochromatics, and the set made of perspex for determining isoclinic parameters. A 3"-diameter circular disk was also made from the PSM-5 araldite for calibration of the fringe value of that material. Models were tested the day they were machined. Loads were applied through flat steel bars placed between 1/4" steel rollers and the loading frame. The rollers were padded with two lapses of masking tape. The polariscope used was of the diffused light type with 12"-diameter elements. The preliminary adjustments of the polariscope have been discussed by the author in a previous report (9) and will not be repeated here. The testing included the following steps:

#### (1) Calibration

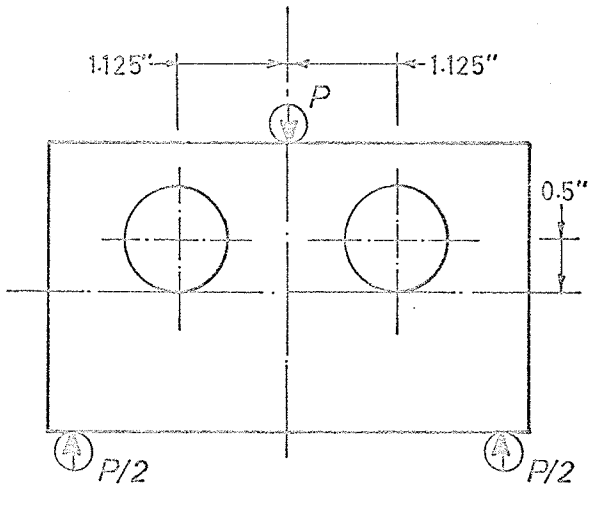
Referring to the ordinate system shown in Fig. 5.2a, it is well known (8) that stresses in the circular disk under diametral compression are

$$\sigma_1 = \sigma_x = \frac{2P}{\pi t D} \left[ \frac{D^2 - 4x^2}{D^2 + 4x^2} \right]^2 ; \quad \text{and} \quad \sigma_2 = \sigma_y = - \frac{2P}{\pi t D} \left[ \frac{4D^4}{(D^2 + 4x^2)^2} - 1 \right]$$



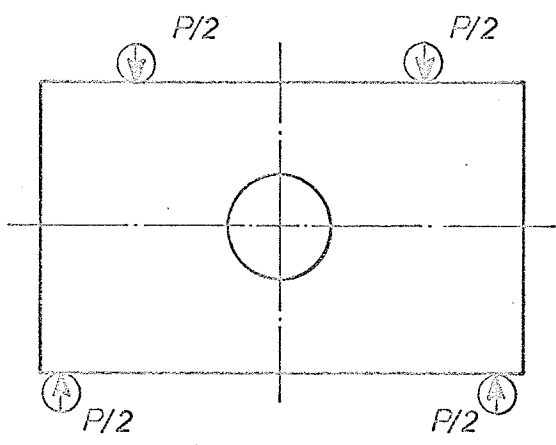
$P_f=400$  lb.,  $P_o=128$  lb.  
 $t=0.25$  in.

BEAM A-1



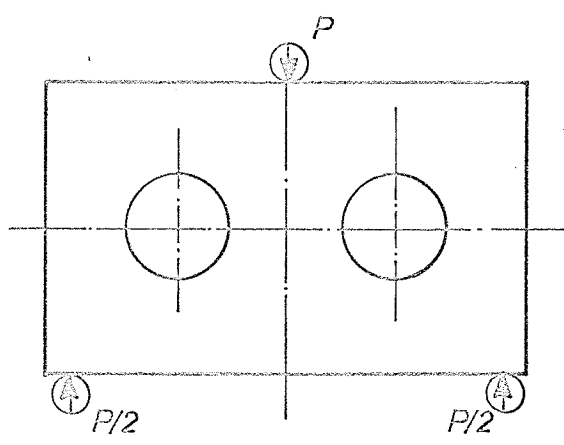
$P_f=216$  lb.,  $P_o=64$  lb.  
 $t=0.25$  in.

BEAM B-1



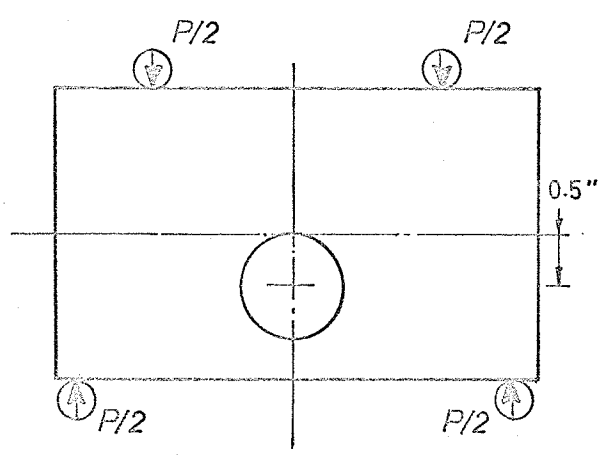
$P_f=480$  lb.,  $P_o=160$  lb.  
 $t=0.24$  in.

BEAM A-2



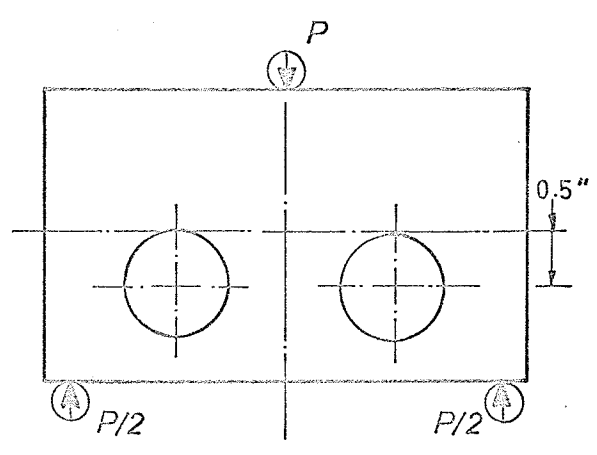
$P_f=240$  lb.,  $P_o=80$  lb.  
 $t=0.24$  in.

BEAM B-2



$P_f=480$  lb.,  $P_o=160$  lb.  
 $t=0.25$  in.

BEAM A-3



$P_f=240$  lb.,  $P_o=80$  lb.  
 $t=0.24$  in.

BEAM B-3

All Openings  
 1-in. Diameter

Fig. 5.1 - Loading Diagrams

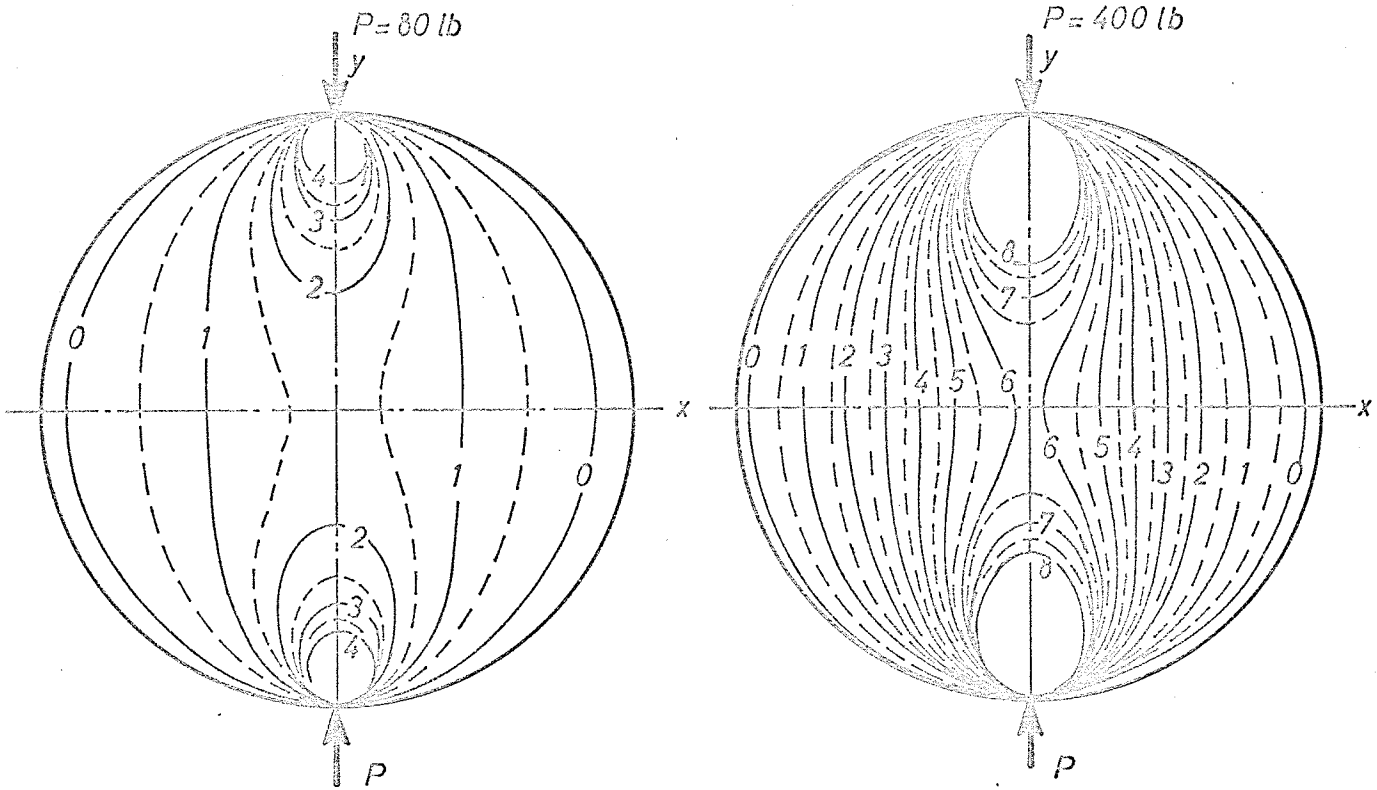


Fig. 5.2a - Isochromatics in Circular Disk Under Diametral Compression

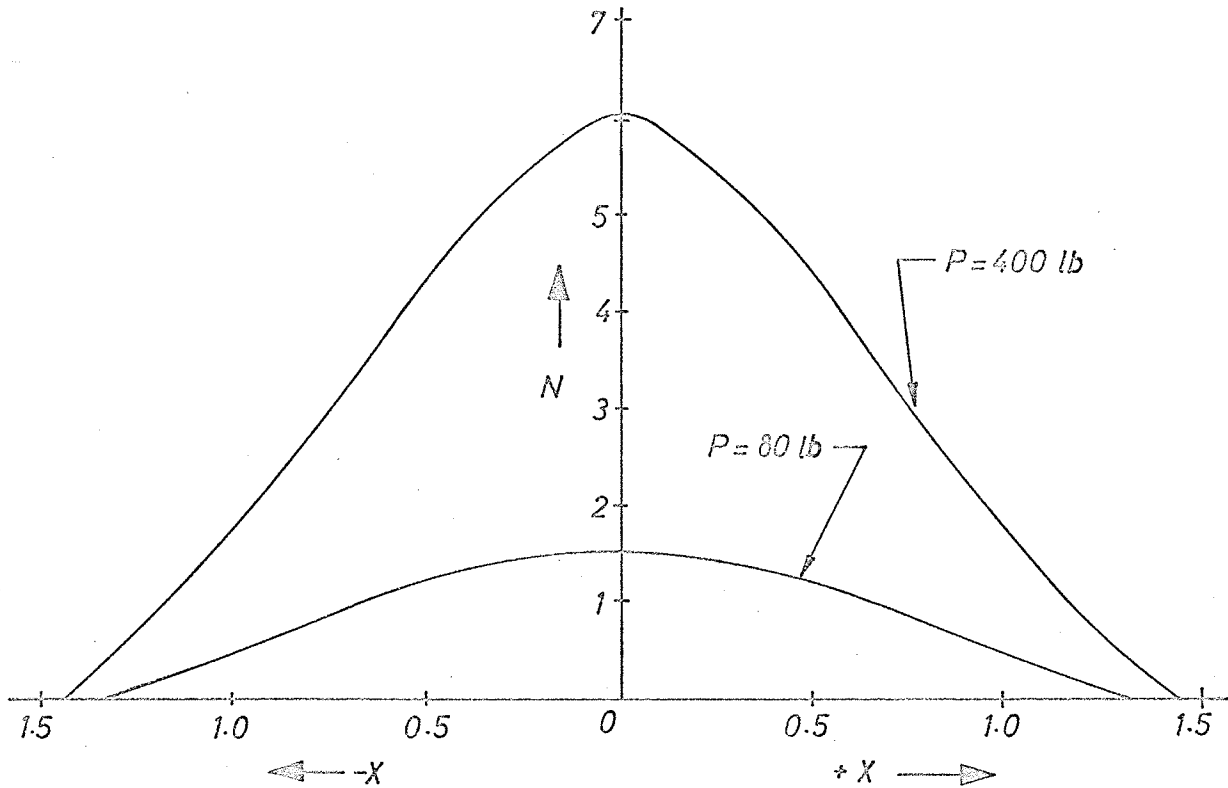


Fig. 5.2b - Variation of Fringe Order Along  $x$ -Axis of Circular Disk

Therefore,

$$\sigma_1 - \sigma_2 = \frac{8P}{\pi t D} \left[ \frac{1 - 4\left(\frac{x}{D}\right)^2}{\left\{1 + 4\left(\frac{x}{D}\right)^2\right\}^2} \right],$$

and when  $x = 0$ ,

$$\sigma_1 - \sigma_2 = \frac{8P}{\pi t D} = f'_{\sigma} N_o$$

where  $P$  = applied diametral compression,

$f'_{\sigma}$  = model fringe value,

$t$  = thickness of disk,

$D$  = diameter of disk,

and  $N_o$  = fringe order at centre of disk.

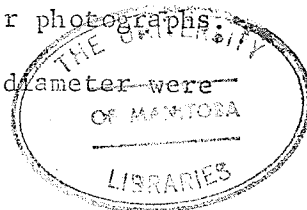
Transposing,

$$f'_{\sigma} = \frac{8P}{\pi t D N_o}$$

Then the material fringe value,

$$f_{\sigma} = f'_{\sigma} t = \frac{8P}{\pi D N_o} \quad (5.1)$$

The disk was placed between two flat steel bars and load applied vertically in its plane. Normal photoelastic procedures were followed to obtain dark and light field patterns at  $P = 80$  lb and  $P = 400$  lb. Pictures were taken of all patterns. Pertinent photographic data will be listed in Table 5.1. Loading cycle and photography were repeated once. Plate 1 shows the matching dark and light field patterns at each of the two loads, while Fig. 5.2a contains sketches of isochromatics plotted with average values obtained from the two sets of similar photographs. Fringe values at varying distances along the horizontal diameter were



plotted (Fig. 5.2b) for both loadings. The difference in  $N_o$  values for the two loads was obtained from this curve. The purpose of working with differences was to eliminate any initial stress that might exist in the material.

$$P_f - P_o = 400 - 80 = 320 \text{ lb.}$$

$$(N_o)_f - (N_o)_o = 4.5 \text{ fr., as obtained from Fig. 5.2b,}$$

where f and o denote final and arbitrary zero loads, respectively.

Substituting into equation (5.1),

$$f_o = \frac{8(320)}{\pi(3)(4.5)} = 60.2 \text{ psi/fr/in.}$$

## (2) Isochromatics and Boundary Values

Each araldite model was loaded in turn,  $P_f$  and  $P_o$  being recorded and shown in Fig. 5.1. The fringe orders at grid points along boundaries, which were direct indications of magnitudes of tangential stresses at these points, were accurately determined to two decimal places using Tardy's compensation method <sup>(8)</sup>. The signs of these boundary stresses were checked by the "nail test" --- when pressure is applied on a nail placed at the boundary point of interest, a flow of fringes towards the point indicates compression, while tension is indicated by the boundary fringe being pushed inside.

The models were observed in white light as load was gradually increased from zero to its final value, to note the order of each fringe formed. The order of the colour bands should be yellow-red-blue-gree, going from a lower to a higher order fringe. This fact was particularly

helpful in determining the orders of fringes around the openings.

Plates 2 to 4 are photographs for the A series models while Plate 5 shows B-1 as an example of the models being stress-free before load application. Sketches of isochromatics at  $P_f$ , together with the accurately determined boundary fringes, are illustrated in Figs. 5.3 to 5.8. These sketches were prepared from enlargements of photographs shown in Plates 2 to 4 and 6 to 8.

### (3) Isoclinics and Identification of $\sigma_1$ and $\sigma_2$

The polariscope was adjusted to give a field of plane polarized white light. Each perspex model was loaded in turn and observed. Load was varied until a clear isoclinic pattern appeared. Photographs were taken at  $10^\circ$  parameters, i.e. the analyser was rotated  $10^\circ$  counterclockwise after each shot, starting from zero. Plate 10 shows a series of such photographs for beam B-2. By projecting the negatives of these photographs onto a sheet of paper placed on the case, a sketch of the isoclinic patterns in beam B-2 was prepared and shown in Fig. 5.9. During this process, the light areas were traced instead of the dark areas since the projection was made from negatives.

Isoclinic parameter at each grid point was obtained by rotating the analyser until an isoclinic passed through that point and noting the reading on the scale.

Since isoclinics do not give information with regard to whether  $\sigma_1$  or  $\sigma_2$  is parallel to the polarizer, this must be determined separately. A strip of very sensitive photoelastic material, PSM-1 ( $f_\sigma = 40$  psi/fr/in), was super-imposed on the point of interest and compressed in the direction of one of the principal stresses, as indicated by the isoclinic parameter previously obtained. An increase in fringe order at the point would

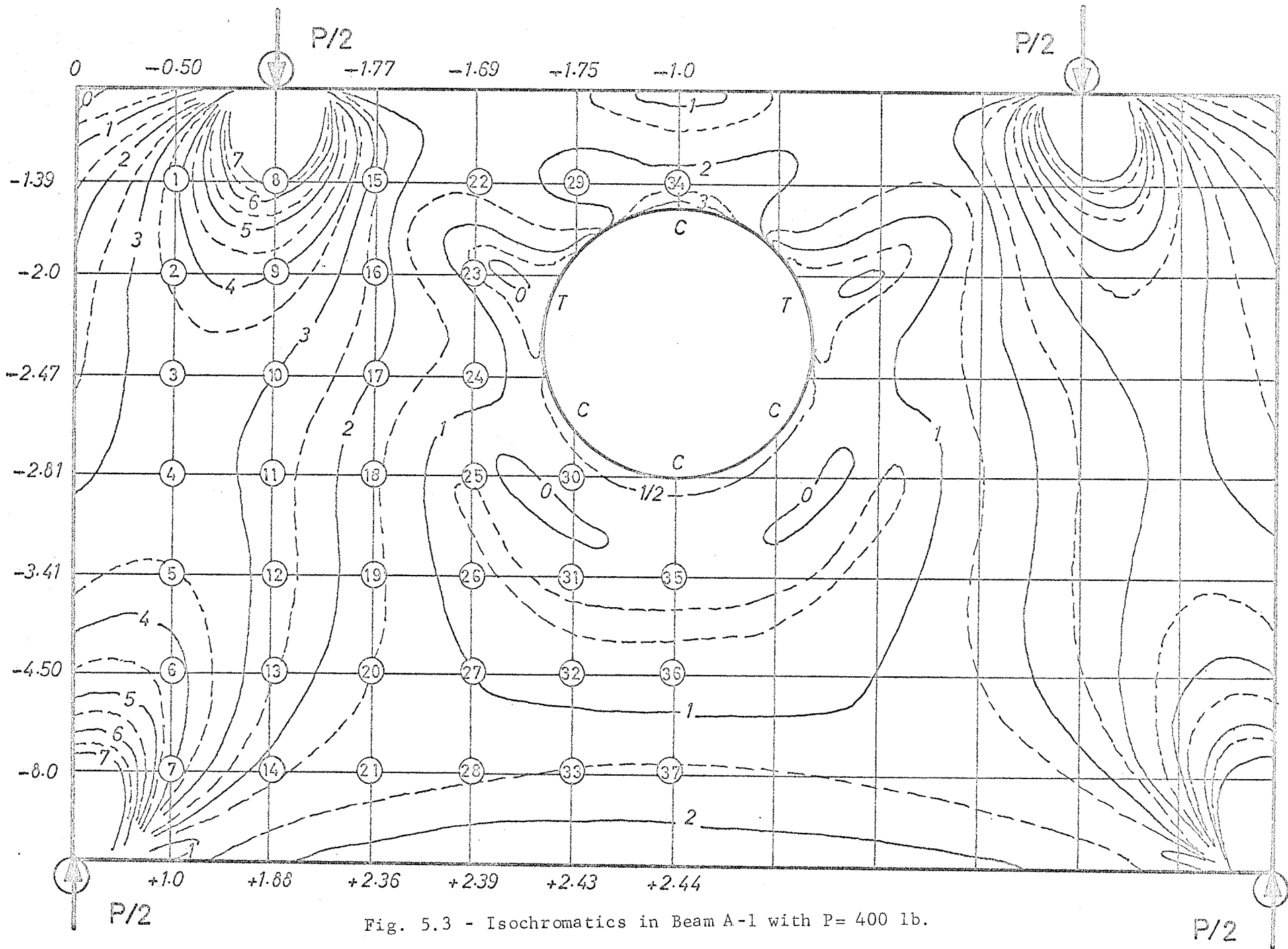


Fig. 5.3 - Isochromatics in Beam A-1 with P= 400 lb.

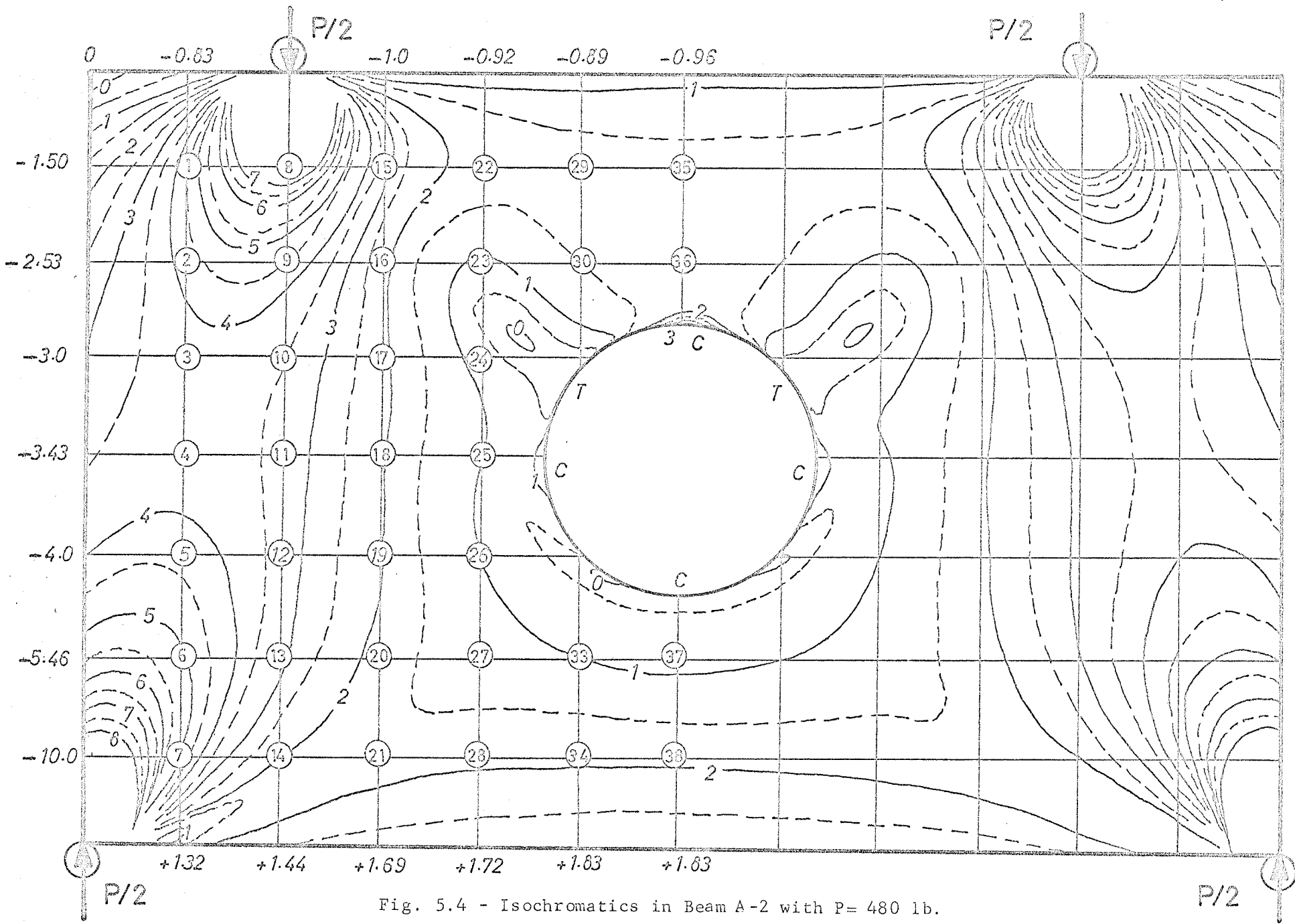


Fig. 5.4 - Isochromatics in Beam A-2 with  $P = 480$  lb.

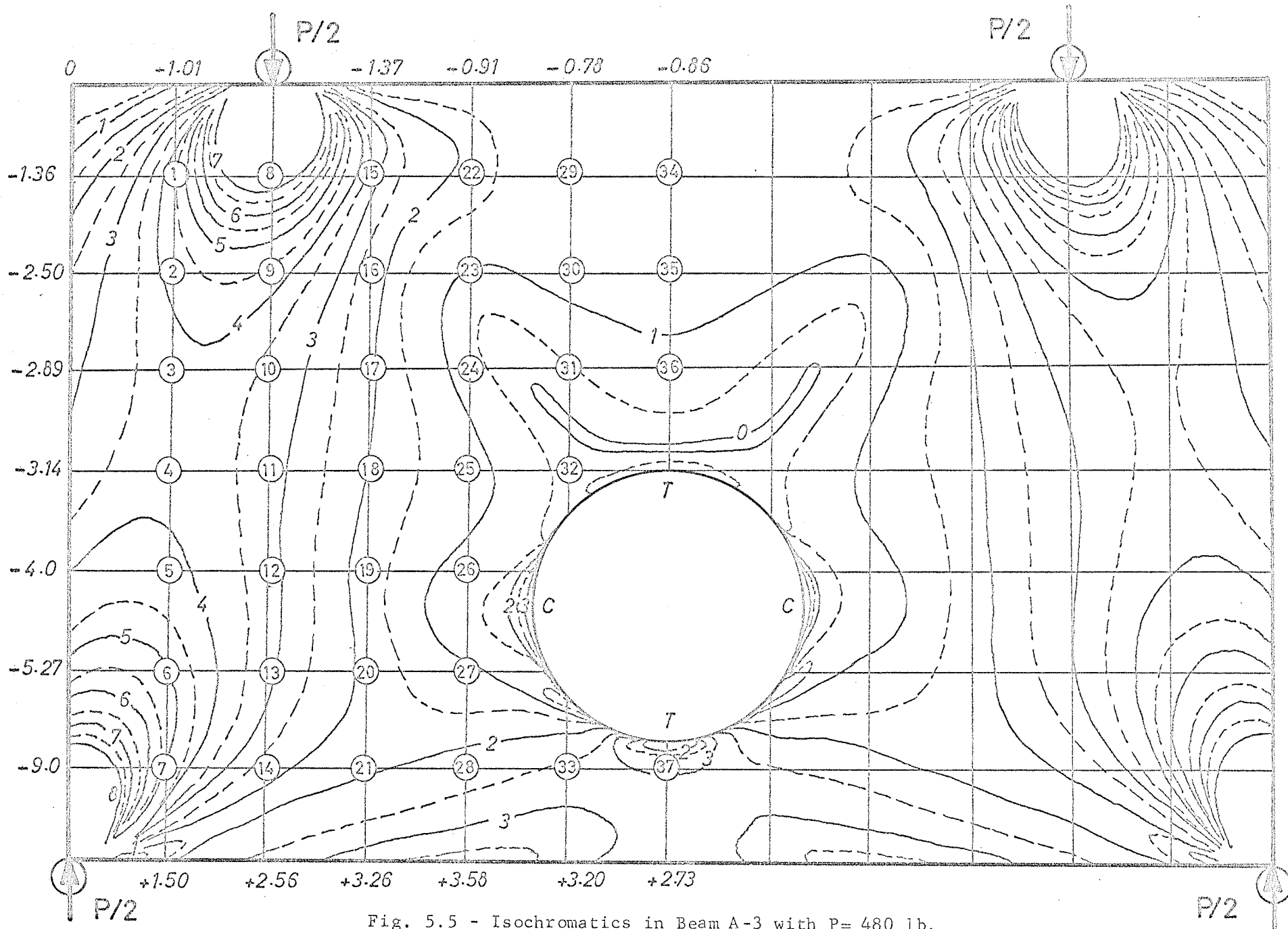


Fig. 5.5 - Isochromatics in Beam A-3 with  $P = 480$  lb.



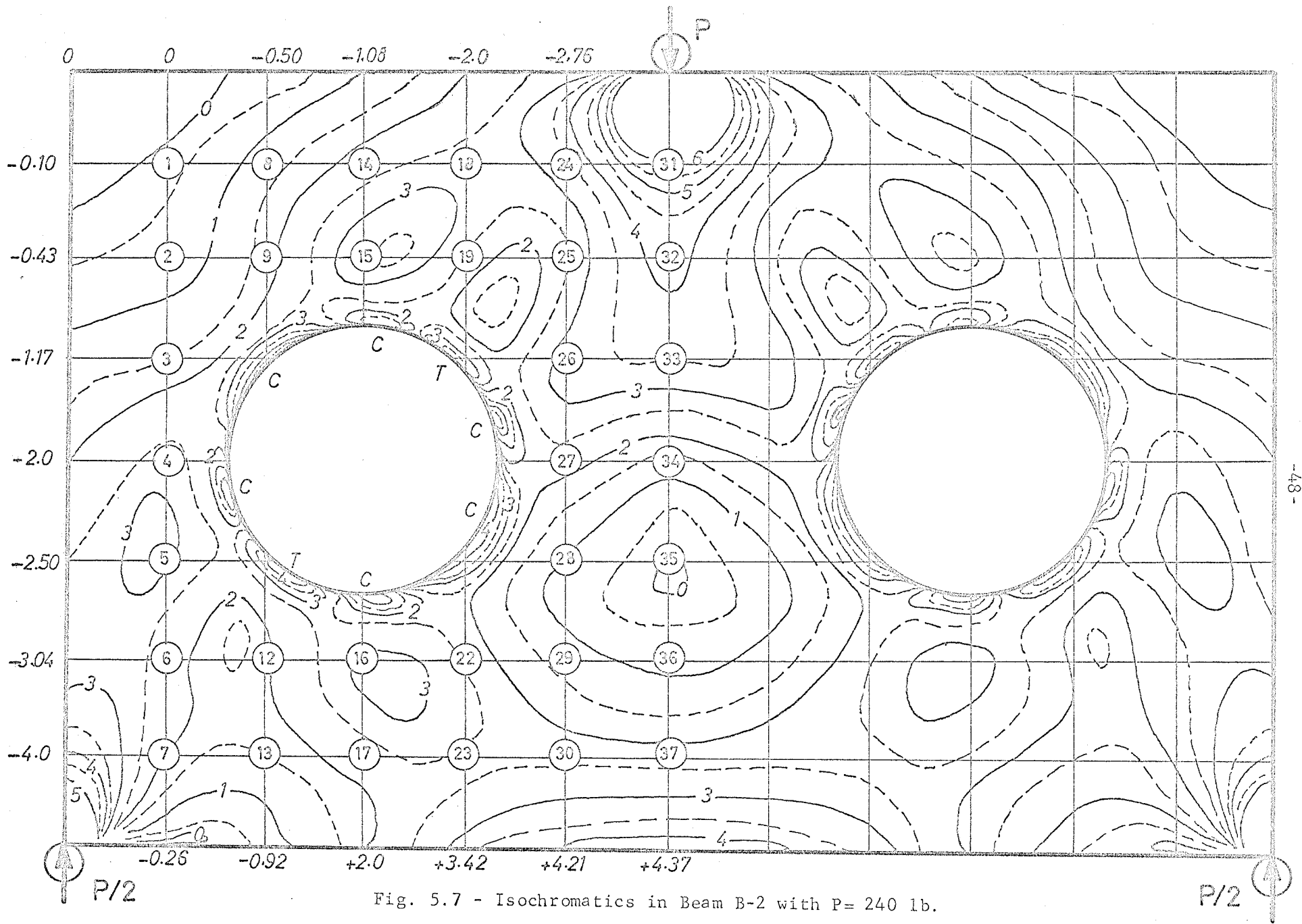


Fig. 5.7 - Isochromatics in Beam B-2 with P= 240 lb.

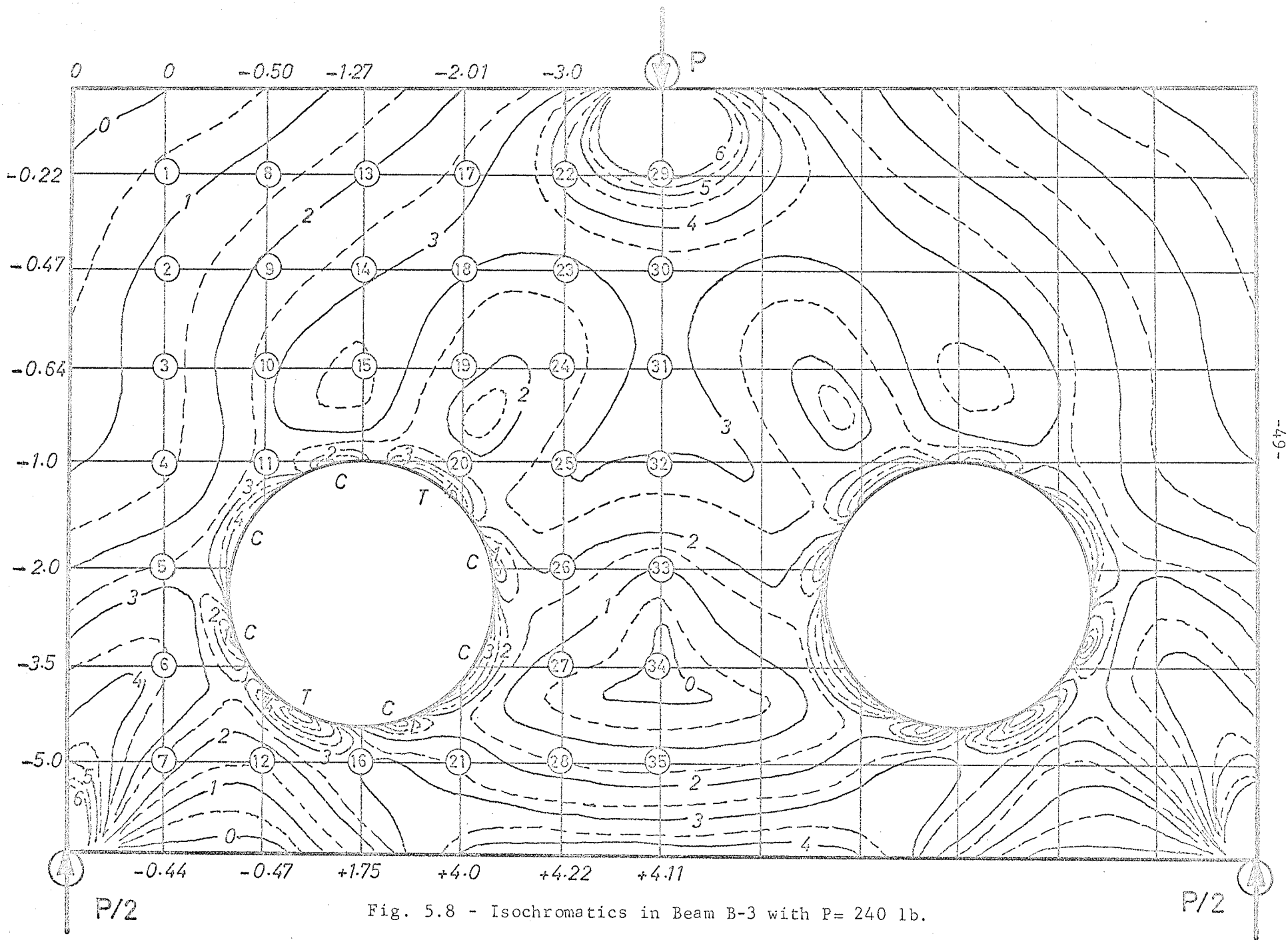


Fig. 5.8 - Isochromatics in Beam B-3 with P= 240 lb.

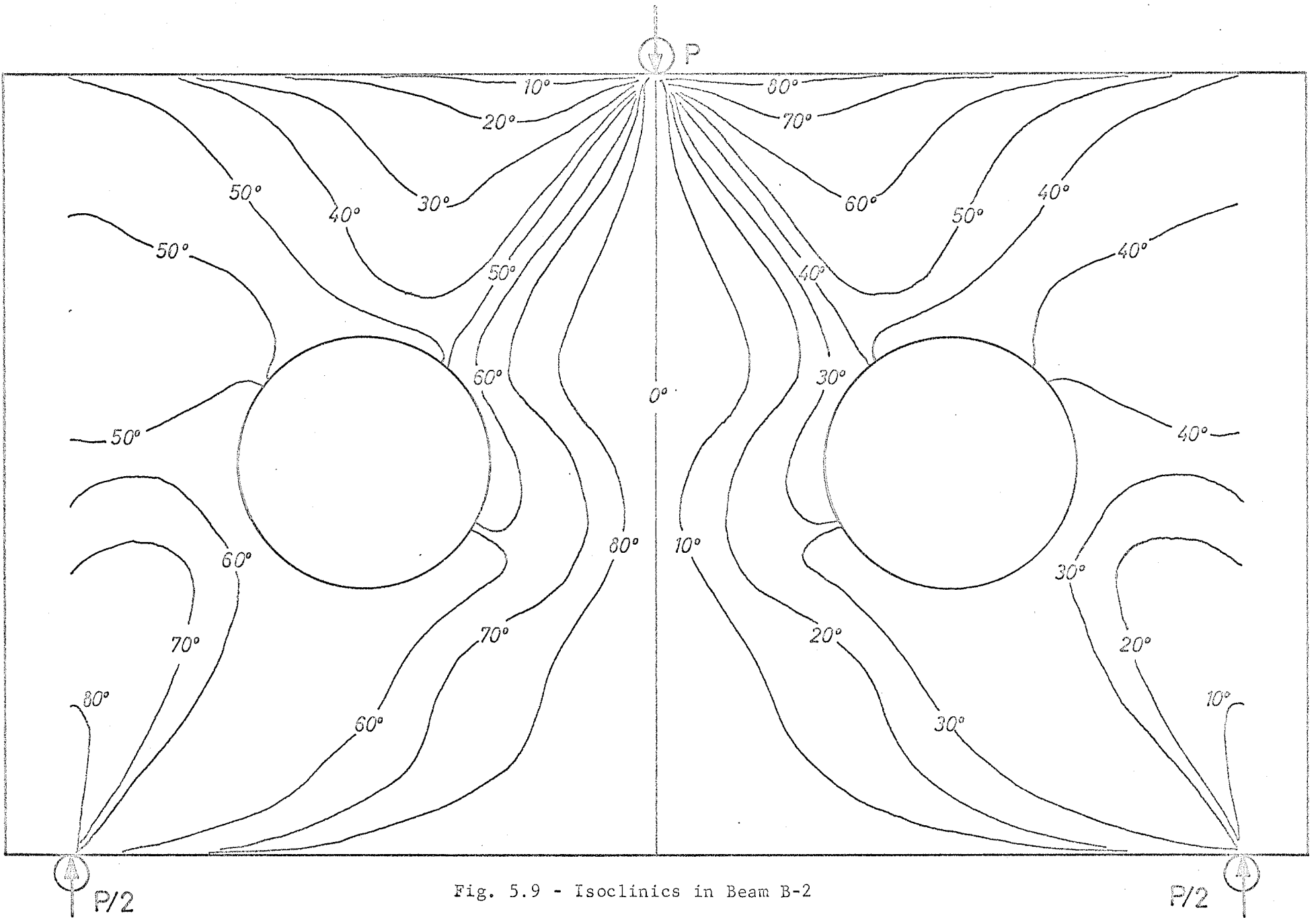


Fig. 5.9 - Isoclinics in Beam B-2

indicate  $\sigma_2$  being parallel to the applied compression. The converse was true when a decrease in fringe order was observed.

(4) Photography

Since only portion of the beam between the supports was of interest, bellows were used to obtain close-ups with the span filling the entire length of the negative frame. Film, filters and paper were selected on the basis of bringing out the high contrast between dark and light areas by suppressing intermediate tones.

Ordinary light meters do not give dependable exposure readings for photography with polarized light, unless it is independently calibrated. Instead of calibrating the meter, exposure was directly calibrated by taking shots over a pre-determined range of exposure-times and judging the developed negatives. Photographic data are listed in Table 5.1 below.

TABLE 5.1 - Photographic Data

Camera:	Minolta SR-T101, SLR
Lens:	Takumar f/4.0 100 mm Bellows
Filter:	Kodak Wratten #77 (Green) for isochromatics. No filter required for isoclinics.
Film:	Kodak High Contrast Copy Film, ASA 0.6
Exposure:	Isochromatics - f/4 at 14 secs. Isoclinics - f/4 at 2.5 secs.
Paper:	Ilford Multigrade with #5 filter.

#### 5.4 Interpretation of Photoelastic Data

Photoelastic data alone are adequate in evaluating boundary stresses. For example, at the boundaries of circular openings, radial stresses,  $\sigma_r$ , are zero and only tangential stresses,  $\sigma_\theta$ , may have values. Therefore, the fringe orders at points along these boundaries, when multiplied by the model fringe value, directly give the values of  $\sigma_\theta$ .

Distribution of  $\sigma_\theta$  around the boundary of the hole of beam A-1 was obtained as a dimensionless plot of the ratios of fringe orders at various  $\theta$  to the maximum fringe order at the lower boundary of the beam. It is equivalent to plotting  $\sigma_\theta/\sigma_m$ , where  $\sigma_m$  is the maximum stress at the extreme bottom fibre of the beam. Figs. 5.11 to 5.15 are similar plots for the other five beams. For beams of series B, the plots are for the left holes, the plots for the right holes being the mirror images of those for the left, since there is symmetry about the centre-line in each beam.

The choice of  $\sigma_m$  as a basis of comparison was not a random one. It was designed to enable a direct estimate of the amount of reinforcement required around the holes, in the case of reinforced concrete members, as compared to the maximum amount of tension steel required elsewhere. The discussion on the application of these results to reinforced concrete will be elaborated in Chapter 6.

#### 5.5 Separation of Principal Stresses

When evaluating separate values of  $\sigma_1$  and  $\sigma_2$  at internal grid points, however, photoelastic data must be supplemented by more information, for example, the value of  $(\sigma_1 + \sigma_2)$  at each grid point. The separation

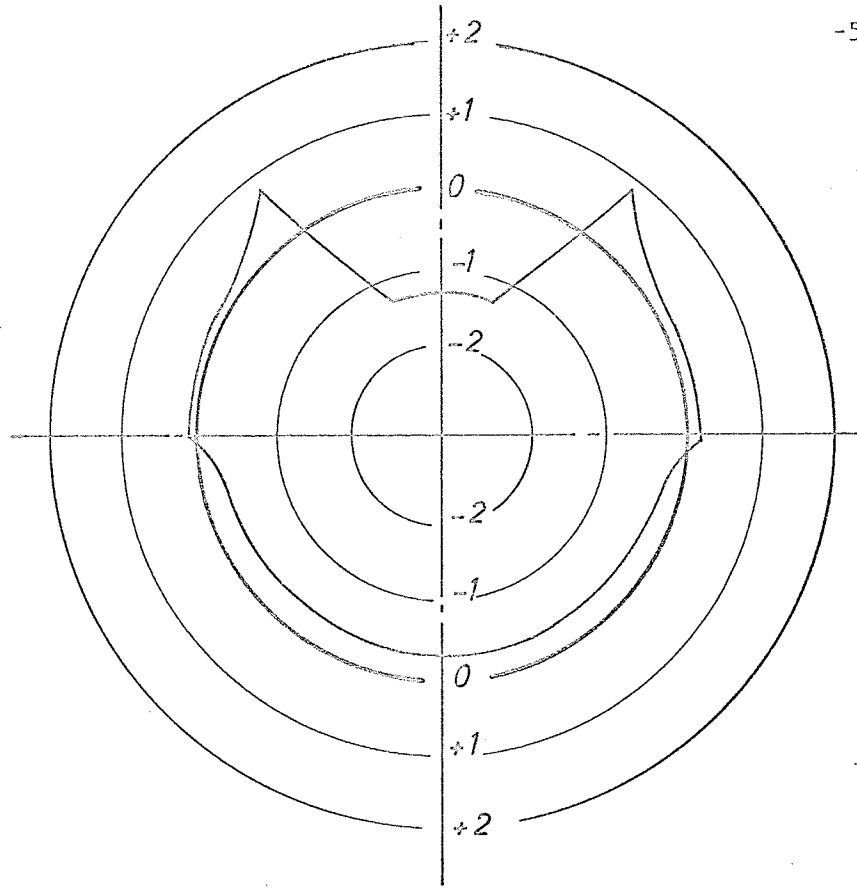


Fig. 5.10 - Variation of  $\sigma_\theta/\sigma_m$  Around Hole of Beam A-1

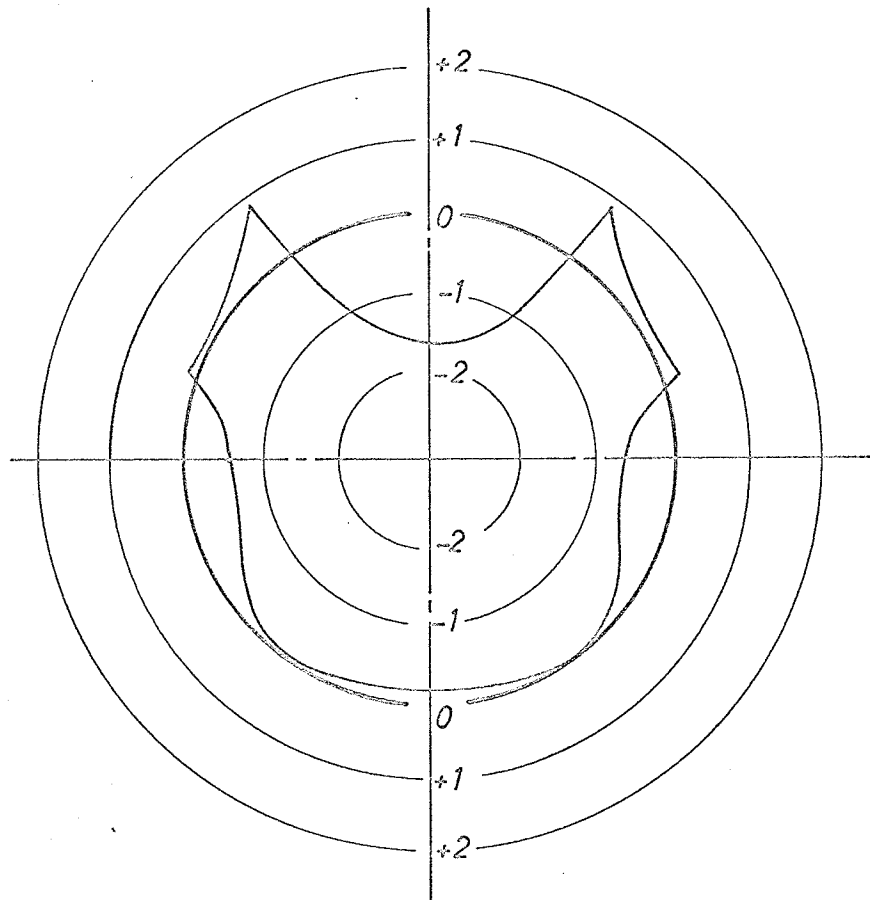


Fig. 5.11 - Variation of  $\sigma_\theta/\sigma_m$  Around Hole of Beam A-2

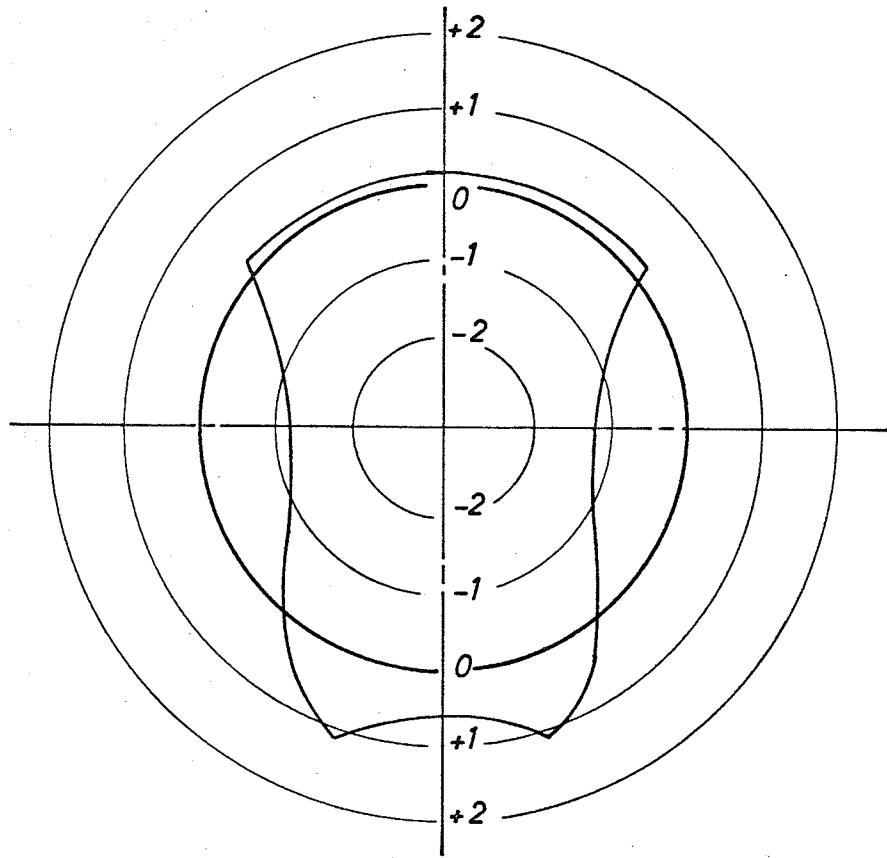


Fig. 5.12 - Variation of  $\sigma_{\theta}/\sigma_m$  Around Hole of Beam A-3

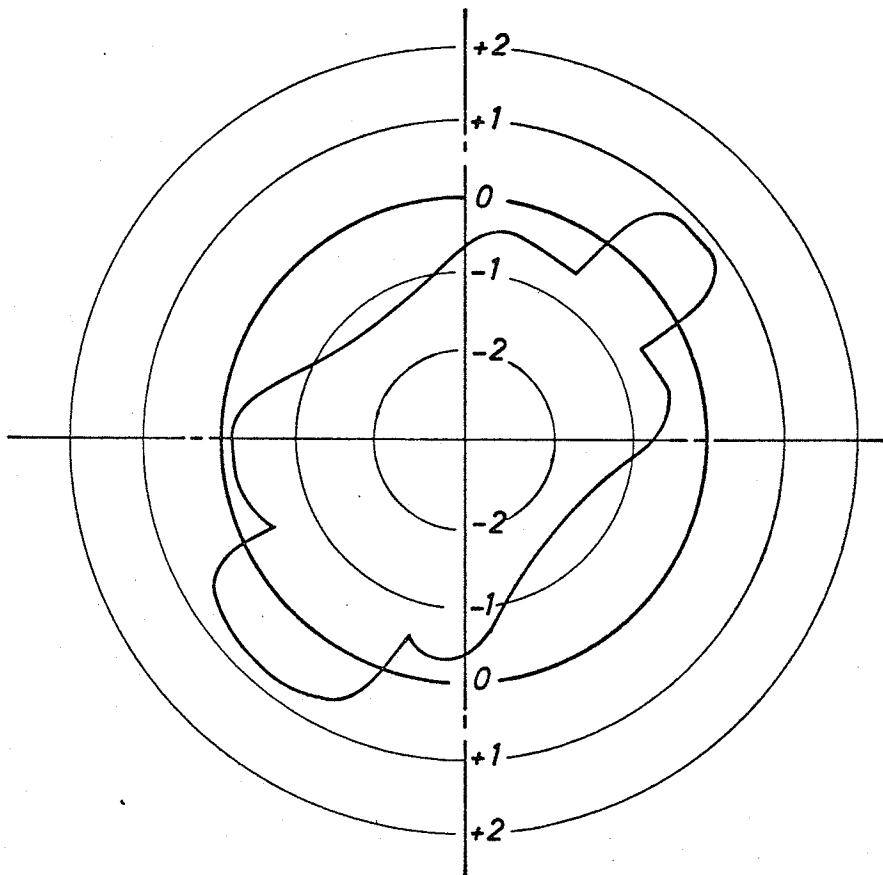


Fig. 5.13 - Variation of  $\sigma_{\theta}/\sigma_m$  Around Left Hole of Beam B-1

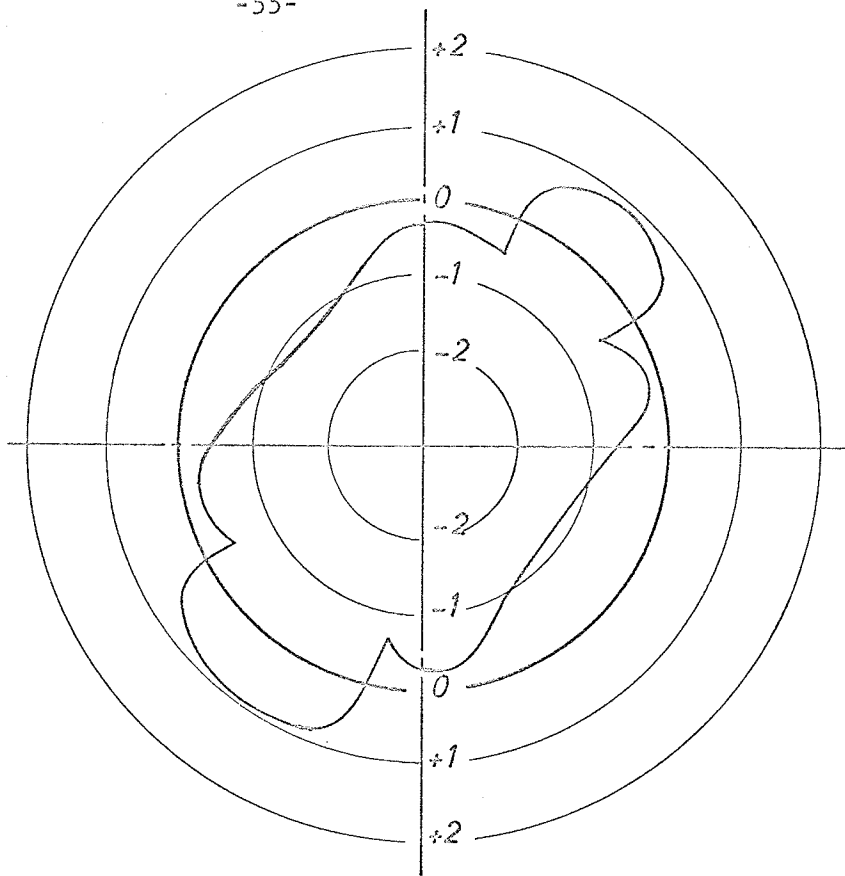


Fig. 5.14 - Variation of  $\sigma_{\theta}/\sigma_m$  Around Left Hole of Beam B-2

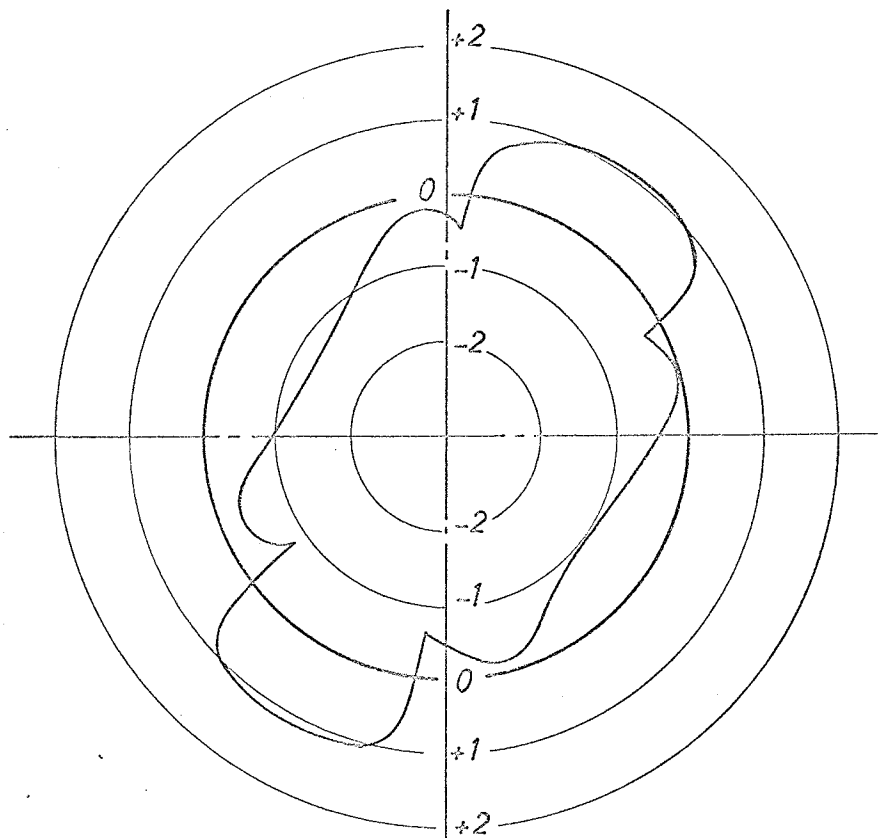


Fig. 5.15 - Variation of  $\sigma_{\theta}/\sigma_m$  Around Left Hole of Beam B-3

technique used in this study was the solution, by the finite difference method (16), of the Laplace equation given below:

$$\left(\frac{\partial^2}{\partial x^2} + \frac{\partial^2}{\partial y^2}\right)(\sigma_1 + \sigma_2) = 0 \quad (5.2)$$

At external boundaries, either  $\sigma_1$  or  $\sigma_2$  is zero. Hence  $(\sigma_1 + \sigma_2)$  is equal to  $\sigma_1$  or  $\sigma_2$ . The Laplace equation may then be solved, in terms of fringes, with boundary values furnished by boundary fringe orders. However, fringe orders at points of application of concentrated loads are indeterminate. To overcome this difficulty,  $(\sigma_1 + \sigma_2)$  was solved for two sets of boundary conditions. The first set assumed zero fringe orders at load points while other boundary grid points maintained their fringe orders as obtained from the experiment. Referring to the grid systems in Figs. 5.3 to 5.8, only half of each beam was considered due to symmetry. The system of algebraic, linear equations resulting from the finite difference analysis was fed into the computer with a "simultaneous equations" program, and outputs were shown in Tables 5.2 to 5.7. Then  $\sigma_1$  and  $\sigma_2$  were evaluated and referred to as solution 1, or  $S_1$ .

The second set of boundary conditions assumed a system of consistent arbitrary fringe orders at load points and zeros at other boundary points.  $(\sigma_1 + \sigma_2)$  was solved for with assumed fringe orders of -200 at P and -100 at P/2. Computer results were listed in Tables 5.8 to 5.13.  $\sigma_1$  and  $\sigma_2$  were again evaluated and referred to as solution 2, or  $S_2$ .

The true solution was  $S = S_1 + CS_2$ , where C was a constant to be

1	7.4605453E 000	2	0.1542006E 010	3	0.2986403E 010	4	0.2573215E 01
5	0.2670255E 010	6	0.2556524E 010	7	0.2950737E-010	8	0.8183408E 00
9	0.1329529E 010	10	0.1815895E 010	11	0.1974100E 010	12	0.2025389E 01
13	0.1860516E 010	14	0.1463994E 010	15	0.1086536E 010	16	0.1043369E 01
17	0.1158656E 010	18	0.1359578E 010	19	0.1570370E 010	20	0.1717522E 01
21	0.1886436E 010	22	0.8726000E 000	23	0.6939598E 000	24	0.3858401E 00
25	0.7367930E 000	26	0.1204741E 010	27	0.1607060E 010	28	0.1958761E 01
29	0.1990642E-010	30	-0.2924924E-020	31	0.9454952E 000	32	0.1581697E 01
33	0.1888003E 010	34	-0.1495719E 010	35	0.9569278E 000	36	0.2104260E 01
37	0.1334224E 010						

TABLE 5.2 - Solution 1 for  $(\sigma_1 + \sigma_2)$  of Beam A-1

1	0.4997192E 000	2	0.1469862E 010	3	0.2213561E 010	4	0.2731014E 01
5	0.3299830E 010	6	0.4024659E 010	7	0.4021544E 010	8	0.7020220E 00
9	0.1161359E 010	10	0.1594681E 010	11	0.1977153E 010	12	0.2363455E 01
13	0.2642932E 010	14	0.2422318E 010	15	0.7073196E 000	16	0.9029813E 00
17	0.1047388E 010	18	0.1187939E 010	19	0.1473421E 010	20	0.1751922E 01
21	0.1815413E 010	22	0.7107799E 000	23	0.6113979E 000	24	0.5762573E 00
25	0.1592905E 000	26	0.5909557E 000	27	0.1111300E 010	28	0.1489253E 01
29	0.4911156E 000	30	0.1612981E 000	31	0.4858522E 000	32	-0.3806986E 00
33	0.6687258E 000	34	0.1314385E 010	35	0.3039426E 000	36	-0.9431689E 00
37	0.6299742E 000	38	0.1266123E 010				

TABLE 5.3 - Solution 1 for  $(\sigma_1 + \sigma_2)$  of Beam A-2

1	0.5624859E 000	2	0.1465957E 010	3	0.2121032E 010	4	0.2566278E 01
5	0.3149792E 010	6	0.3881282E 010	7	0.3979694E 010	8	0.7757265E 00
9	0.1182992E 010	10	0.1527405E 010	11	0.1799096E 010	12	0.2118501E 01
13	0.2532537E 010	14	0.2759053E 010	15	0.9254879E 000	16	0.9847172E 00
17	0.1035597E 010	18	0.9762757E 000	19	0.9216803E 000	20	0.1333735E 01
21	0.2229276E 010	22	0.8800656E 000	23	0.8147219E 000	24	0.6759295E 00
25	0.2577935E 000	26	-0.8530177E 000	27	-0.4577935E 000	28	0.1747396E 01
29	0.7865694E 000	30	0.7095004E 000	31	0.5459146E 000	32	0.2319762E 00
33	0.1638101E 010	34	0.7718090E 000	35	0.6811600E 000	36	0.5487460E 00
37	0.1314373E 010						

TABLE 5.4 - Solution 1 for  $(\sigma_1 + \sigma_2)$  of Beam A-3

1	-0.3469615E 000	2	-0.2388542E 000	3	0.3245788E 000	4	0.7480659E 00
5	0.1040016E 010	6	0.1297976E 010	7	0.1084111E 010	8	-0.1089925E 00
9	0.2376739E 000	10	0.5842008E 000	11	0.7916663E 000	12	0.5121652E 00
13	0.1052132E 010	14	0.1632661E 000	15	0.7074673E 000	16	0.1133686E 01
17	0.2163947E 010	18	-0.2575074E 010	19	-0.2918705E 000	20	0.8118634E 00
21	0.1722922E 010	22	0.1712710E 010	23	0.8679895E 000	24	-0.1632104E 01
25	-0.1212776E 010	26	0.1595001E-020	27	0.1061321E 010	28	0.2134365E 01
29	0.1128916E 010	30	0.4351606E 000	31	-0.7293968E 000	32	-0.6455380E 00
33	0.7425196E 000	34	0.1243860E 010	35	0.2286151E 010		

TABLE 5.5 - Solution 1 for  $(\sigma_1 + \sigma_2)$  of Beam B-1

1	-0.3045548E 000	2	-0.1014091E 010	3	-0.1631509E 010	4	-0.1744092E 00
5	0.1952435E 010	6	0.2174160E 010	7	0.1579804E 010	8	-0.9992373E-01
9	-0.1320035E 010	10	-0.4167538E 010	11	0.3310028E 010	12	0.1585159E 01
13	0.1053575E 010	14	0.6081438E 000	15	0.1402446E-020	16	-0.1970785E 00
17	0.1211337E 000	18	0.1395538E 010	19	0.1494833E 010	20	0.3249836E 01
21	-0.4150606E 010	22	-0.9162146E 000	23	0.9569336E 000	24	0.1578731E 01
25	0.1332517E 010	26	0.8919534E 000	27	-0.1430800E 010	28	-0.1711717E 01
29	-0.2740185E 000	30	0.1722518E 010	31	0.1262927E 010	32	0.1115915E 01
33	0.4162705E 000	34	-0.7693294E 000	35	-0.9914285E 000	36	0.8803225E-01
37	0.1974214E 010						

TABLE 5.6 Solution 1 for  $(\sigma_1 + \sigma_2)$  of Beam B-2

1	0.1203048E 000	2	0.1379012E 000	3	-0.1049229E 000	4	-0.5756298E 00
5	-0.8998419E 000	6	0.5629056E 000	7	0.1518903E 010	8	0.4205642E 00
9	0.1322351E 000	10	-0.5539061E 000	11	-0.2297755E 010	12	0.9527072E 00
13	0.8826379E 000	14	0.4626676E 000	15	-0.1258276E 000	16	-0.9577658E 00
17	0.1367418E 010	18	0.9179393E 000	19	0.7904361E 000	20	0.1930643E 01
21	-0.3414649E-010	22	0.1559960E 010	23	0.1143579E 010	24	0.9856219E 00
25	0.8689873E 000	26	-0.9913701E-010	27	-0.6943803E 000	28	0.1303764E 01
29	0.1269987E 010	30	0.1157732E 010	31	0.9589184E 000	32	0.6583322E 00
33	0.1541243E 000	34	0.2227595E 000	35	0.1743620E 010		

TABLE 5.7 - Solution 1 for  $(\sigma_1 + \sigma_2)$  of Beam B-3

1	-0.1282419E 020	2	-0.7453118E 010	3	-0.3795698E 010	4	-0.1927744E 01
5	-0.9835825E 000	6	-0.4606057E 000	7	-0.5080110E-010	8	-0.2866295E 02
9	-0.1201954E 020	10	-0.5841722E 010	11	-0.3004107E 010	12	-0.1579638E 01
13	-0.7955986E 000	14	-0.3125572E 000	15	-0.1432268E 020	16	-0.9140350E 01
17	-0.5055553E 010	18	-0.2813583E 010	19	-0.1596512E 010	20	-0.8716314E 00
21	-0.3833256E 000	22	-0.4833867E 010	23	-0.3885749E 010	24	-0.2334328E 01
25	-0.1681655E 010	26	-0.1164658E 010	27	-0.7307939E 000	28	-0.3508384E 00
29	-0.1127046E 010	30	-0.4140731E 000	31	-0.6555001E 000	32	-0.5359629E 00
33	-0.2881700E 000	34	-0.2821575E 000	35	-0.4471966E 000	36	-0.4499636E 00
37	-0.2588571E 000						

TABLE 5.8 - Solution 2 for  $(\sigma_1 + \sigma_2)$  of Beam A-1

1	-0.1289104E 020	2	-0.7580484E 010	3	-0.3981030E 010	4	-0.2223451E 01
5	-0.1602870E 010	6	-0.2137299E 010	7	-0.5926690E 010	8	-0.2880327E 02
9	-0.1228594E 020	10	-0.6174454E 010	11	-0.3421113E 010	12	-0.2274521E 01
13	-0.2095222E 010	14	-0.1972342E 010	15	-0.1453539E 020	16	-0.9635444E 01
17	-0.5536496E 010	18	-0.3151284E 010	19	-0.2006996E 010	20	-0.1473542E 01
21	-0.9370788E 000	22	-0.4899573E 010	23	-0.5069084E 010	24	-0.3123758E 01
25	-0.1613886E 010	26	-0.1138929E 010	27	-0.8565738E 000	28	-0.5015566E 00
29	-0.1956888E 010	30	-0.2110531E 010	31	-0.2755805E 000	32	-0.7831675E-01
33	-0.3485830E 000	34	-0.2585928E 000	35	-0.1221928E 010	36	-0.1140589E 01
37	-0.2008502E 000	38	-0.1784655E 000				

TABLE 5.9 - Solution 2 for  $(\sigma_1 + \sigma_2)$  of Beam A-2

1	-0.1297142E 020	2	-0.7722003E 010	3	-0.4147739E 010	4	-0.2374659E 01
5	-0.1712970E 010	6	-0.2203444E 010	7	-0.5956622E 010	8	-0.2898341E 02
9	-0.1260688E 020	10	-0.6552617E 010	11	-0.3750776E 010	12	-0.2494641E 01
13	-0.2217664E 010	14	-0.2025245E 010	15	-0.1485285E 020	16	-0.1022177E 02
17	-0.6246123E 010	18	-0.3727736E 010	19	-0.2310046E 010	20	-0.1621126E 01
21	-0.9957896E 000	22	-0.5394156E 010	23	-0.6053012E 010	24	-0.4467556E 01
25	-0.2624918E 010	26	-0.1310374E 010	27	-0.9920242E 000	28	-0.5301500E 00
29	-0.2622231E 010	30	-0.3548967E 010	31	-0.2801106E 010	32	-0.9919889E 00
33	-0.1327915E 000	34	-0.1959786E 010	35	-0.2779986E 010	36	-0.2130536E 01
37	-0.5323625E-010						

TABLE 5.10 - Solution 2 for  $(\sigma_1 + \sigma_2)$  of Beam A-3

1	-0.5984079E-020	2	-0.1059962E-010	3	-0.4058277E-010	4	-0.1845626E 00
5	-0.5459262E 000	6	-0.1609346E 010	7	-0.5706553E 010	8	-0.1333670E-01
9	-0.1517208E 000	10	-0.5866593E 000	11	-0.1244524E 010	12	-0.1612290E 01
13	-0.5979136E 000	14	-0.3887798E 000	15	-0.6154652E 000	16	-0.5541707E 00
17	-0.3580864E 010	18	-0.2674573E 000	19	-0.2685155E 000	20	-0.2293243E 00
21	-0.1746367E 000	22	-0.1561656E 020	23	-0.8472998E 010	24	-0.3519296E 01
25	-0.1374907E 010	26	0.5850855E-020	27	0.1389085E 000	28	0.2945128E-01
29	-0.5041324E 020	30	-0.1659654E 020	31	-0.6055558E 010	32	-0.1718738E 01
33	0.1968393E 010	34	0.4769865E 000	35	0.1210689E 000		

TABLE 5.11 - Solution 2 for  $(\sigma_1 + \sigma_2)$  of Beam B-1

1	-0.2970776E 000	2	-0.3159218E 000	3	-0.1188021E 000	4	-0.1052163E 00
5	-0.4060972E 000	6	-0.1453793E 010	7	-0.5630260F 010	8	-0.9407077E 00
9	-0.9150348E 000	10	-0.5407032E-010	11	-0.6541842E-010	12	-0.8446643E 00
13	-0.1486345E 010	14	-0.2825097E 010	15	-0.2349396F 010	16	-0.3731408E 00
17	-0.5000610E 000	18	-0.8754105E 010	19	-0.7410051E 010	20	-0.8193600E 00
21	-0.1052791E 000	22	-0.4156420E 000	23	-0.3257370E 000	24	-0.2851883E 02
25	-0.1771651E 020	26	-0.8255647E 010	27	-0.3172175F 010	28	-0.1597243E 01
29	-0.8585160E 000	30	-0.4050667E 000	31	-0.5810899E 020	32	-0.2464873E 02
33	-0.1131439E 020	34	-0.4967625E 010	35	-0.2252950E 010	36	-0.1087296E 01
37	-0.4653398E 000						

TABLE 5.12 - Solution 2 for  $(\sigma_1 + \sigma_2)$  of Beam B-2

1	-0.6845943E 000	2	-0.9789218E 000	3	-0.7796297E 000	4	-0.3227002E 00
5	-0.7073146E-010	6	-0.1744671E-010	7	-0.5916420E-020	8	-0.1816118E 01
9	-0.2511735E 010	10	-0.1858485E 010	11	-0.4404398E 000	12	-0.6218988E-02
13	-0.4262268E 010	14	-0.5509033E 010	15	-0.3857951E 010	16	-0.2224372E-01
17	-0.1049550E 020	18	-0.1145096E 020	19	-0.7678834E 010	20	-0.2570449E 01
21	-0.1047497E 000	22	-0.3015863E 020	23	-0.2091354E 020	24	-0.1235289E 02
25	-0.6225193E 010	26	-0.2377542E 010	27	-0.1103016E 010	28	-0.4520724E 00
29	-0.5965103E 020	30	-0.2748105E 020	31	-0.1467124E 020	32	-0.7600020E 01
33	-0.3513227E 010	34	-0.1546918E 010	35	-0.6005141E 000		

TABLE 5.13 - Solution 2 for  $(\sigma_1 + \sigma_2)$  of Beam B-3

determined by equilibrium considerations. The vertical section at mid-span of each beam was considered for equilibrium. Symmetry dictated that there should be no shear stress along this section which was, therefore, a principal plane. Then  $\sigma'_x = (\sigma'_1 \text{ or } \sigma'_2)$  was plotted for both solutions and the areas under the curves referred to as  $A_1$  and  $A_2$ , respectively. Since there was no horizontal load in any of the cases considered, the true solution should give  $\int \sigma'_x dy = 0$ . That is to say

$$A_1 + CA_2 = 0 \quad (5.3)$$

From equation (5.3), the C values might be obtained. The C values thus determined for each beam are listed below:

<u>Beam</u>	<u>Constant C</u>
A-1	1.560
A-2	1.010
A-3	0.590
B-1	0.132
B-2	0.121
B-3	0.119

Once these constants were determined, it was a simple task to linearly combine the two solutions and obtain the final values of  $\sigma'_1$  and  $\sigma'_2$  in terms of fringes. In Figs. 5.16 to 5.21, these results are presented, together with principal stress directions, as ratios of  $\sigma'_1/\sigma'_s$  and  $\sigma'_2/\sigma'_s$ , where  $\sigma'_s = \frac{M}{Z}$  is the extreme fibre stresses as calculated with

the simple beam theory. It was found to be more convenient to convert  $\sigma_s$  into fringes than to convert other stresses into psi. For instance, for Beam A-1,

$$\begin{aligned} M &= (P/2)(\text{Moment Arm}) \\ &= 200(0.75) = 150 \text{ lb-in.} \\ Z &= \frac{1}{6}tH^2 = \frac{1}{6}t(3)^2 = 1.5t \text{ in}^3 \end{aligned}$$

Therefore,

$$\begin{aligned} \sigma_s &= \frac{M}{Zf_{\sigma}} = \frac{Mt}{Zf_{\sigma}} \\ &= \frac{150t}{1.5t(60.2)} = 1.66 \text{ fringes} \end{aligned}$$

From results presented in Figs. 5.16 to 5.21, the normal and shear stresses on any plane may be evaluated using the following relationships obtained from the Mohr's Circle:

$$\sigma_n = \frac{\sigma_1 + \sigma_2}{2} + \left(\frac{\sigma_1 - \sigma_2}{2}\right) \cos 2n \quad (5.4)$$

$$\tau_n = \left(\frac{\sigma_1 - \sigma_2}{2}\right) \sin 2n \quad (5.5)$$

where  $n$  is the angle made by the normal to the plane with the major principal stress direction. Equations (5.4) and (5.5) were used to find  $\sigma_x$  along the vertical sections at mid-span and at centre-line of each opening, and also  $\sigma_y$  along the horizontal section at mid-depth of each beam. Results were plotted as ratios to  $\sigma_s$  and presented in Figs. 5.22 to 5.27.

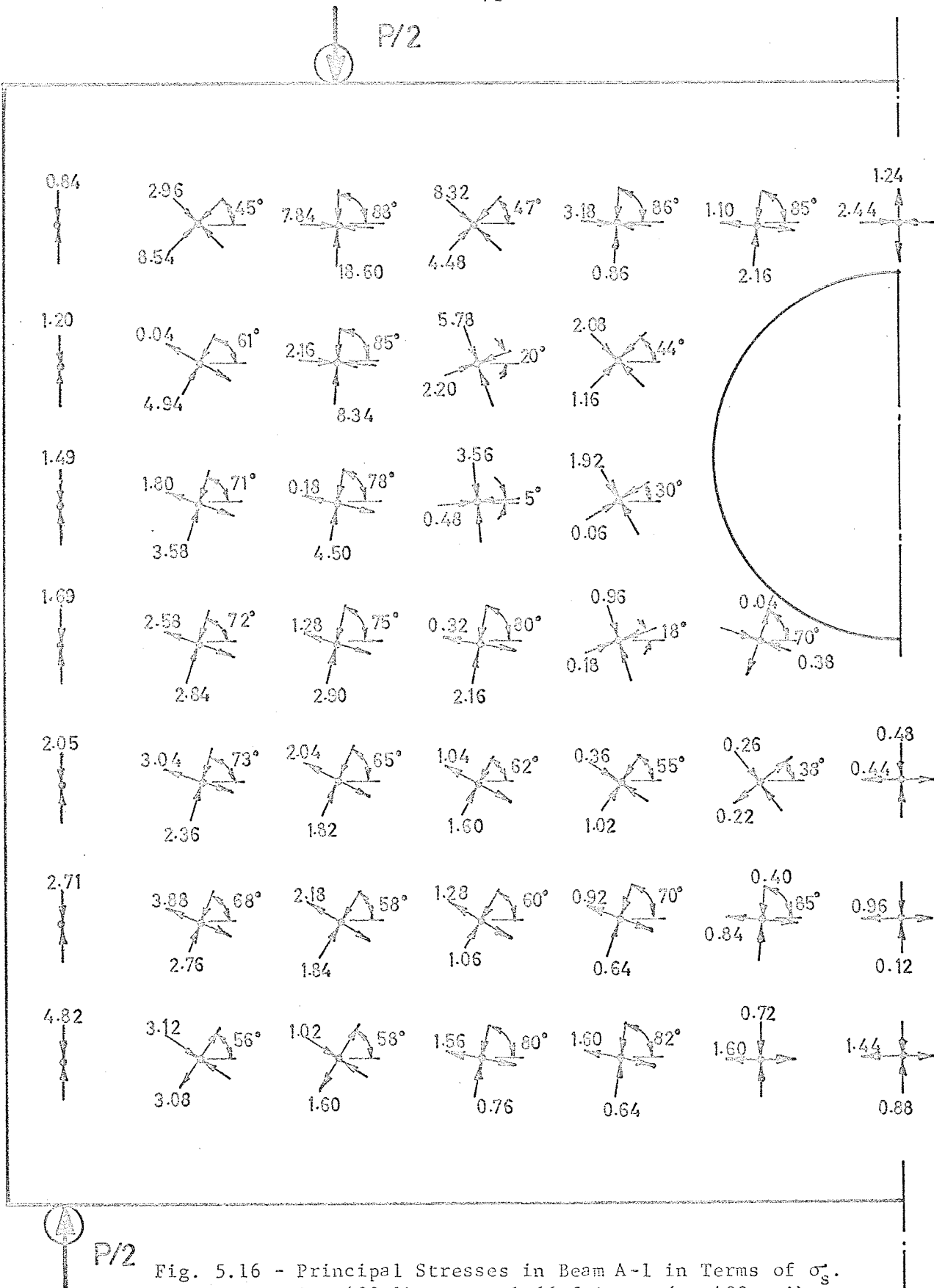


Fig. 5.16 - Principal Stresses in Beam A-1 in Terms of  $\sigma_s$ .  
 $P = 400$  lb;  $\sigma_s = 1.66$  fringes (or 400 psi)

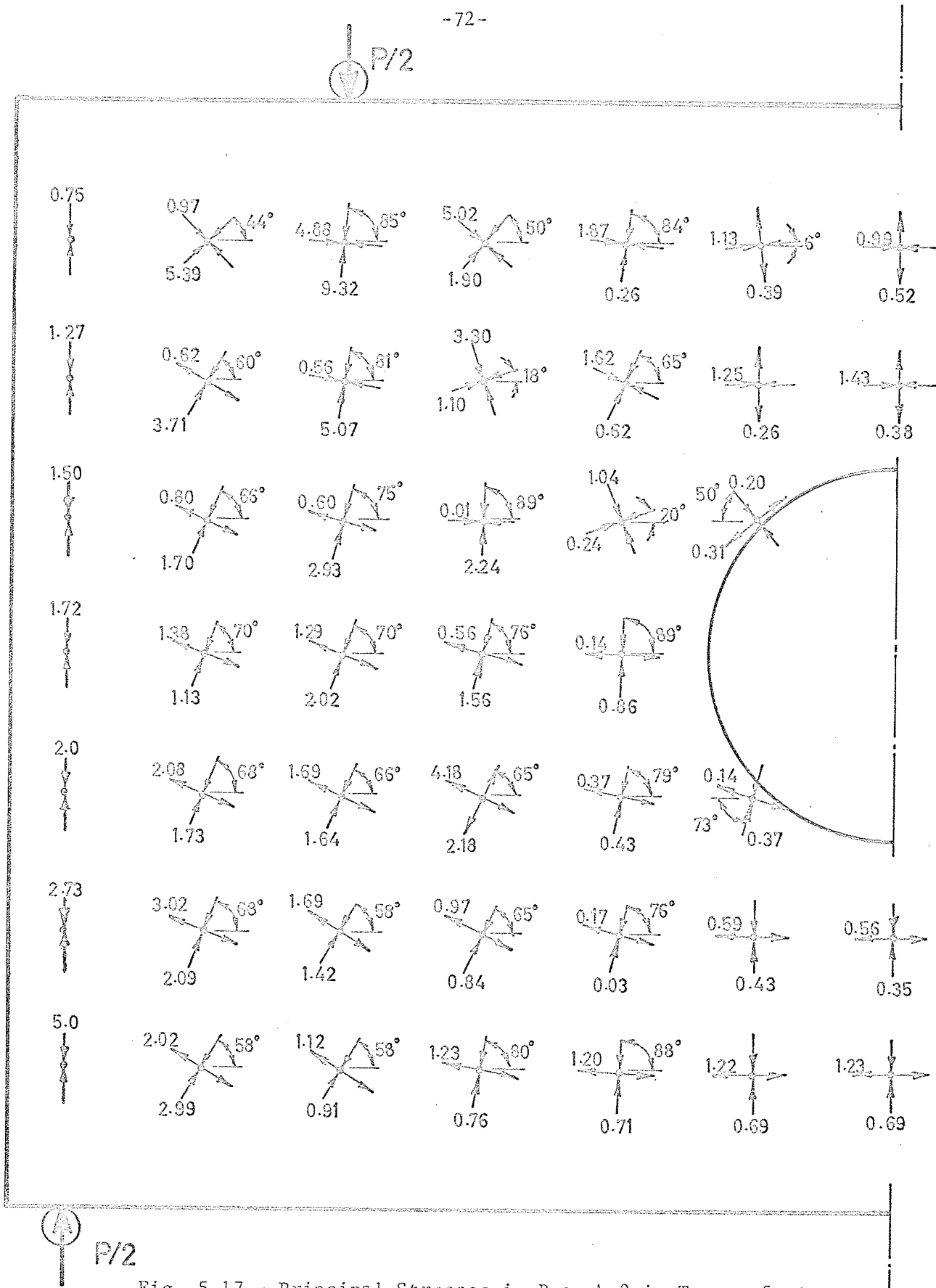


Fig. 5.17 - Principal Stresses in Beam A-2 in Terms of  $\sigma_s$ .  
 $P = 480 \text{ lb}$ ;  $\sigma_s = 2.0 \text{ fringes (or } 480 \text{ psi)}$

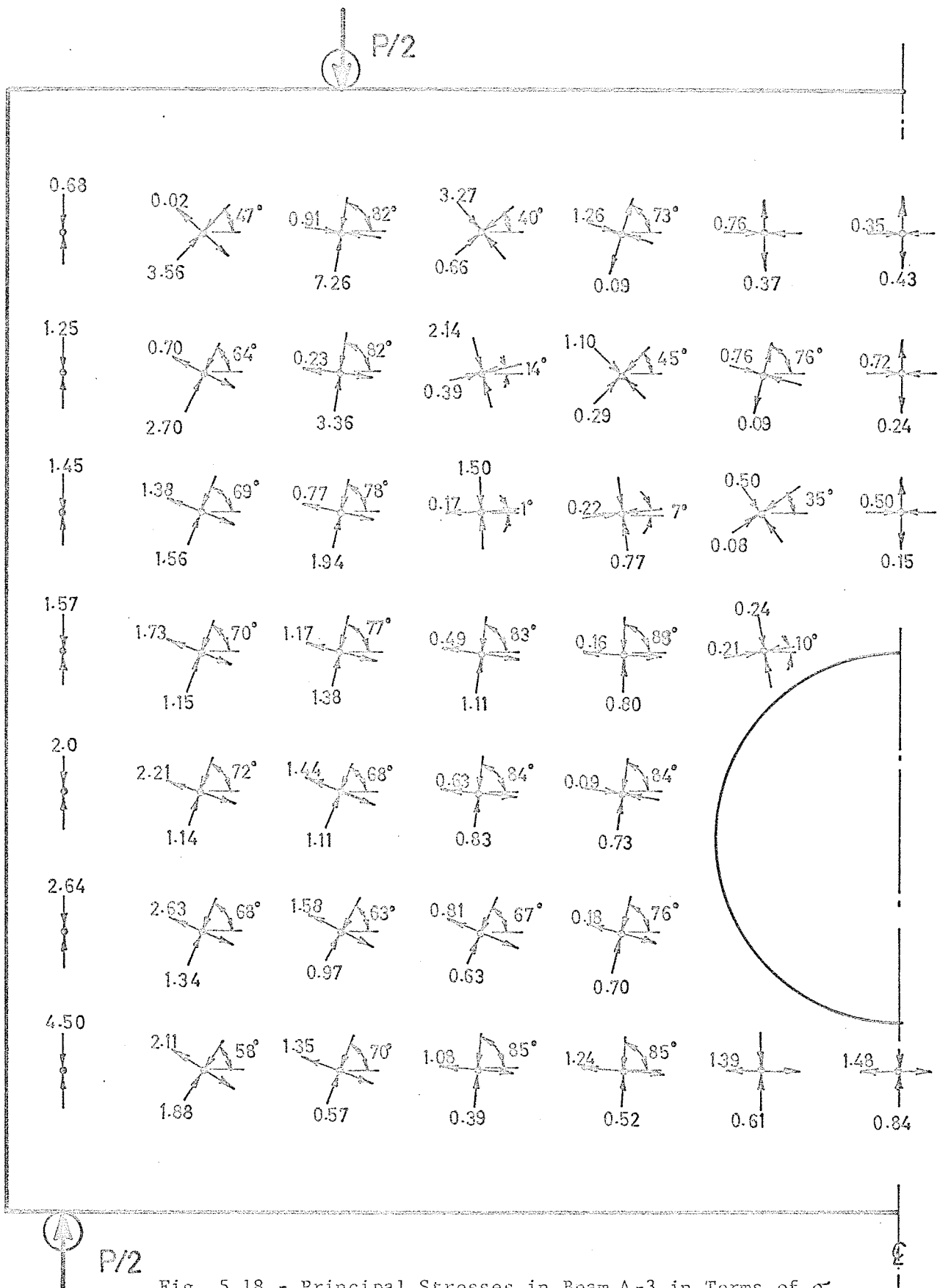


Fig. 5.18 - Principal Stresses in Beam A-3 in Terms of  $\sigma_s$ .  
 $P = 480$  lb;  $\sigma_s = 2.0$  fringes (or 480 psi)

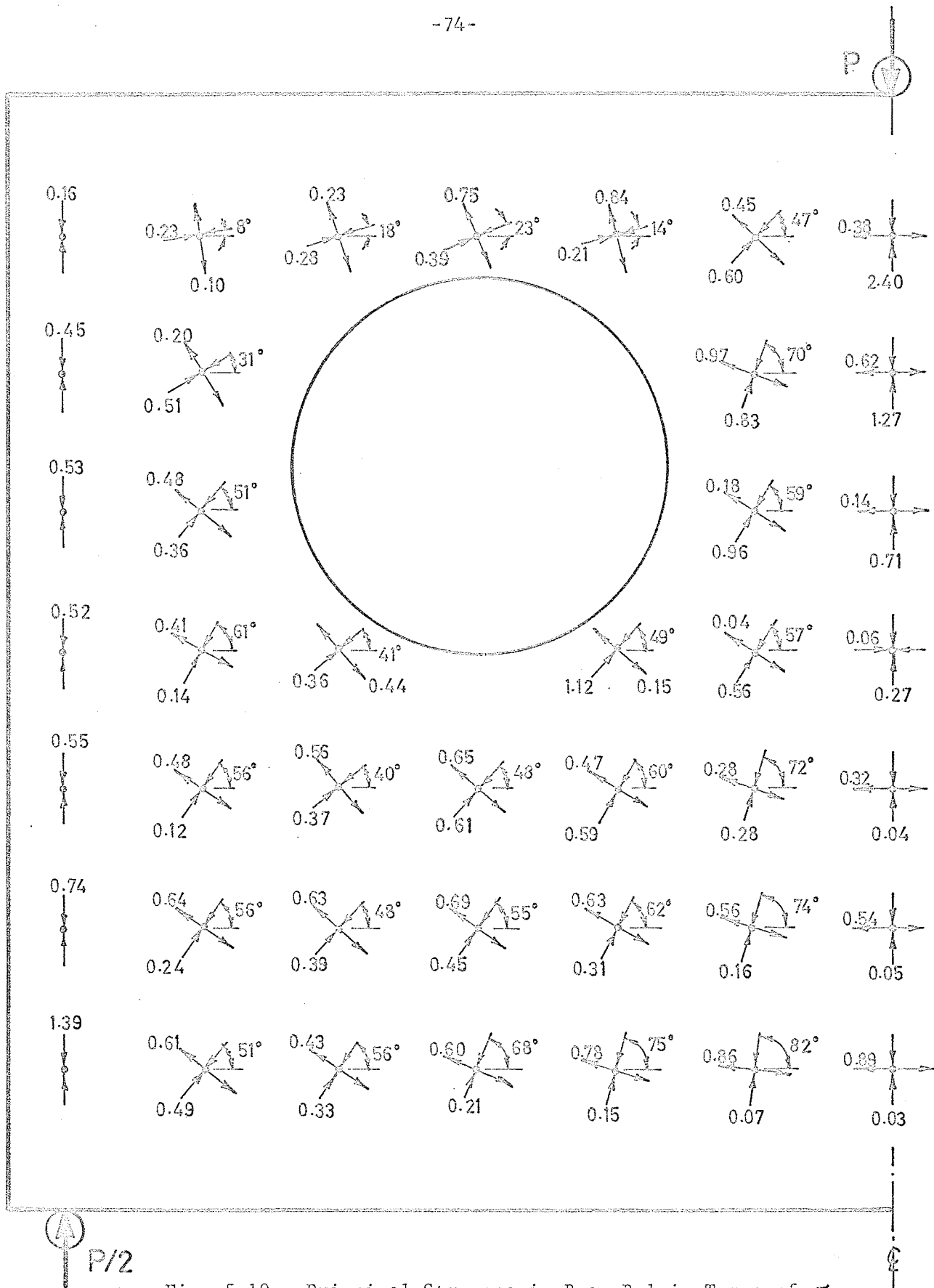


Fig. 5.19 - Principal Stresses in Beam B-1 in Terms of  $\sigma_s$ .  
 $P = 216 \text{ lb}$ ;  $\sigma_s = 2.69 \text{ fringes (or } 645 \text{ psi)}$

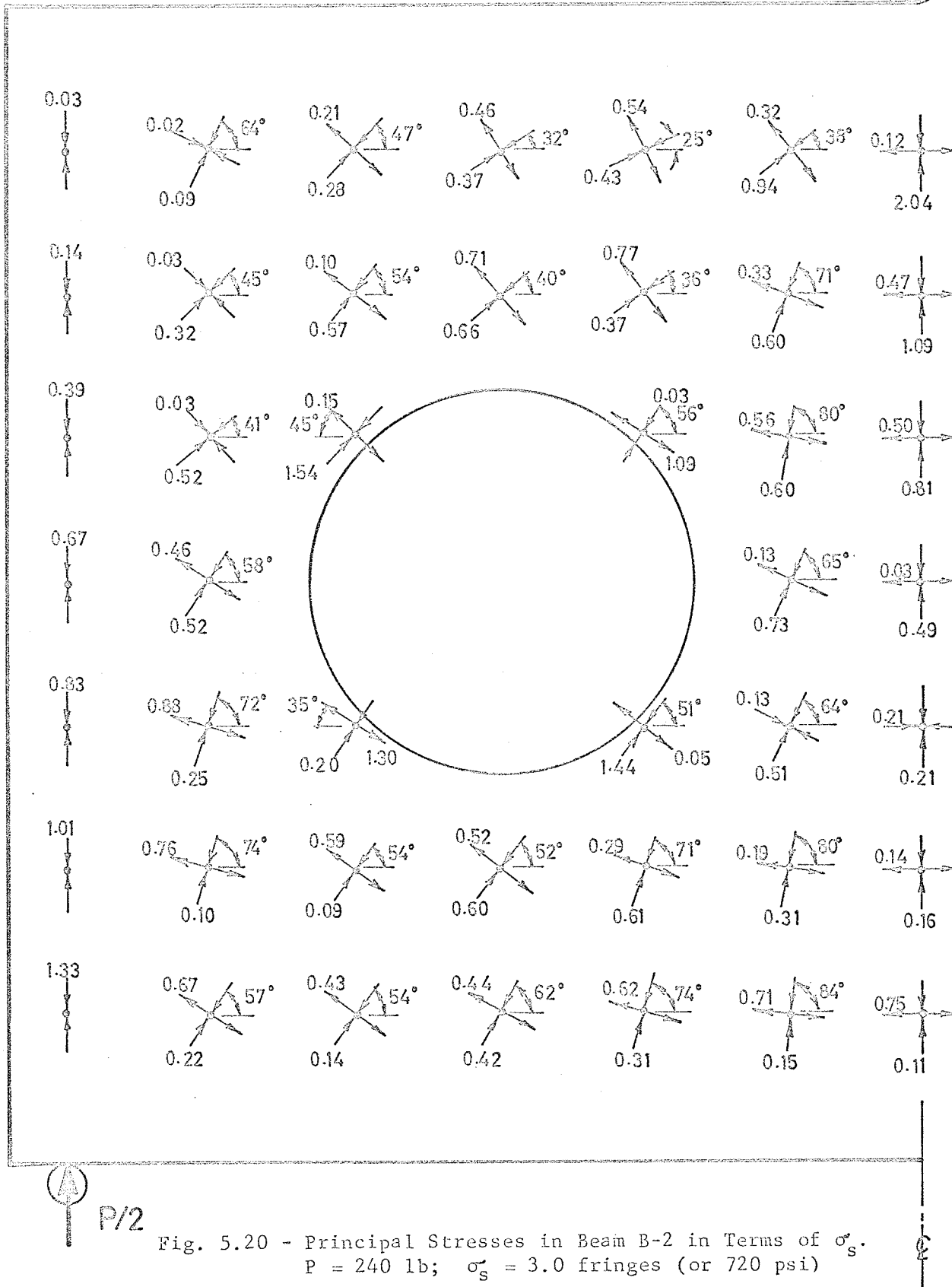
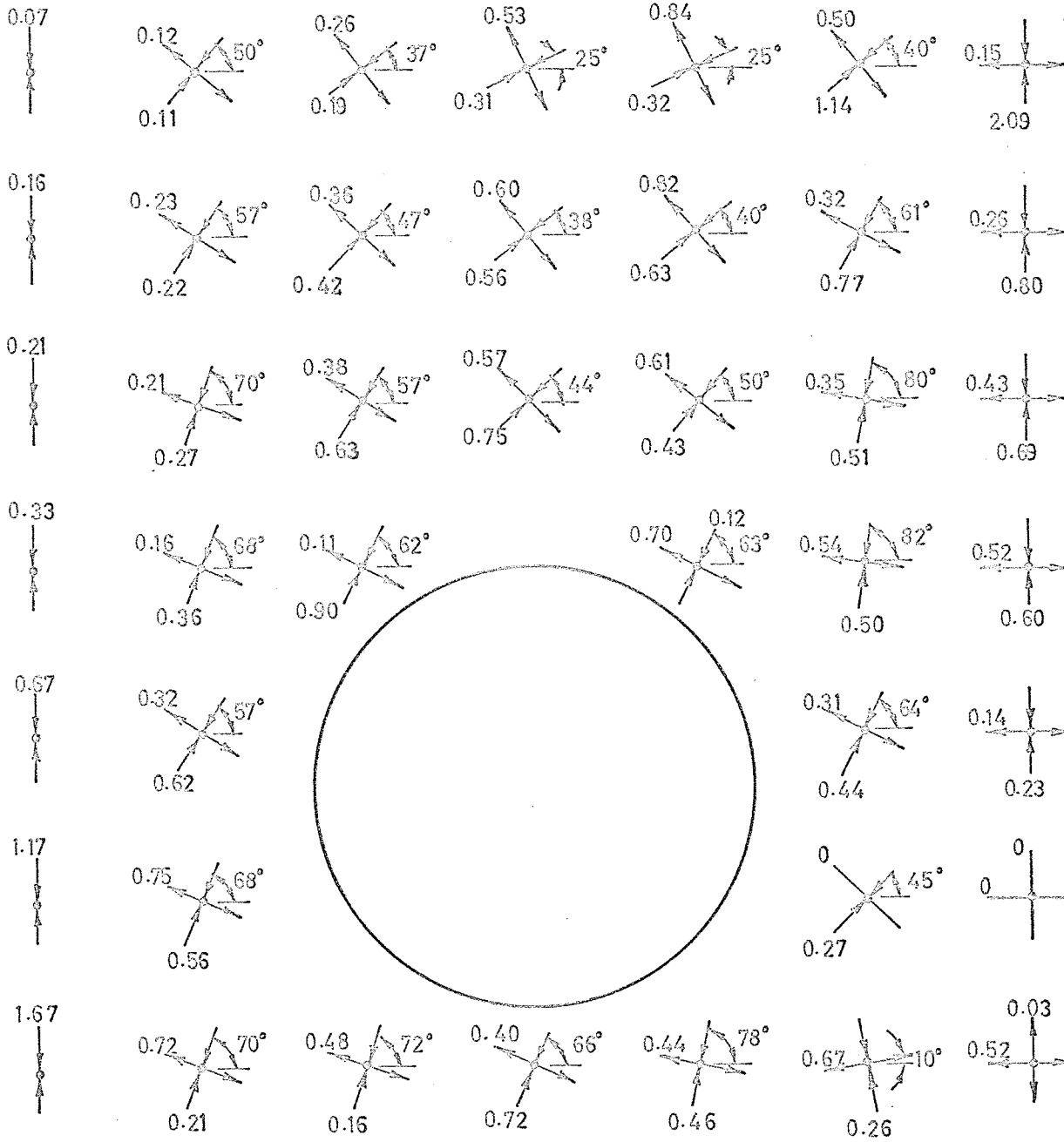


Fig. 5.20 - Principal Stresses in Beam B-2 in Terms of  $\sigma_s$ .  
P = 240 lb;  $\sigma_s = 3.0$  fringes (or 720 psi)



P/2

Fig. 5.21 - Principal Stresses in Beam B-3 in Terms of  $\sigma_s$ .  
P = 240 lb;  $\sigma_s = 3.0$  fringes (or 720 psi)



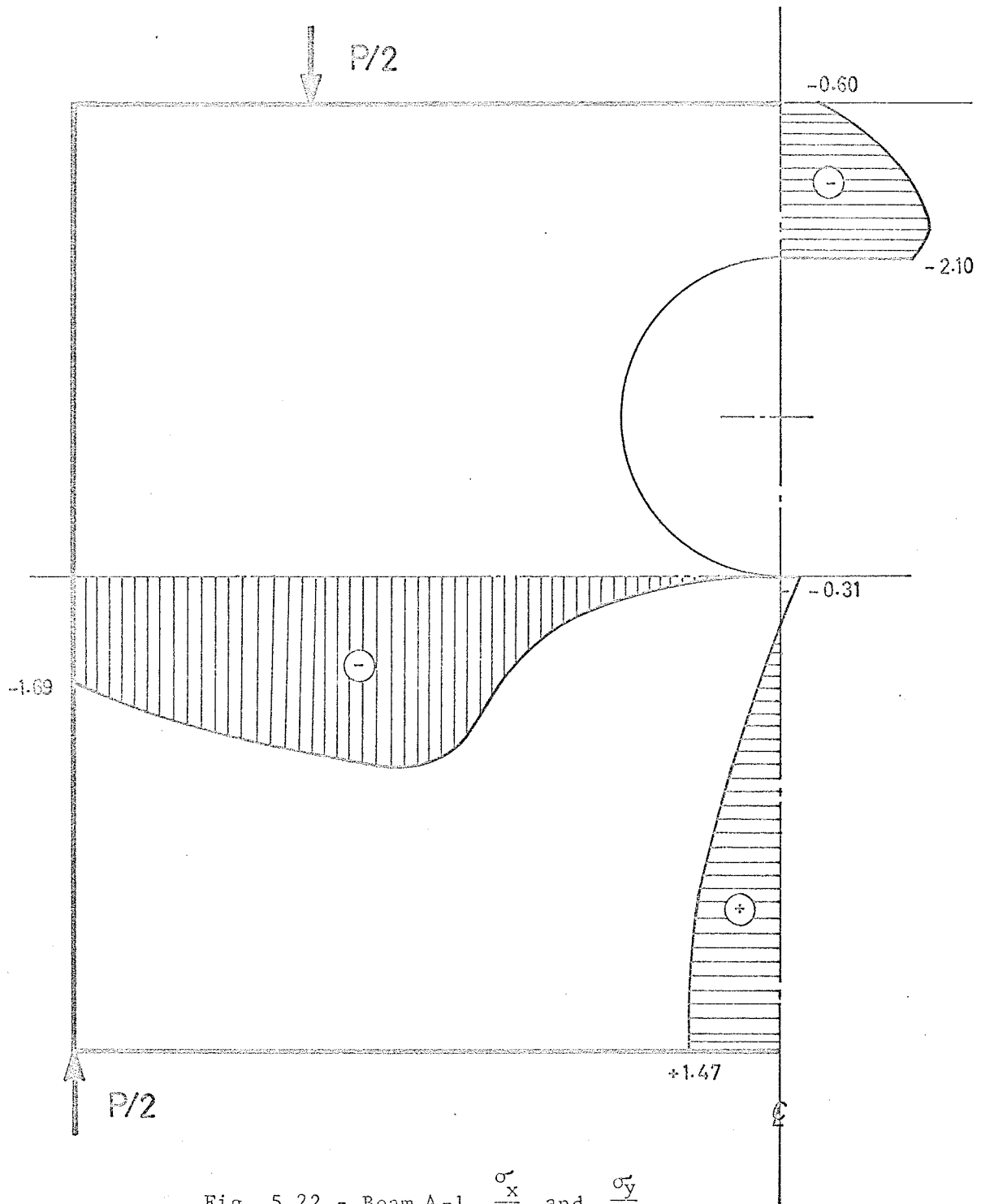


Fig. 5.22 - Beam A-1,  $\frac{V}{S}$  and  $\frac{M}{S}$ .

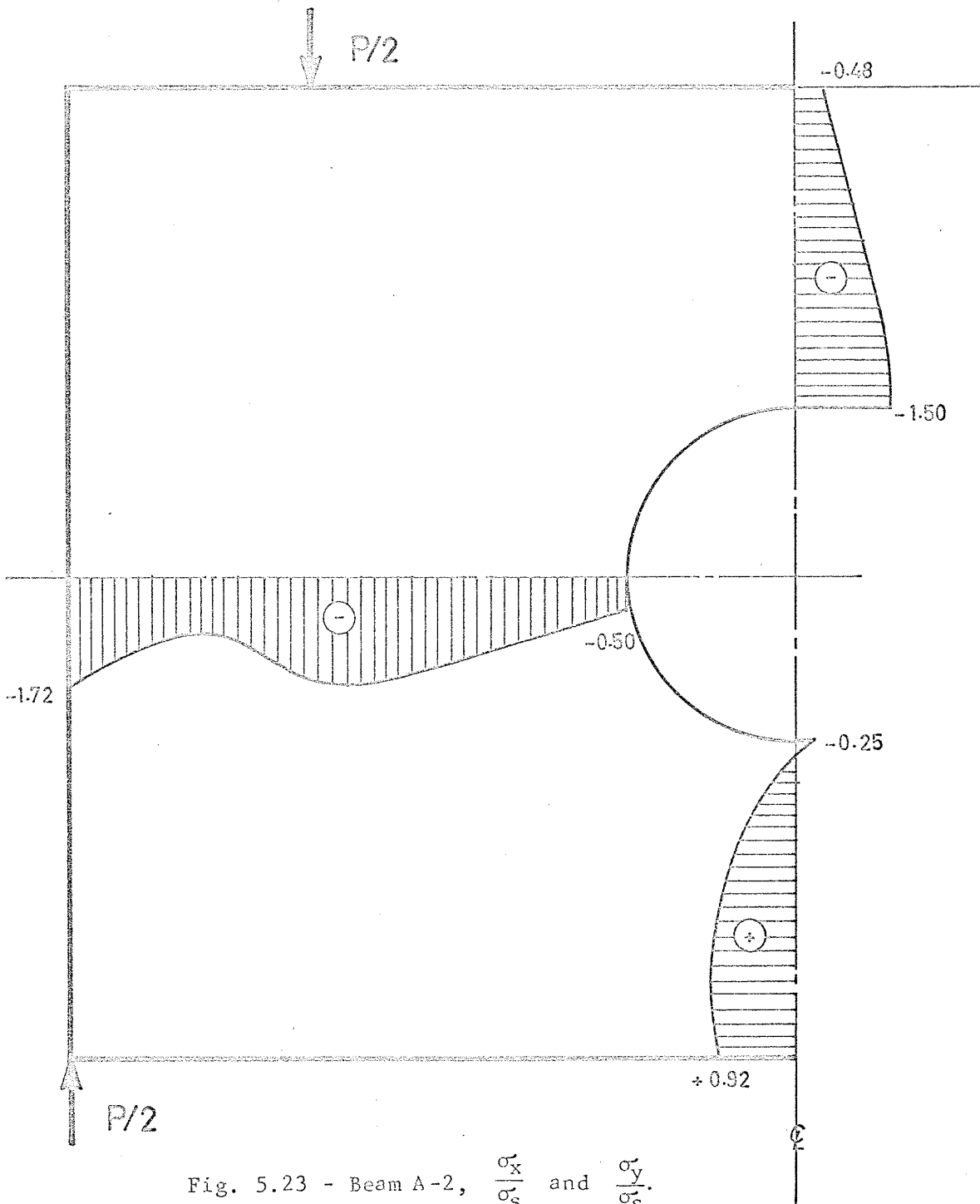


Fig. 5.23 - Beam A-2,  $\frac{\sigma_x}{\sigma_s}$  and  $\frac{\sigma_y}{\sigma_s}$ .

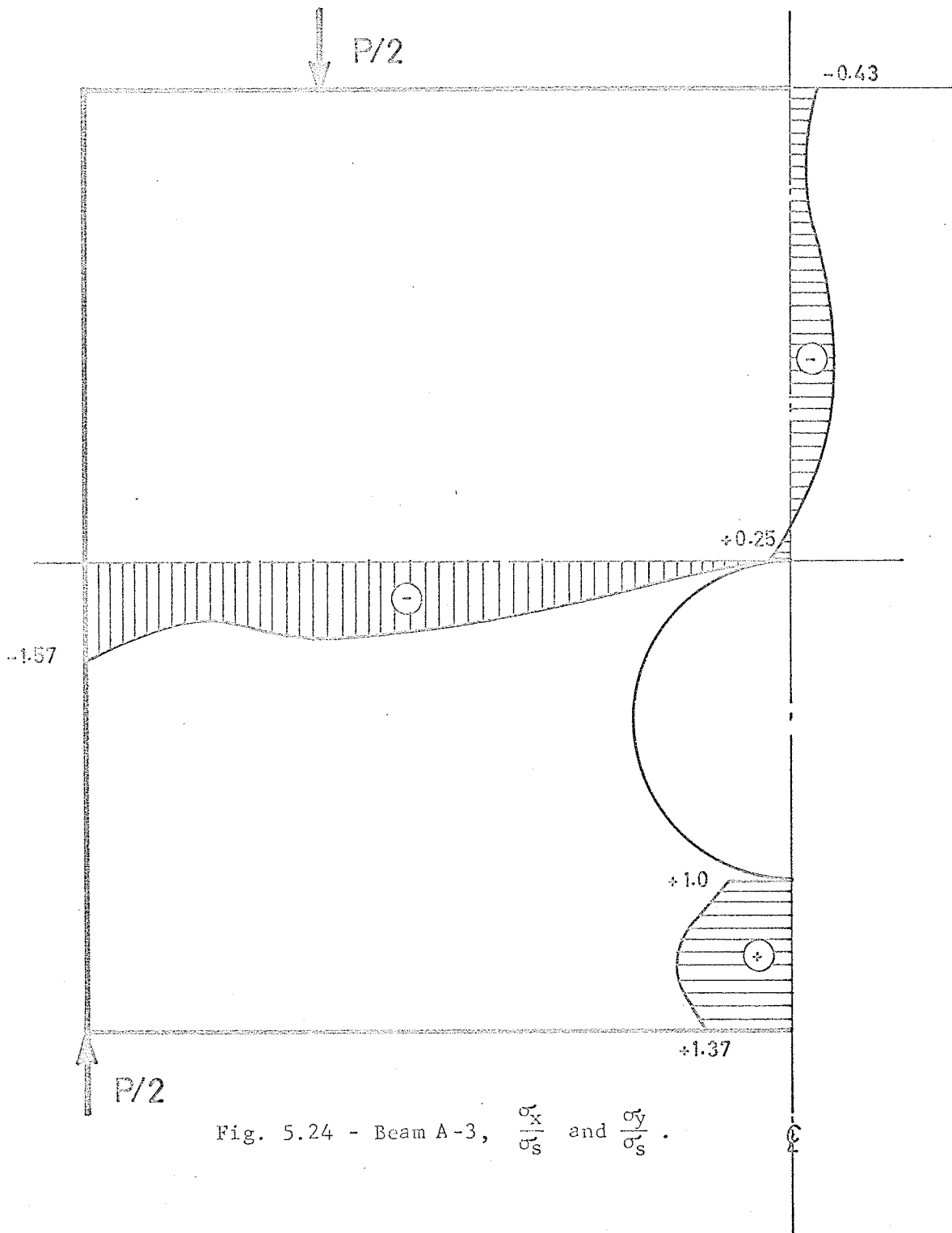


Fig. 5.24 - Beam A-3,  $\frac{\sigma_x}{\sigma_s}$  and  $\frac{\sigma_y}{\sigma_s}$ .

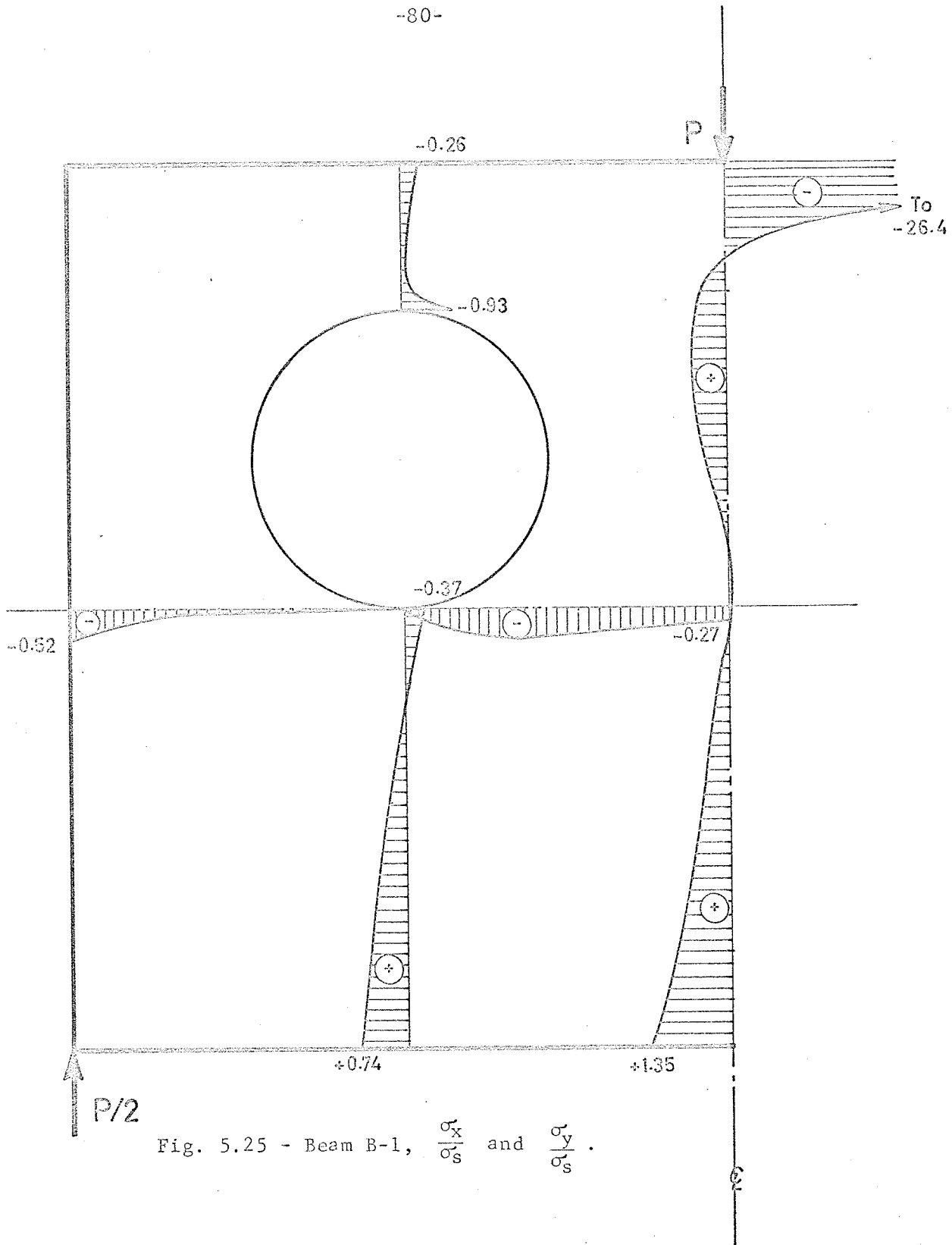


Fig. 5.25 - Beam B-1,  $\frac{\sigma_x}{\sigma_s}$  and  $\frac{\sigma_y}{\sigma_s}$ .

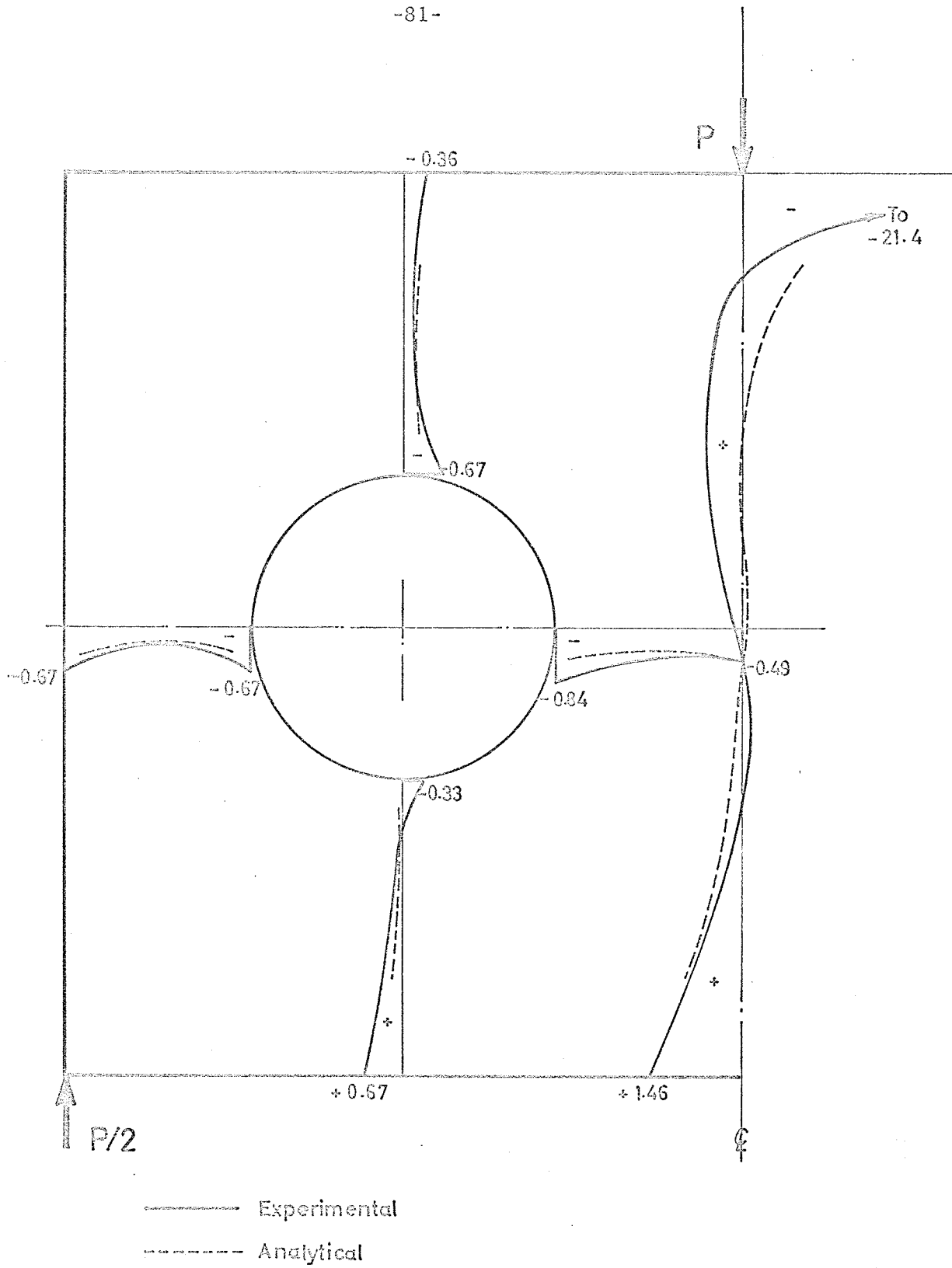


Fig. 5.26 - Beam B-2,  $\frac{\sigma'_x}{\sigma'_s}$  and  $\frac{\sigma'_y}{\sigma'_s}$ .

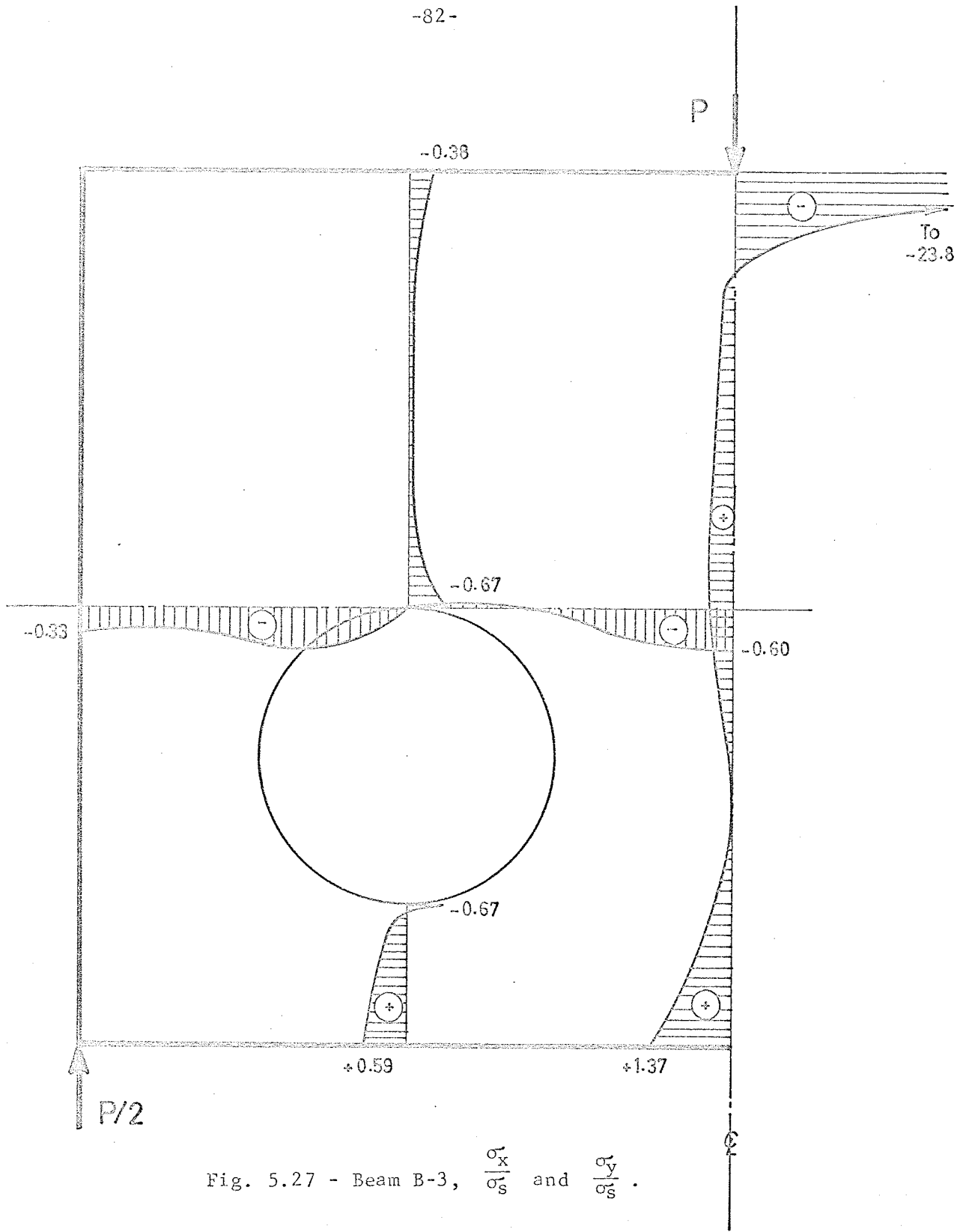
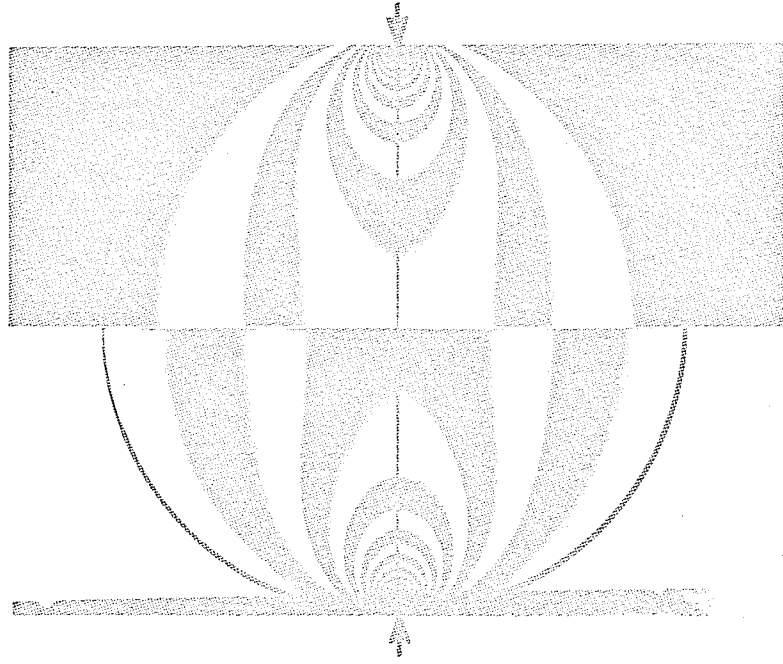
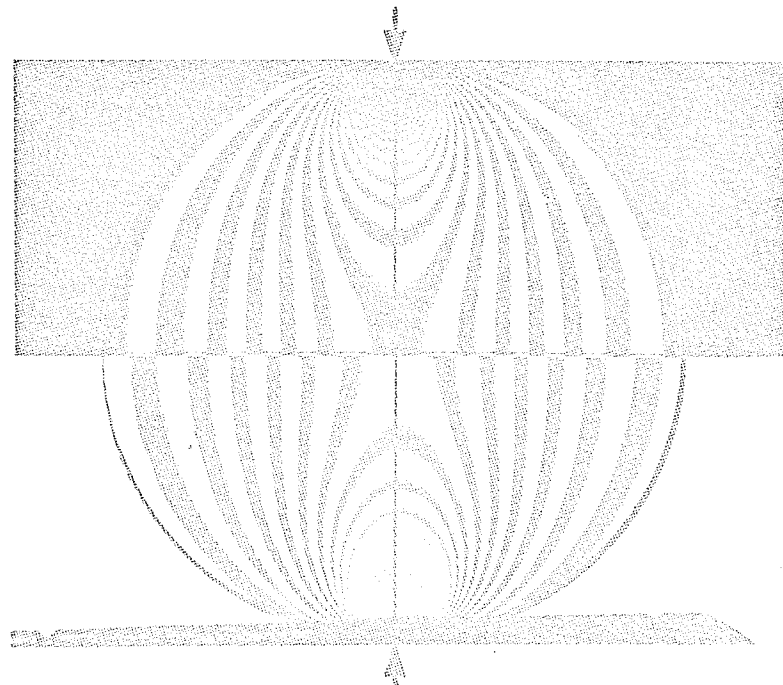


Fig. 5.27 - Beam B-3,  $\frac{\sigma_x}{\sigma_s}$  and  $\frac{\sigma_y}{\sigma_s}$ .



Matching Dark-Light Field Isochromatics in  
Circular Disk, Arbitrary Zero Load = 80 lb.

PLATE 1



Matching Dark-Light Field Isochromatics  
in Circular Disk, Final Load = 400 lb.

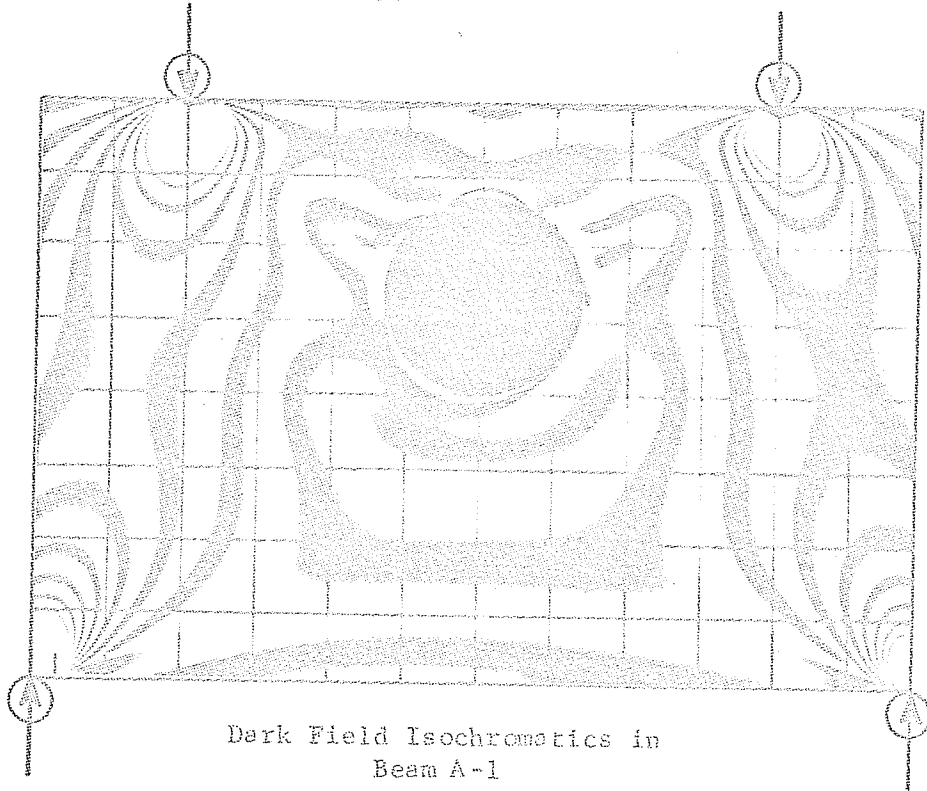
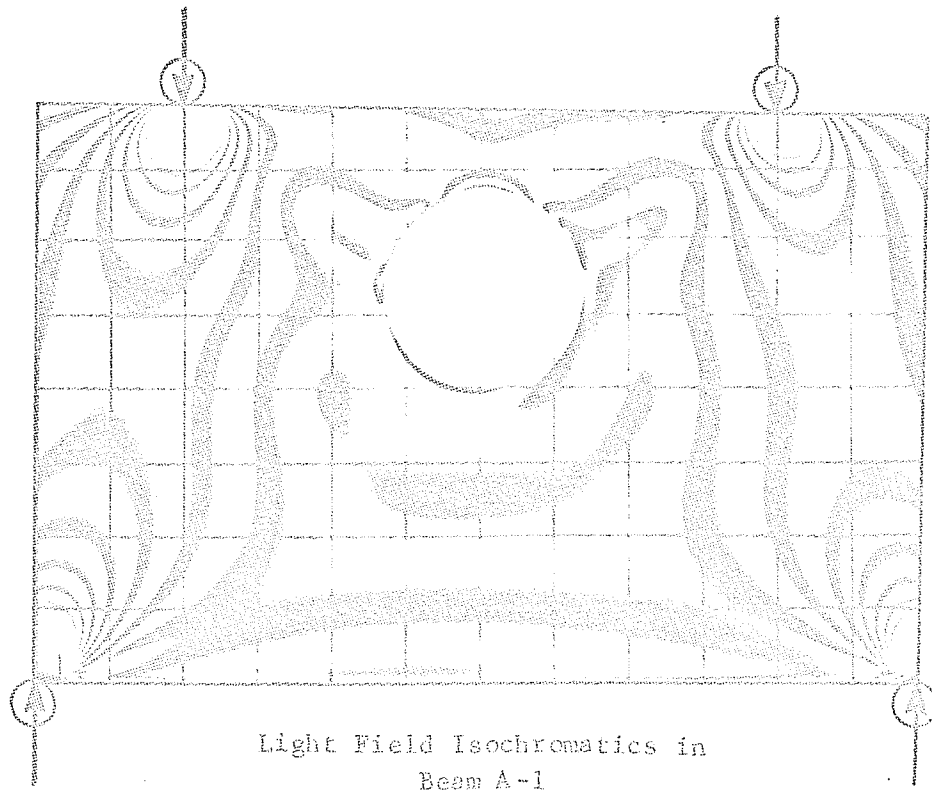
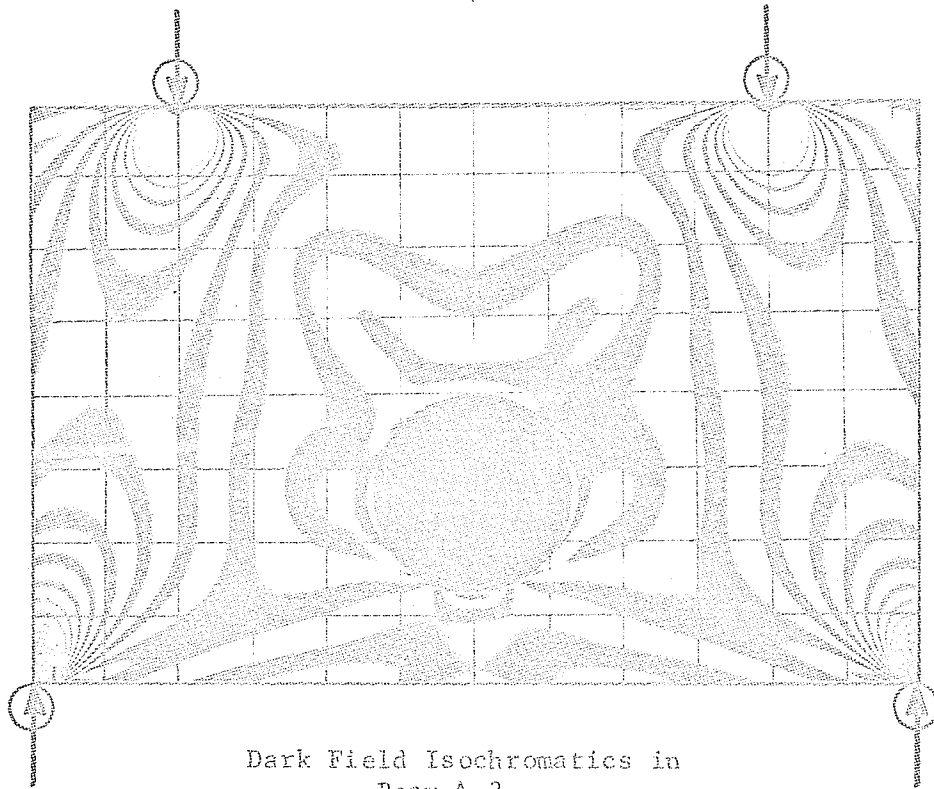


PLATE 2

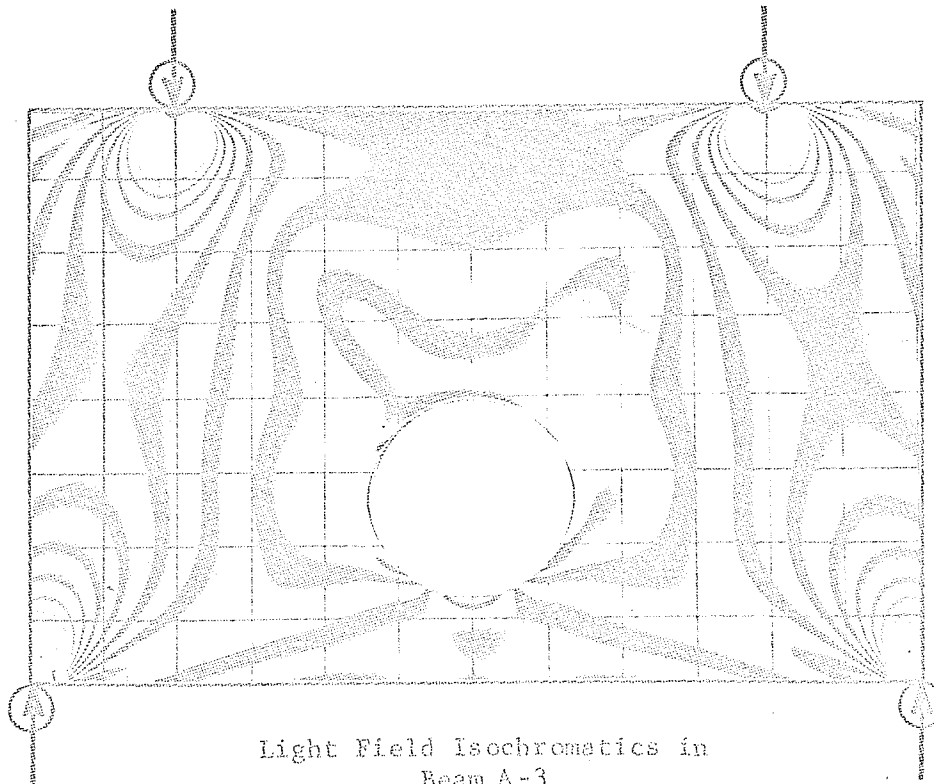






Dark Field Isochromatics in  
Beam A-3

PLATE 4

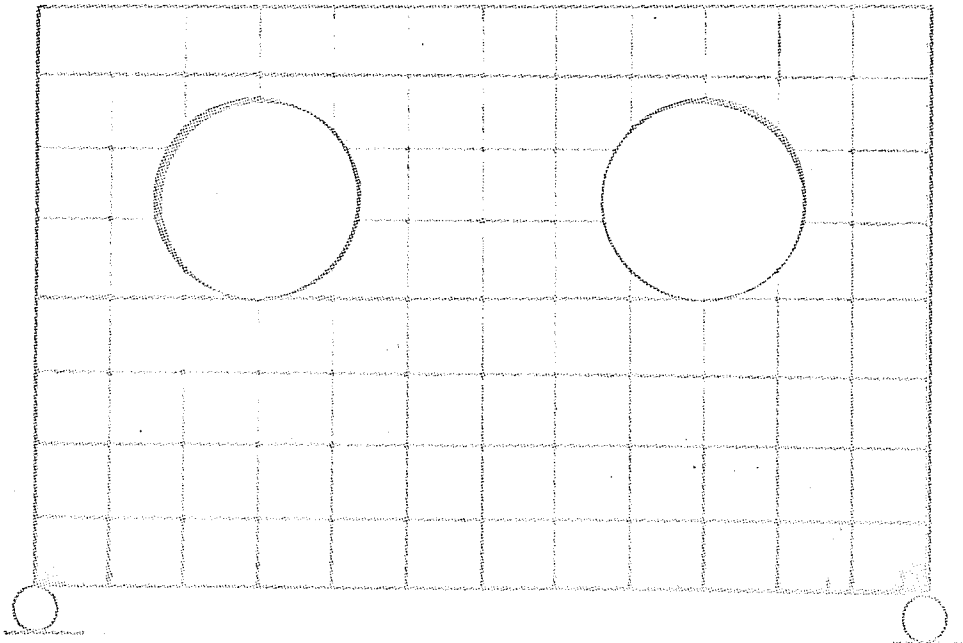


Light Field Isochromatics in  
Beam A-3

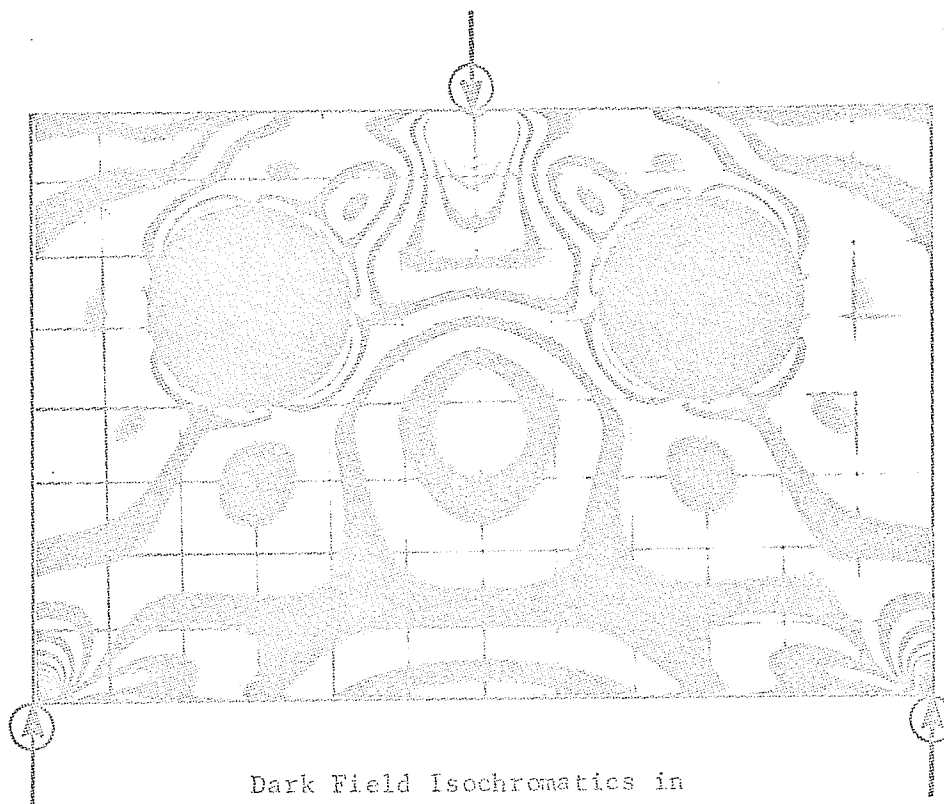


Model in Dark Field before Load Application

PLATE 5

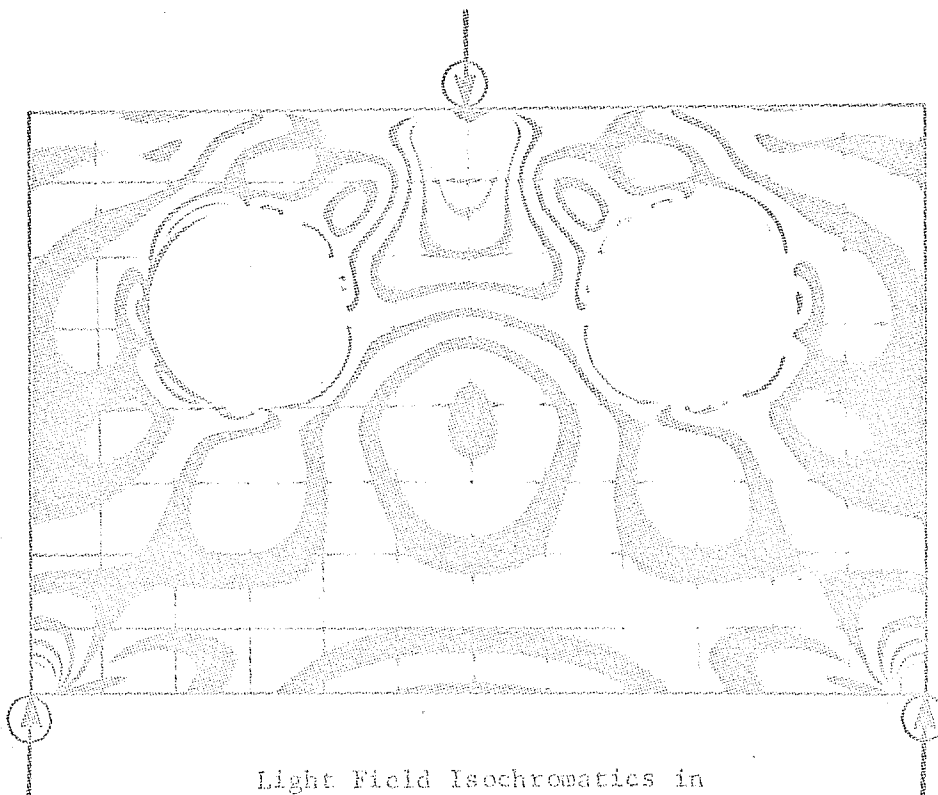


Model in Light Field before Load Application

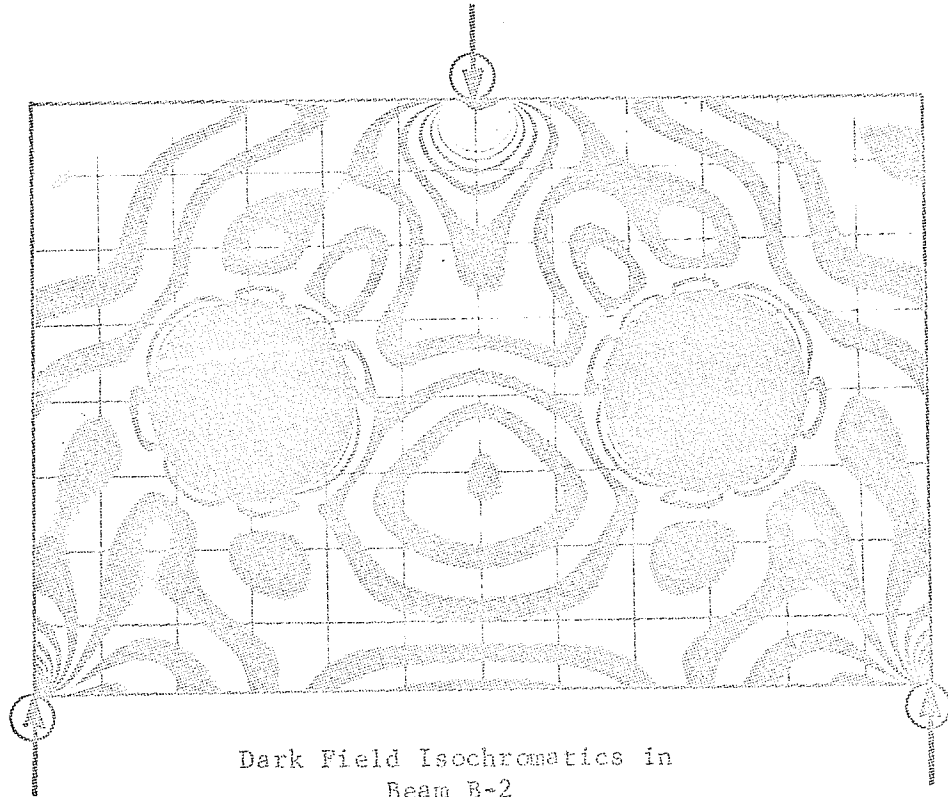


Dark Field Isochromatics in  
Beam B-1

PLATE 6

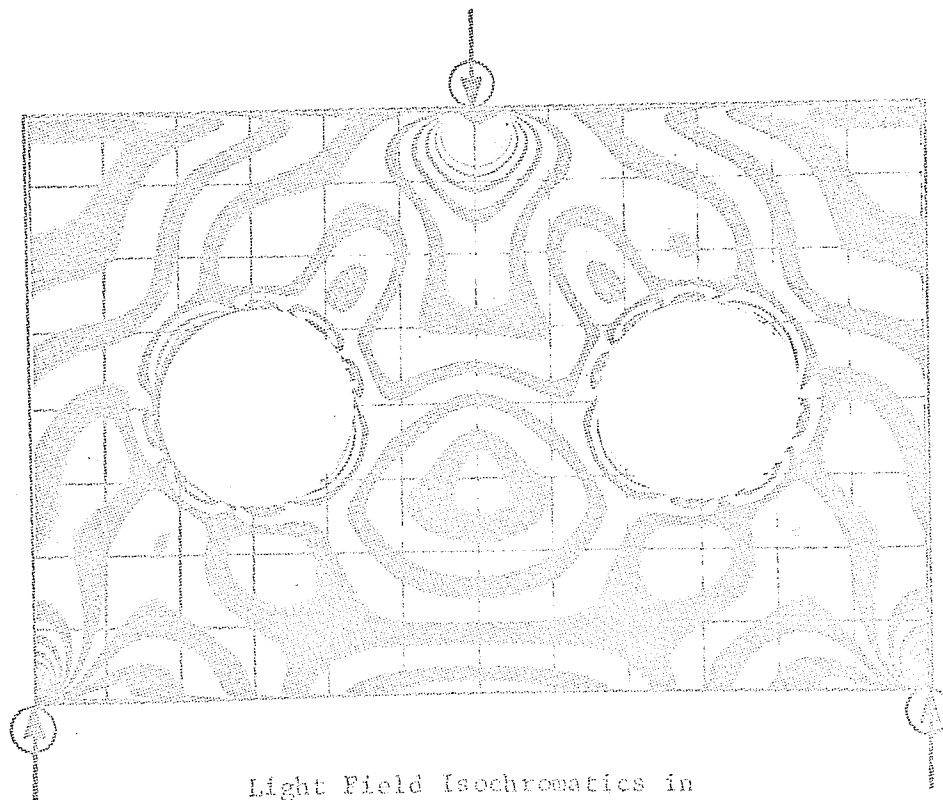


Light Field Isochromatics in  
Beam B-1

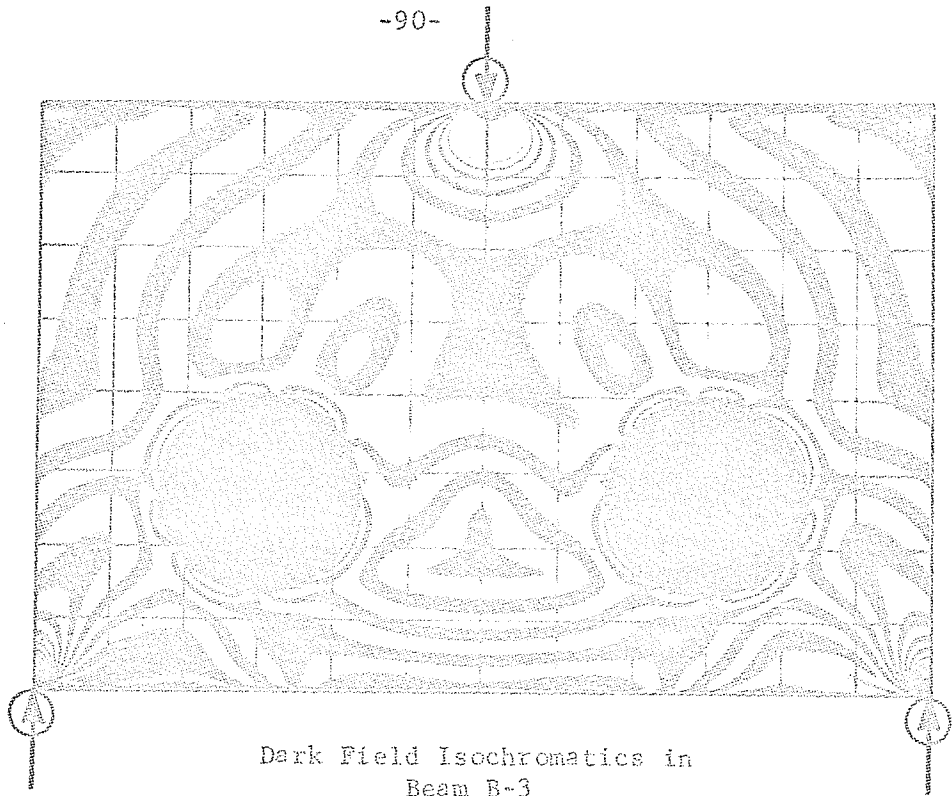


Dark Field Isochromatics in  
Beam B-2

PLATE 7

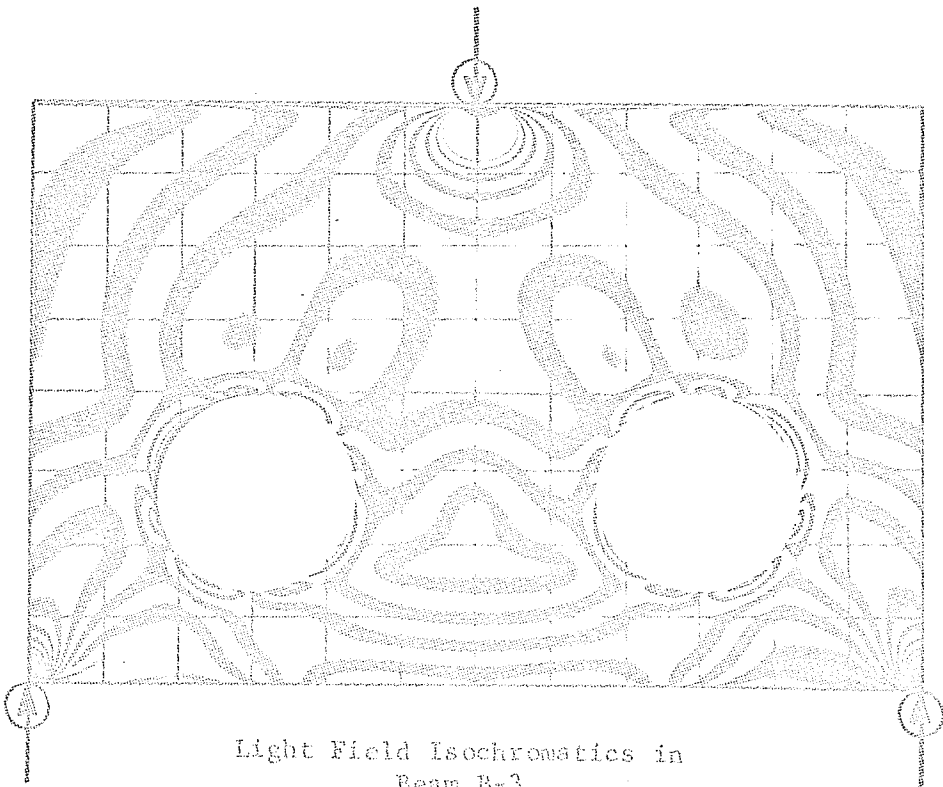


Light Field Isochromatics in  
Beam B-2

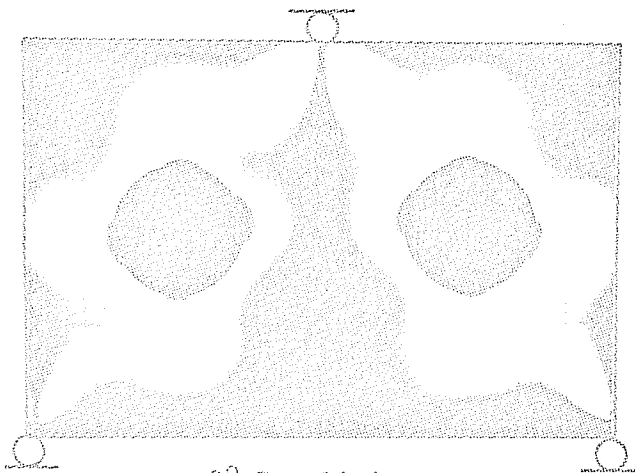


Dark Field Isochromatics in  
Beam B-3

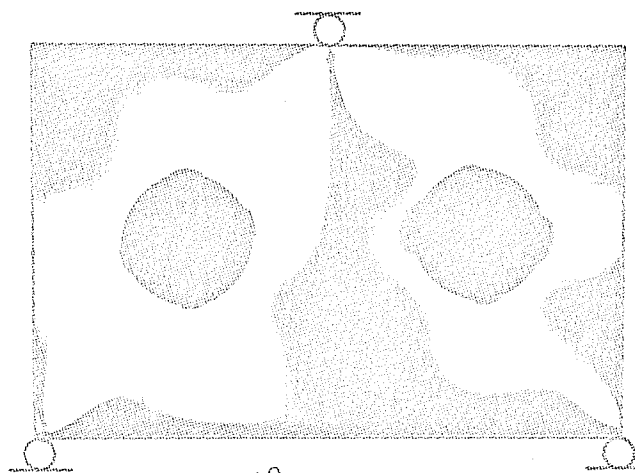
PLATE 8



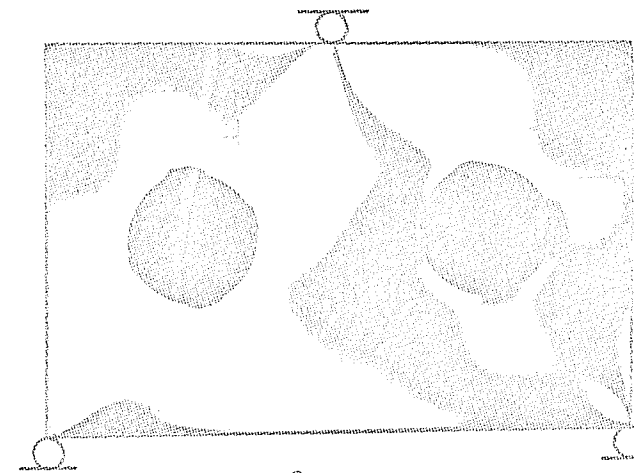
Light Field Isochromatics in  
Beam B-3



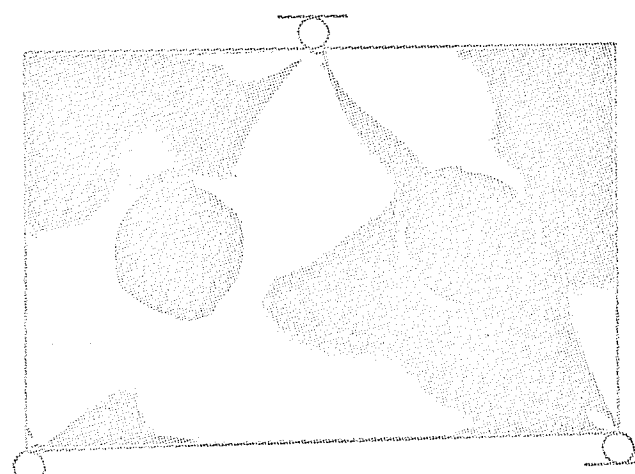
0° Isoclinics



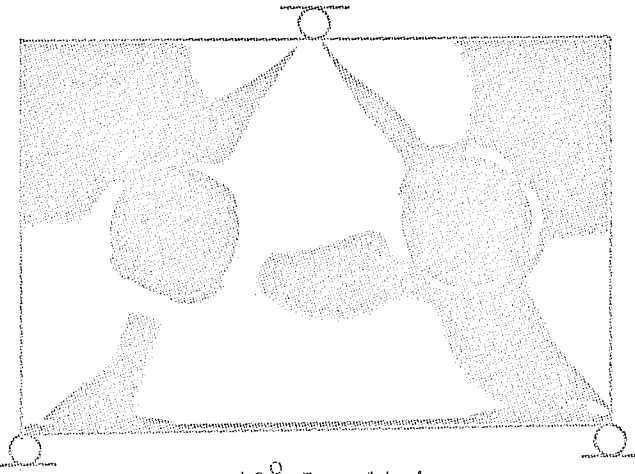
10° Isoclinics



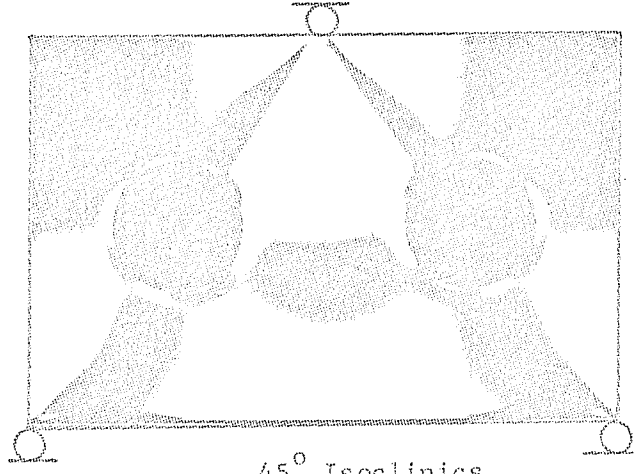
20° Isoclinics



30° Isoclinics

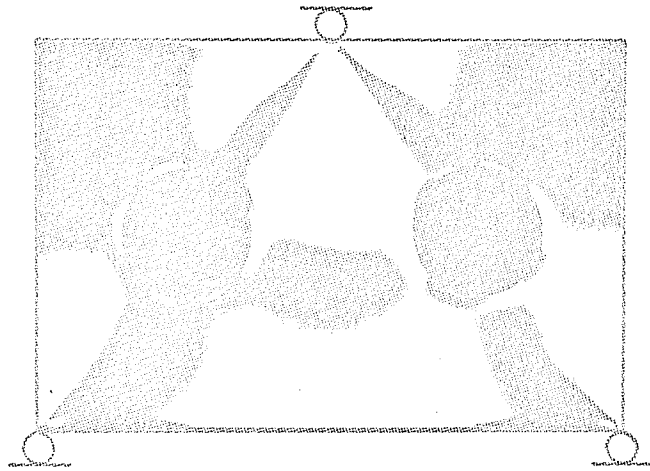


40° Isoclinics

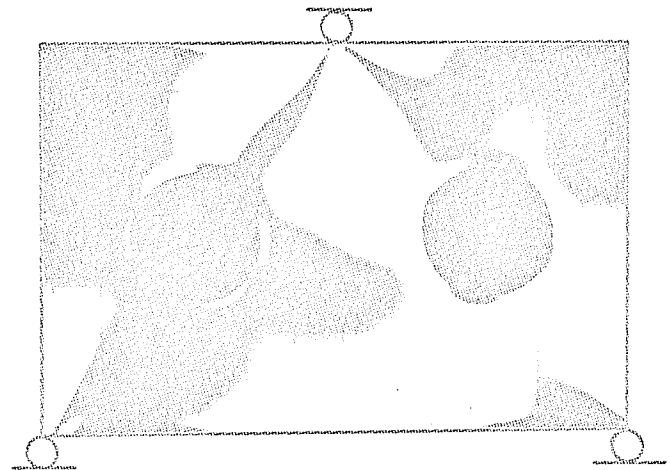


45° Isoclinics

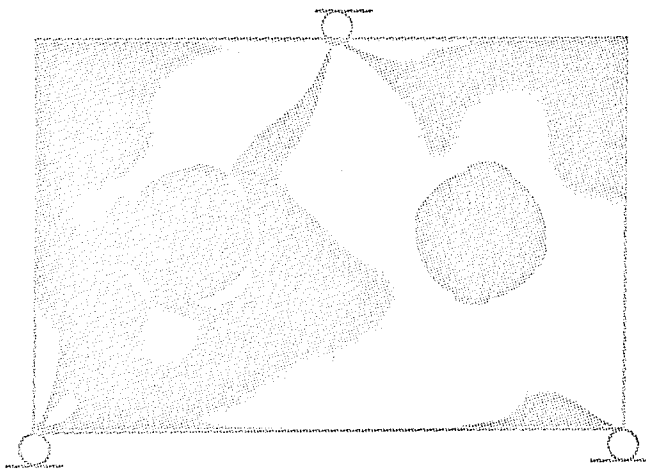
PLATE 9 - Isoclinics in Beam B-2



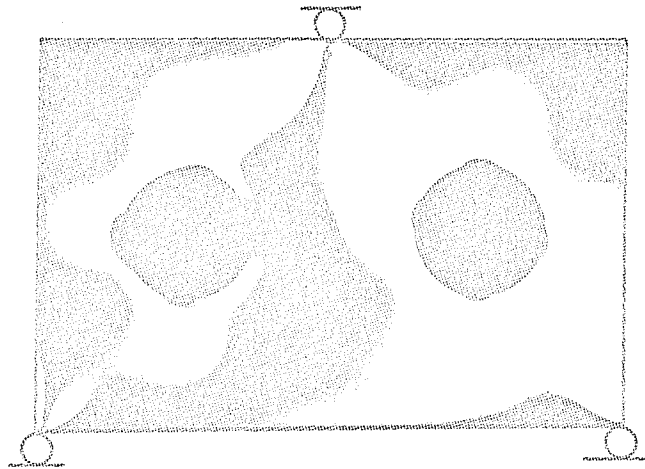
50° Isoclinics



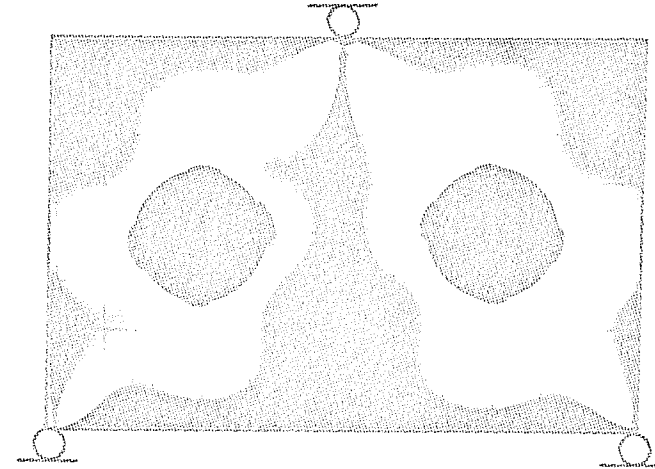
60° Isoclinics



70° Isoclinics



80° Isoclinics



90° Isoclinics

PLATE 10 - Isoclinics in Beam B-2 (Cont'd)

## 6. DISCUSSIONS

### 6.1 Observations on Experimental and Analytical Results

Stress distribution curves for all six beams investigated resemble those obtained by Saad and Hendry (14) and Weinberg (22) for similar beams but without openings, except for the regions in the immediate vicinity of the openings. Deviation is more pronounced when the hole is located in the lower half of the beam where tension predominates.

Stress distribution diagrams around openings in beams of series A (Figs. 5.10 to 5.12), which were subjected to pure bending, are symmetrical about the axis of symmetry of the beam. In cases of series B (Figs. 5.13 to 5.15), a line of symmetry is also found, for each beam, which is roughly parallel to the line joining the concentrated load and the support. Stress concentration is not very serious in any of the cases considered, indicating that circular shapes are desirable when openings have to be made.

Analytical and experimental results obtained for beam B-2 compare very favorably (Fig. 5.26). The discrepancy directly under the point load may have been caused by two factors:

- (1) the assumption made in the analytical solution (Article 4.1) that the concentrated load is distributed over a small area, and
- (2) sensitivity of the value  $C$ , the constant in the linear combination used in the experimental analysis (Article 5.5), to concentrated loads.

The fact that an extremely good comparison is obtained elsewhere in the beam, despite the above two factors, is a good verification of Saint-Venant's Principle.

## 6.2 Application of Experimental Results to Prototypes

Model analysis<sup>(8)</sup> shows that results obtained in photoelastic studies, when multiplied by a proper scale factor, may be applied to prototypes made of any homogeneous material loaded within its elastic limit. The only possible source of error, the difference in model and prototype Poisson's ratios, need not be considered when the body is simply-connected and the body-force field is either absent or uniform (i.e. dead weight loading). For multiply-connected bodies, Coke and Filon<sup>(2)</sup> have indicated a dislocation procedure which may be followed in making correction to the stress distribution produced by a different Poisson's ratio. In most practical cases, however, Wolf<sup>(23)</sup> claims that this correction only ranges from 5 to 8 percent.

In the case of reinforced concrete members, non-homogeneity of the material and cracking of the tension zone may result in a stress distribution somewhat different from that predicted in the model study. If, however, tension steel is arranged in such a fashion as to give a distribution of steel stresses which closely resembles that in the tension zone of the model, resultant of the steel stresses would be located very close to, if not coincident with, that found in the model. Besides, deep beams are generally imbedded with a mesh reinforcement which further enhances homogeneity by reducing the chances of small cracks propagating. For members similar to the models studied, and under similar conditions of loading, it is recommended that the same amount of steel be specified around the openings as at the bottom of the tension zone, because the maximum value of  $\sigma_{\theta}/\sigma_m$  is very close to unity in all cases, where  $\sigma_m$  has been previously defined as the maximum stress at the extreme bottom

fibre of the beam.

### 6.3 Conclusions

Both the experimental and the analytical methods used in this investigation have been found to be very efficient and produce rigorous results, the photoelastic method being particularly useful in determining stress concentrations. Only a limited number of parameters in the problem of deep beams with openings have been studied, but the same methods may be applied to a more extensive range of depth/span ratios, diameter/depth ratios and locations of openings so that charts may be prepared to aid practical design.

Normally, as in the case of other experimental methods, photoelasticity enters the pictures when a mathematical analysis proves inadequate or unsatisfactory. However, even when analytical solutions are obtainable by numerical methods, photoelasticity is still invaluable in providing convincing corroboration in theoretical methods, thus adding much to its technical value. It is to this end that photoelasticity has been employed in this research.

The new flexibility coefficient method developed by the author and his advisor <sup>(19)</sup> has proved to be a powerful method for the solution of plane stress problems of multiply-connected continua. The method promises to be extremely versatile and can be further developed for the solution of more involved problems in theory of plate and shell. The basic procedure as presented in Chapter 3 would essentially be unchanged, and only the details of the steps required to set up the flexibility coefficients matrix would have to be modified.

The author is of the hope that this theoretical and experimental study of stresses in wall-beams with openings will pave the way for further work in the subject. Future researchers might consider the following variations of the basic problem:

- (1) Effect of shape of openings on the stress concentration factors --- triangular, rectangular or elliptical, as compared to circular.
- (2) Effect of openings on stresses distributions in continuous wall-beams.
- (3) Stresses in deep beams with reinforced openings.
- (4) Cantilevered wall-beams with openings, loaded in bending and shear --- to simulate and study stresses in shear walls.

BIBLIOGRAPHY

BIBLIOGRAPHY

1. Chow, L., Conway, H. D. and Winter, G., "Stresses in Deep Beams", Proceedings of ASCE, Structural Division, Separate No. 127, Vol. 78, May, 1952.
2. Coker, E. G. and Filon, L. N. G., A Treatise on Photo-Elasticity, Cambridge University Press, 1931.
3. Conway, H. D., Chow, L. and Morgan, G. W., "Analysis of Deep Beams", Journal of Applied Mechanics, June, 1951, pp. 163-172.
4. Dally, J. W. and Riley, W. F., Experimental Stress Analysis, McGraw-Hill Book Co., 1965.
5. "Design of Deep Girders", Concrete Information No. ST66, Portland Cement Association, Chicago.
6. Dischinger, F., "Beitrag zur Theorie der Halscheib und wandertigen Balkens", Publications, International Association for Bridge and Structural Engineering, I, 1932, pp. 69-93.
7. Dlugach, M. I., Metok Setok v Smeshannoi Ploskoi Zadache Teorii Uprugosti (The Grid Method in Mixed Plane Elastic Problems), Naukova, Kiev, 1964.
8. Durelli, A. J. and Riley, W. F., Introduction to Photomechanics, Prentice-Hall, Inc., 1965.
9. Fan, B. and Shah, A. A., "A Study of Stress Distribution in a Deep Beam with a Central Circular Opening by Photoelastic Analysis", Unpublished Research Report, University of Manitoba, Winnipeg, 1968.
10. Frocht, M. M., Photoelasticity, Vol. II, John Wiley & Sons, New York, 1948, p.20.
11. Gaonkar, G. H., "Plane Stress Fields due to Isolated and Multirows of Inclusions in an Elastic Continuum", Doctoral Dissertation, Washington University, St. Louis, 1967.
12. Gibson, J. E. and Jenkins, W. M., "The Stress Distribution in a Simply-Supported Beam with a Circular Hole", The Structural Engineer, December, 1956, pp. 443-449.
13. Muskhelishvili, N. I., Some Basic Problems of the Mathematical Theory of Elasticity, P. Noordhoff Ltd., Groningen, the Netherlands, 1963.

14. Saad, S. and Hendry, A. W., "Stresses in a Deep Beam with a Central Concentrated Load", Experimental Mechanics, June, 1961, pp. 192-198.
15. Saad, S. and Hendry, A. W., "Gravitational Stresses in Deep Beams", The Structural Engineer, June, 1961, pp. 185-194.
16. Salvadori, M. G. and Baron, M. L., Numerical Methods in Engineering, Prentice-Hall, Ltd., 1963.
17. Savin, G. N., Stress Concentration Around Holes, English Translation by Johnson, W. (ed.), Pergamon Press, 1961.
18. Thadani, B. N., Modern Methods in Structural Mechanics, Asia Publishing House, 1964.
19. Thadani, B. N. and Fan, B., "A Flexibility Coefficient Method in Plane Stress Analysis", Paper Submitted for Publication, Journal of EIC, 1968.
20. Timoshenko, S. and Goodier, J. N., Theory of Elasticity, McGraw-Hill Book Co., 1951.
21. Wang, C. T., Applied Elasticity, McGraw-Hill, New York, 1953.
22. Weinberg, D. V. and Weinberg, E. D., Plastinki, Diski, Balki-Stenki (Plates, Disks, Wall-Beams), Gosstroizdat, Kiev, 1959.
23. Wolf, H., Spannungsoptik, Springer-Verlag, Berlin/Gothingen/Heidelberg, 1961.
24. Zienkiewicz, O. C. and Cheung, C. K., The Finite Element Method in Structural and Continuum Mechanics, McGraw-Hill Publishing Co., Ltd., 1967.
25. Zienkiewicz, O. C. and Holister, G. S., Stress Analysis, John Wiley & Sons, Ltd., 1965.

APPENDICES

APPENDIX A

EVALUATION OF MOHR'S INTEGRALS

A.1 Rectangular Elements --- Direct Stress Terms

The expressions of equation (3.7), which are applicable to the evaluation of integrals of direct stress terms, viz.  $\iint \sigma_x^i \sigma_x^k dx dy$ ,  $\iint \sigma_y^i \sigma_y^k dx dy$ ,  $\iint \tau_{xy}^i \tau_{xy}^k dx dy$ , and  $\iint \tau_{yx}^i \tau_{yx}^k dx dy$ , may be directly obtained from integration.

Figs. A.1a and A.1b show the variations of  $\sigma_x^i$  and  $\sigma_x^k$ , respectively, for a rectangular element. The stress functions may be written as

$$\sigma_x^i = \sigma_{x,m}^i + k_1 x \quad (A.1)$$

and 
$$\sigma_x^k = \sigma_{x,m}^k + k_2 x \quad (A.2)$$

where 
$$k_1 = \frac{\sigma_{x,m+1}^i - \sigma_{x,m}^i}{a} \quad (A.3)$$

and 
$$k_2 = \frac{\sigma_{x,m+1}^k - \sigma_{x,m}^k}{a} \quad (A.4)$$

Then 
$$\int_0^b \int_0^a \sigma_x^i \sigma_x^k dx dy = \int_0^b \int_0^a (\sigma_{x,m}^i + k_1 x)(\sigma_{x,m}^k + k_2 x) dx dy$$

$$= b(a\sigma_{x,m}^i \sigma_{x,m}^k + \frac{a^2}{2} k_1 \sigma_{x,m}^k + k_1 k_2 \frac{a^3}{3} + k_2 \frac{a^2}{2} \sigma_{x,m}^i)$$

Substituting (A.3) and (A.4) into the above expression and simplifying,

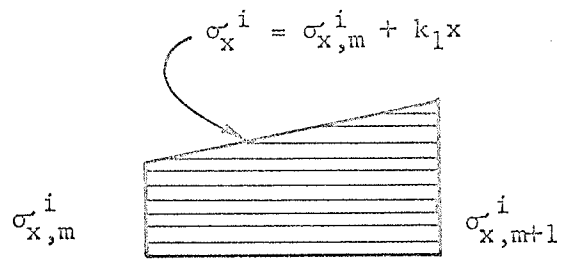
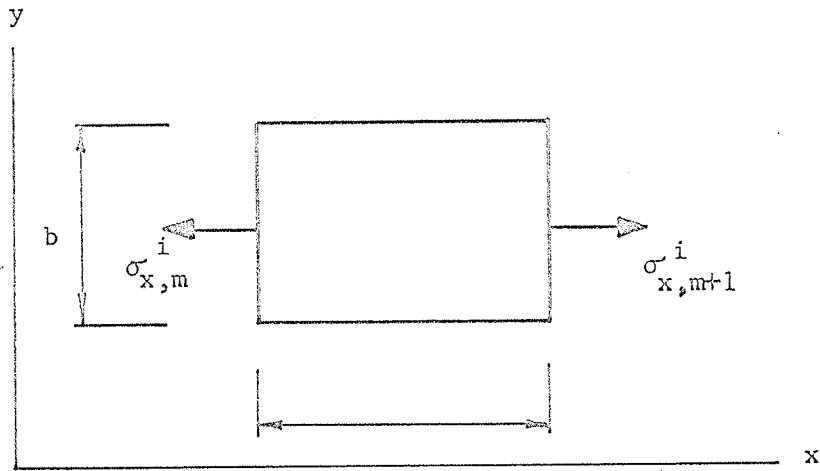


Fig. A.1a - Stress Variation for  $\sigma_x^i$

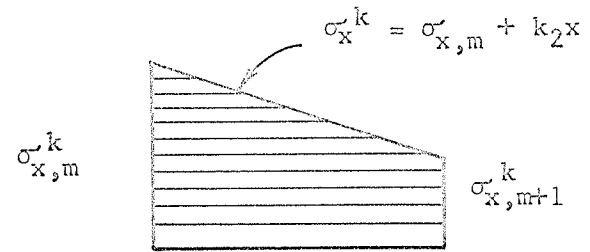
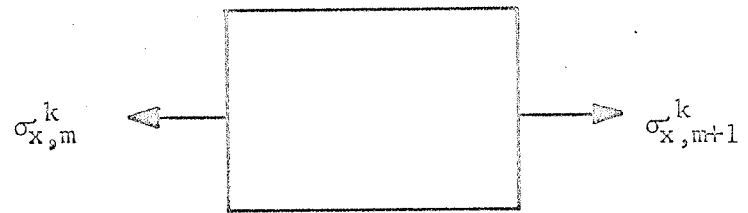


Fig. A.1b - Stress Variation for  $\sigma_x^k$

$$\begin{aligned} \int_0^b \int_0^a \sigma_x^i \sigma_x^k dx dy &= \frac{ab}{6} (2\sigma_{x,m}^i \sigma_{x,m}^k + 2\sigma_{x,m+1}^i \sigma_{x,m+1}^k + \sigma_{x,m}^i \sigma_{x,m+1}^k \\ &\quad + \sigma_{x,m+1}^i \sigma_{x,m}^k) \\ &= \frac{ab}{6} \left[ \sigma_{x,m}^i (2\sigma_{x,m}^k + \sigma_{x,m+1}^k) + \sigma_{x,m+1}^i (2\sigma_{x,m+1}^k + \sigma_{x,m}^k) \right] \end{aligned} \quad (A.5)$$

where (ab) is the area of the rectangular element.

#### A.2 Rectangular Elements --- Crossed Stress Terms

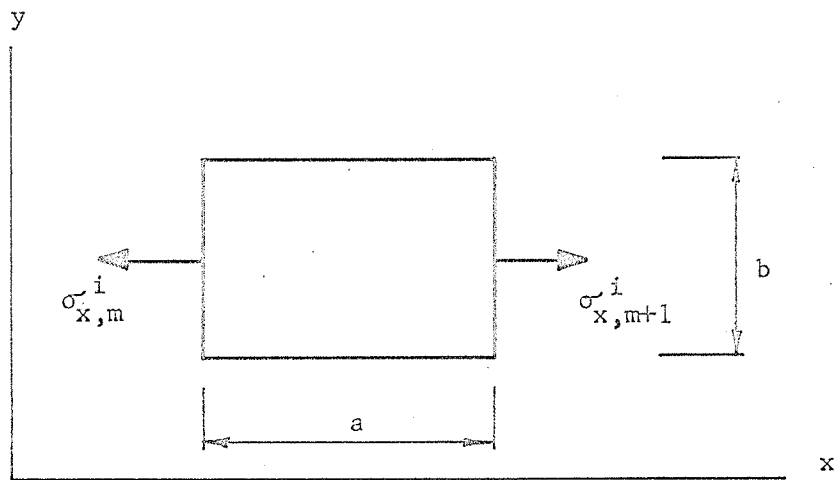
The integrals for the crossed stress terms, viz.  $\iint \sigma_x^i \sigma_y^k dx dy$  and  $\iint \sigma_y^i \sigma_x^k dx dy$ , require separate consideration, since  $\sigma_x^i$  is a function of x while  $\sigma_y^k$  is a function of y.

Equation (A.1) again represents the stress function for  $\sigma_x^i$ , whereas the stress function for  $\sigma_y^k$  is

$$\sigma_y^k = \sigma_{y,n}^k + k_3 y \quad (A.6)$$

as shown in Figs. A.2a and A.2b. Substituting equations (A.1) and (A.6) into the integral,

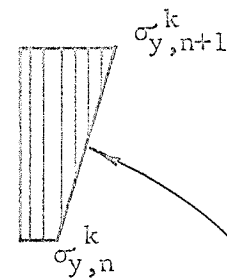
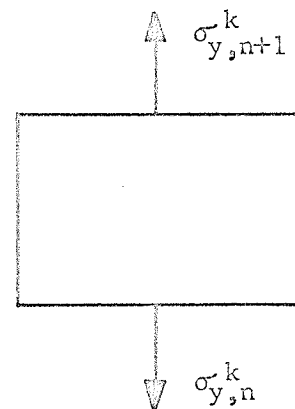
$$\begin{aligned} \int_0^b \int_0^a \sigma_x^i \sigma_y^k dx dy &= \int_0^b \int_0^a (\sigma_{x,m}^i + k_1 x) (\sigma_{y,n}^k + k_3 y) dx dy \\ &= \int_0^b \int_0^a (\sigma_{x,m}^i + k_1 x \sigma_{y,n}^k + k_3 y \sigma_{x,m}^i + k_1 k_3 xy) dx dy \\ &= ab \sigma_{x,m}^i \sigma_{y,n}^k + k_1 \frac{a^2 b}{2} \sigma_{y,n}^k + k_3 \frac{ab^2}{2} \sigma_{x,m}^i + k_1 k_3 \frac{a^2 b^2}{4} \end{aligned}$$



$$\sigma_x^i = \sigma_{x,m}^i + k_1 x$$



Fig. A.2a - Stress Variation for  $\sigma_x^i$



$$\sigma_y^k = \sigma_{y,n}^k + k_3 y$$

Fig. A.2b - Stress Variation for  $\sigma_y^k$

Putting  $k_1 = \frac{\sigma_{x,m+1}^i - \sigma_{x,m}^i}{a}$  and  $k_3 = \frac{\sigma_{y,n+1}^k - \sigma_{y,n}^k}{b}$

and simplifying, one gets

$$\begin{aligned} \int_0^b \int_0^a \sigma_x^i \sigma_y^k dx dy &= \frac{ab}{4} (\sigma_{x,m}^i \sigma_{y,n}^k + \sigma_{x,m+1}^i \sigma_{y,n+1}^k + \sigma_{x,m}^i \sigma_{y,n+1}^k \\ &\quad + \sigma_{x,m+1}^i \sigma_{y,n}^k) \\ &= \frac{ab}{4} \sigma_{x,m}^i (\sigma_{y,n}^k + \sigma_{y,n+1}^k) + \sigma_{x,m+1}^i (\sigma_{y,n+1}^k + \sigma_{y,n}^k) \end{aligned} \quad (A.7)$$

in which (ab) is again the area of the element.

### A.3 Elements at Curvilinear Boundaries

As mentioned earlier, elements of shapes other than rectangular have to be considered when dealing with curvilinear boundaries. It is, therefore, important to find out what modifications to the integrals have to be made in such cases. Fig. A.3 illustrates a truncated-rectangular element, the integral of which may be considered as the difference in the integrals for the rectangle and for the triangle. For instance, the integral  $\iint \sigma_x^i \sigma_x^k dx dy$  for this element becomes

$$\begin{aligned} \iint \sigma_x^i \sigma_x^k dx dy &= \iint_{\text{rect.}} \sigma_x^i \sigma_x^k dx dy - \iint_{\text{tria.}} \sigma_x^i \sigma_x^k dx dy \\ &= \int_0^b \int_0^a \sigma_x^i \sigma_x^k dx dy - \frac{1}{2} \int_0^d \int_{a-c}^a \sigma_x^i \sigma_x^k dx dy \end{aligned}$$

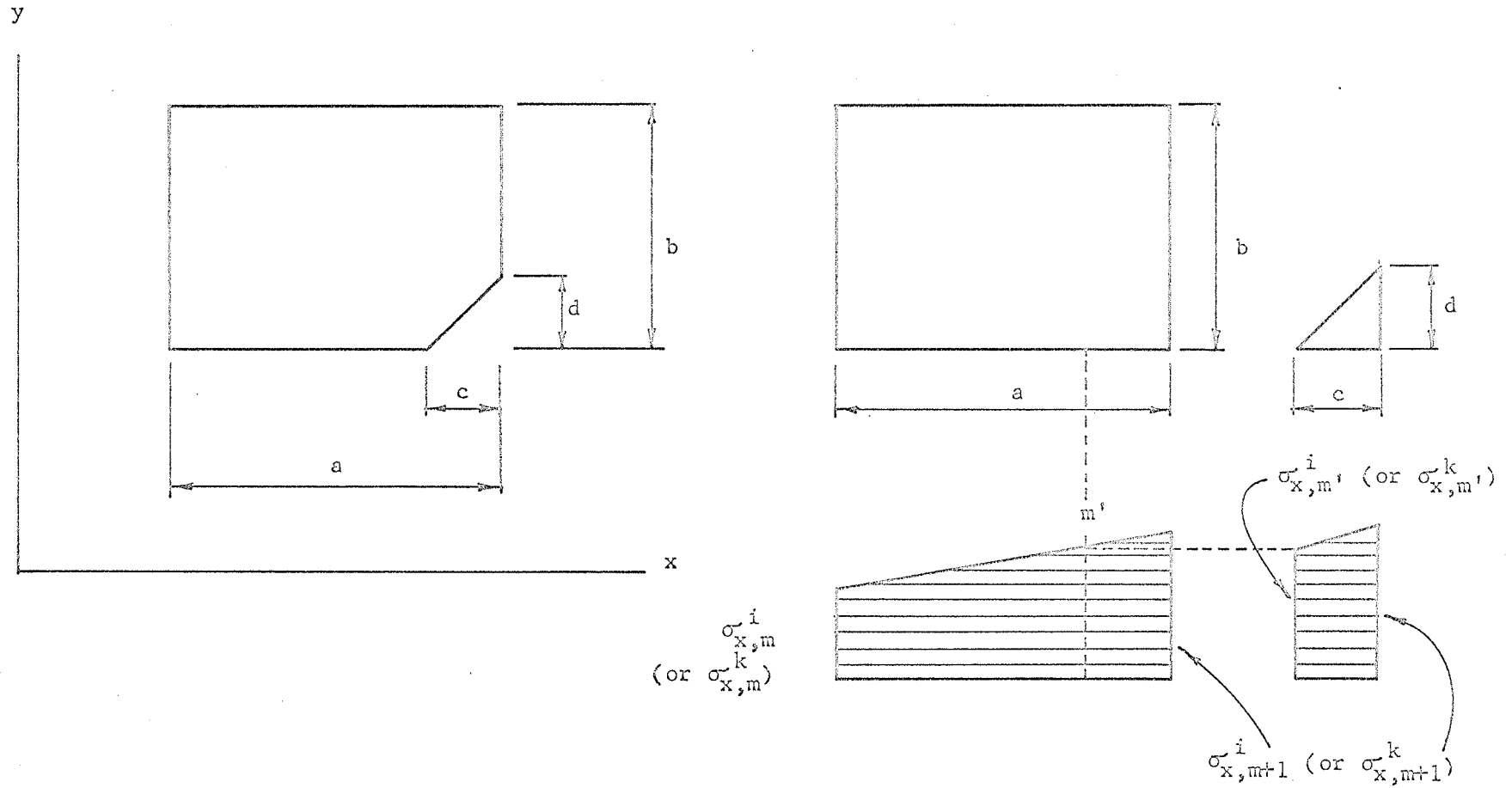


Fig. A.3 - Stress Variations on a Truncated-Rectangular Element

$$= \int_0^b \int_0^a \sigma_x^i \sigma_x^k dx dy - \frac{1}{2} \int_0^d \int_0^a \sigma_x^i \sigma_x^k dx dy + \frac{1}{2} \int_0^d \int_0^{a-c} \sigma_x^i \sigma_x^k dx dy$$

Referring to equation (A.5) for each term in the above expression and grouping accordingly, one gets

$$\begin{aligned} \iint \sigma_x^i \sigma_x^k dx dy &= \left[ \frac{ab}{6} - \frac{a(d/2)}{6} + \frac{d(a-c)/2}{6} \right] \left[ \sigma_{x,m}^i (2\sigma_{x,m}^k + \sigma_{x,m+1}^k) \right. \\ &\quad \left. + \sigma_{x,m+1}^i (2\sigma_{x,m+1}^k + \sigma_{x,m}^k) \right] \\ &= \left( \frac{ab}{6} - \frac{cd/2}{6} \right) \left[ \sigma_{x,m}^i (2\sigma_{x,m}^k + \sigma_{x,m+1}^k) + \sigma_{x,m+1}^i (2\sigma_{x,m+1}^k + \sigma_{x,m}^k) \right] \quad (A.8) \end{aligned}$$

in which  $(ab - cd/2)$  is the area of the truncated-rectangular element. It may thus be concluded that the basic expressions remain unchanged. The same conclusion may be drawn for integrals of crossed stress terms, and also for elements of other shapes as long as they are bounded by straight lines. This is, in fact, a logical deduction from the principle of superposition, because linearity is assumed to exist in relationships of all quantities concerned.

APPENDIX B

ADAPTATION OF THE FLEXIBILITY COEFFICIENT METHOD TO COMPUTERS

The computations of stresses using the Flexibility Coefficient Method may be carried out in the following steps, some or all of which may be adapted to computer operations. It should be mentioned that, as in many other cases, complete computerization may not be the best approach. The importance and advantage of properly located human links cannot be over-emphasized.

- (1) Set up  $2E$  equilibrium equations for the  $E$  elements.
- (2) Choose the appropriate  $I$  stress resultants as redundants.
- (3) Call subroutine for simultaneous equations to solve the equilibrium equations, making one redundant unity and others zero. This is performed  $(I+1)$  times to obtain the stresses caused by each redundant and also by applied loads acting on the primary structure.
- (4) Call subroutine for flexibility coefficients and load terms.
- (5) Call subroutine for simultaneous equations to solve for the redundants.
- (6) Back-substitute into equilibrium equations in (1) and solve for the remaining stress resultants.
- (7) Divide the stress resultants by corresponding lengths to get the stresses, unit thickness of the body being considered.

Of the seven steps outlined above, only step (4) needs further discussion, since the other subroutines are fairly standard. Notation

for stresses are shown in Fig. B.1. Input to the computer includes the area and the eight stress terms for each element. Each stress term is fed in in a two-dimensional array, e.g. XL(I,J), the columns corresponding to the element numbers and the rows corresponding to respective redundants, the last row being the stress terms due to applied loads. Therefore, the dimensions of each of these arrays are (I+1) rows by E columns. The flexibility coefficients are assembled as a square matrix D(I,K), whose order is (I+1), the last row or column with signs changed forming the right-hand-sides of the linear equations in step (5). The flow chart for these operations is shown in Fig. B.2 to which the following legend applies:

NSET = Number of sets to be solved

UM =  $\mu$  = Poisson's ratio

NEL = E = Number of elements

NRE = Number of redundants plus one

$$XINT = \iint \sigma_x^i \sigma_x^k dx dy$$

$$YINT = \iint \sigma_y^i \sigma_y^k dx dy$$

$$XYINT = (1 + \mu) \iint \tau_{xy}^i \tau_{xy}^k dx dy$$

$$YXINY = (1 + \mu) \iint \tau_{yx}^i \tau_{yx}^k dx dy$$

$$CINT = -\mu \iint \sigma_x^i \sigma_y^k dx dy - \mu \iint \sigma_y^i \sigma_x^k dx dy$$

This "flexibility coefficients" program may be linked up with a "simultaneous equations" subroutine to perform steps (4) and (5) simultaneously, as shown in Fig. B.3.

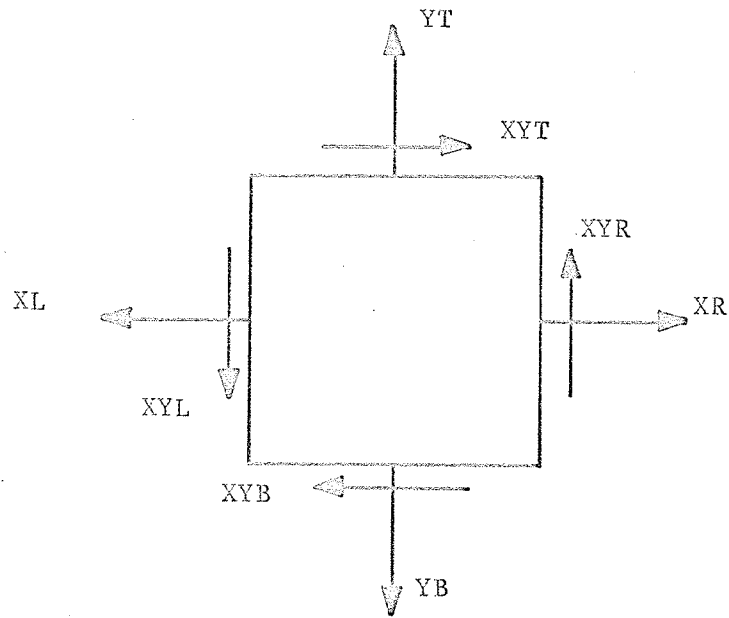


Fig. B.1 - Notation of Stresses in the Program

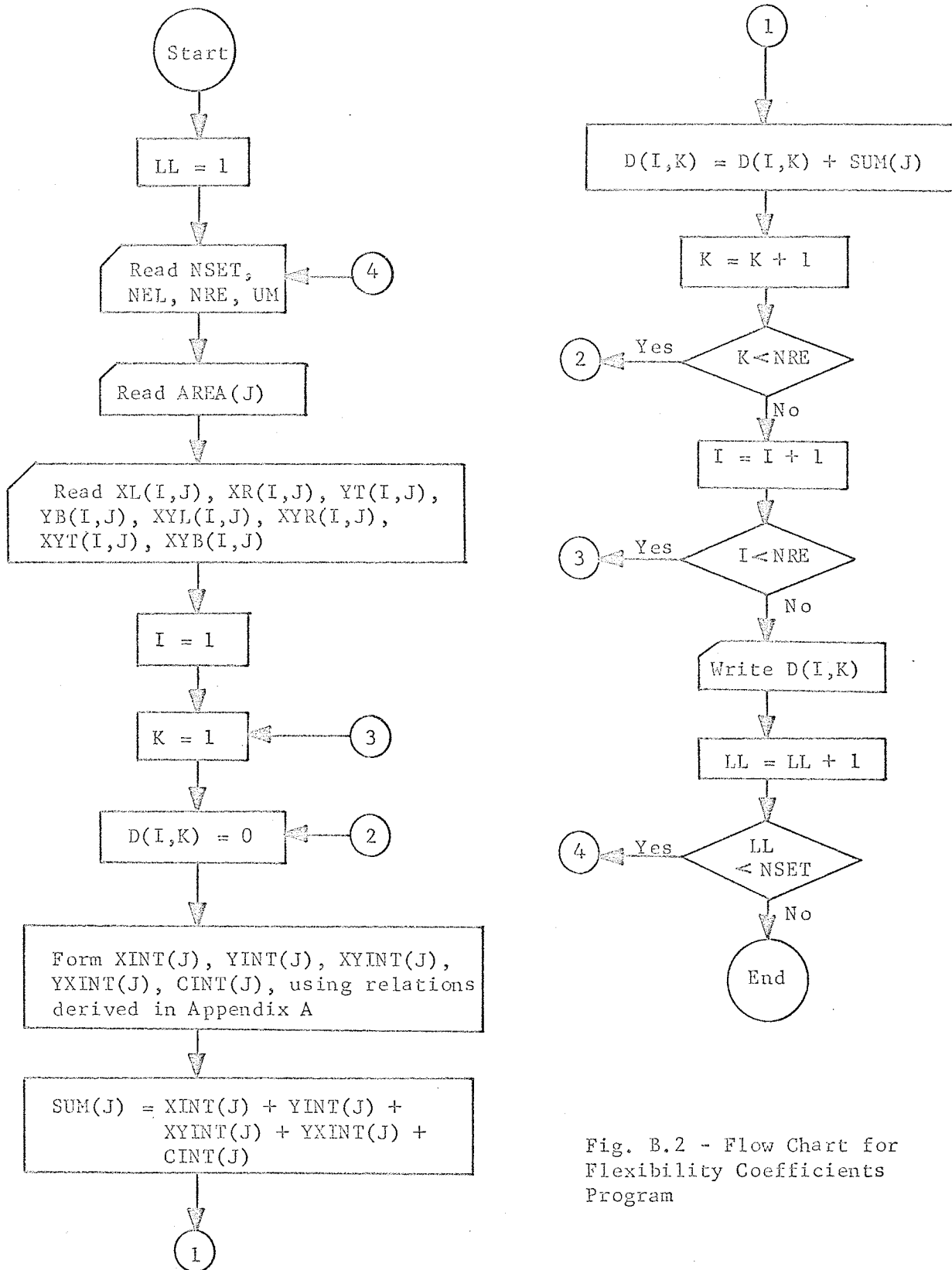


Fig. B.2 - Flow Chart for Flexibility Coefficients Program

Fig. B.3 - Program for Flexibility Coefficients & Stress Resultants

```
DIMENSION XL(51,51),XR(51,51),YT(51,51),YB(51,51),XYL(51,51),
1XYR(51,51),XYT(51,51),XYB(51,51),D(51,51),XINT(40),YINT(40),
2XYINT(40),YXINT(40),CINT(40),SUM(40),AREA(40),E(51,51),F(51)
100 FORMAT (I10)
200 FORMAT (16F5.0)
300 FORMAT (1H0, I5)
500 FORMAT (F10.0)
600 FORMAT (8F10.2)
LL=1
READ (5,100)NSET
4 READ (5,100)NEL
READ (5,100)NRE
READ (5,500)UM
C UM=POISSON'S RATIO
C NEL=NUMBER OF ELEMENTS, NRE=NUMBER OF REDUNDANTS+1
AN=NEL
AN1=AN/16.+0.99
MAN=AN1
NA8=MAN*16
READ (5,200) (AREA(J),J=1,NA8)
WRITE (6,600) (AREA(J),J=1,NEL)
READ (5,200) ((XL(I,J),J=1,NA8),I=1,NRE)
WRITE (6,300)LL
WRITE (6,600) ((XL(I,J),J=1,NEL),I=1,NRE)
READ (5,200) ((XR(I,J),J=1,NA8),I=1,NRE)
WRITE (6,600) ((XR(I,J),J=1,NEL),I=1,NRE)
READ (5,200) ((YT(I,J),J=1,NA8),I=1,NRE)
WRITE (6,600) ((YT(I,J),J=1,NEL),I=1,NRE)
READ (5,200) ((YB(I,J),J=1,NA8),I=1,NRE)
WRITE (6,600) ((YB(I,J),J=1,NEL),I=1,NRE)
READ (5,200) ((XYL(I,J),J=1,NA8),I=1,NRE)
WRITE (6,600) ((XYL(I,J),J=1,NEL),I=1,NRE)
READ (5,200) ((XYR(I,J),J=1,NA8),I=1,NRE)
WRITE (6,600) ((XYR(I,J),J=1,NEL),I=1,NRE)
READ (5,200) ((XYT(I,J),J=1,NA8),I=1,NRE)
WRITE (6,600) ((XYT(I,J),J=1,NEL),I=1,NRE)
READ (5,200) ((XYB(I,J),J=1,NA8),I=1,NRE)
WRITE (6,600) ((XYB(I,J),J=1,NEL),I=1,NRE)
I=1
5 K=1
10 D(I,K)=0.
DO 20 J=1,NEL
XINT(J)=(AREA(J)/6.)*(2.*XL(I,J)*XL(K,J)+2.*XR(I,J)*XR(K,J)
1+XL(I,J)*XR(K,J)+XL(K,J)*XR(I,J))
YINT(J)=(AREA(J)/6.)*(2.*YT(I,J)*YT(K,J)+2.*YB(I,J)*YB(K,J)
1+YT(I,J)*YB(K,J)+YT(K,J)*YB(I,J))
XYINT(J)=(1.+UM)*(AREA(J)/6.)*(2.*XYL(I,J)*XYL(K,J)+2.*
1XYR(I,J)*XYR(K,J)+XYL(I,J)*XYR(K,J)+XYL(K,J)*XYR(I,J))
```

Fig. B.3 - Cont'd

```
YXINT(J)=(1.+UM)*(AREA(J)/6.)*(2.*XYT(I,J)*XYT(K,J)+2.*XYB
1(I,J)*XYB(K,J)+XYT(I,J)*XYB(K,J)+XYT(K,J)*XYB(I,J)
CINT(J)=(-UM/4.)*(XL(I,J)*YB(K,J)+XR(I,J)*YT(K,J)+XL(I,J)*YT(K,J)
1+XR(I,J)*YB(K,J)+YB(I,J)*XL(K,J)+YT(I,J)*XR(K,J)+YB(I,J)*XR(K,J)
2+YT(I,J)*XL(K,J))*AREA(J)
SUM(J)=XINT(J)+YINT(J)+XYINT(J)+YXINT(J)+CINT(J)
D(I,K)=D(I,K)+SUM(J)
20 CONTINUE
K=K+1
IF (K-NRE)10,10,30
30 I=I+1
IF (I-NRE)5,5,40
40 NRE1=NRE-1
DO 60 I=1,NRE1
DO 60 K=1,NRE1
E(I,K)=D(I,K)
F(K)=-D(NRE,K)
60 CONTINUE
WRITE (6,400) (((I,K,E(I,K)),K=1,NRE1),I=1,NRE1)
400 FORMAT (4(1H0,I3,I3,F8.3))
WRITE (6,900) ((K,F(K)),K=1,NRE1)
900 FORMAT (4(1H0,I3,3X,F8.3))
CALL SOLVE(NRE1,E,F)
LL=LL+1
IF (LL-NSET)4,4,50
50 CONTINUE
END
```

```
SUBROUTINE SOLVE(N,A,B)
DIMENSION A(51,51),B(51),X(51)
NMI=N-1
DO 300 K=1,NMI
KP1=K+L
L=K
DO 400 I=KP1,N
IF (ABS(A(I,K))-ABS(A(L,K)))400,400,401
401 L=I
400 CONTINUE
IF (L-K)500,500,405
405 DO 410 J=K,N
TEMP=A(K,J)
A(K,J)=A(L,J)
410 A(L,J)=TEMP
TEMP=B(K)
```

Fig. B.3 - Cont'd

```
B(K)=B(L)
B(L)=TEMP
500 DO 300 I=KPL,N
    FACTO=A(I,K)/A(K,K)
    A(I,K)=0.
    DO 301 J=KPL,N
301 A(I,J)=A(I,J)-FACTO*A(K,J)
300 B(I)=B(I)-FACTO*B(K)
    X(N)=B(N)/A(N,N)
    I=NML
710 IPL=I+1
    SUM=0.
    DO 700 J=IPL,N
700 SUM=SUM+A(I,J)*X(J)
    X(I)=(B(I)-SUM)/A(I,I)
    I=I-1
    IF (I)800,800,700
800 WRITE (6,901) ((JJ,X(JJ)),JJ=1,N)
901 FORMAT (4(1H0,I5,5X,E15.7))
    RETURN
END
```

APPENDIX C  
CASTING OF ARALDITE SHEETS FOR TWO-DIMENSIONAL  
PHOTOELASTICITY

The material used was ARALDITE 502. It is a light straw-coloured epoxy resin available in a very viscous liquid form. When mixed with aliphatic polyamines or other recommended hardeners, it yields a photoelastic material with a very high figure of merit. The hardener used was HARDENER 951. Both the plastic resin and the hardener were supplied by the CIBA Corporation through the Intertechnology Limited of Ontario, Canada.

The casting procedures may be divided into three parts: weighing and pre-heating, mode preparation, mixing and pouring.

(1) Weighing and Pre-heating

The total amount of resin-hardener mixture required was calculated using the approximate formula

$$W = 18.5 \times A \times t$$

where  $W$  = total weight needed in grams,

$A$  = area of sheet in sq. in.,

$t$  = desired thickness in inches.

Correct amount of resin and hardener was weighed, paper cups being used as containers. The resin as obtained from the can was fairly clear and free of bubbles, but pouring and other handlings would invariably introduce some bubbles. And, being a very viscous liquid, it would

not free the bubbles before a lengthy period of undisturbed settling. It was, therefore, necessary to pre-heat it with an infra-red lamp for about 20 minutes, during which time the mode could be prepared. The bubbles were driven to the surface and conveniently removed with a wooden tongue-depressor.

(2) Mode Preparation

The resin-hardener mixture, when partly or completely cured, sticks to most surfaces. Teflon is suggested by many researchers as the material for making the mode. However, teflon sheets do not come with glossy-finished surfaces and have to be carefully polished if a perfectly smooth surface is desired. It was found that perspex plates were an excellent substitute in that they produced surfaces on the casted araldite which did not require any polishing at all.

One disadvantage of using perspex plates was their tendency to warp after three or four castings, probably due to the heat generated in the curing process. However, their relatively low cost allowed them to be economically discarded after three castings or when appreciable warping was noticed, whichever occurred first.

The mode was made with two 8" x 5" x 1/4" perspex plates, with three 10 mm x 10 mm flexible teflon strips forming three edges. The fourth edge, preferably a lengthwise one, was left open for pouring. The assembly was held together by C-clamps, and artist's cement was applied around the outside of the edges for water-proofing. The mode was then placed in an inclined position, about 30° with the bench. It was then slightly heated with an infra-red lamp to about 20°F above

room temperature to facilitate free-flowing of the poured mixture. Just before the mode was assembled, light machine oil was applied, very sparingly, to the inner surfaces of the perspex plates to serve as a releasing agent.

(3) Mixing and Pouring

The temperature at mixing should not be so high that the pot-life of the mixture is shortened to an extent not leaving sufficient time for proper mixing, nor should it be so low that the mixture is viscous and difficult to mix without vigorous stirring. A temperature between 85° to 90°F was found to be desirable. The pre-heated resin was, therefore, allowed to cool to this temperature before mixing with the hardener.

The hardener was gently poured into the resin and mixed with the help of a thermometer, which was worked in a circular motion around the inside wall of the paper cup. The polymerization of the resin was an exothermic process. Bubbles at this stage, if any, would be driven up to the surface by the heat generated, and were drawn to the side of the container and bursted or scraped off. When the temperature reached 120°F the mixture was ready for pouring. A disposable rod, or simply a straw, was held against one edge of the mode to guide the pouring in a thin stream.

Curing was then allowed to proceed in undisturbed surroundings at room temperature. The clear, bubble-free, 10 mm thick aradite sheet could be released from the mode after 24 hours, but should be allowed to rest on a flat surface and continue to cure for another 2 to 6 days.